NASA/TM–2014–218535

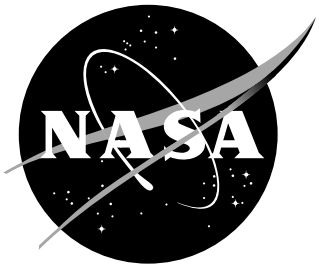

Mars Entry Atmospheric Data System Modeling, Calibration, and Error Analysis

Christopher D. Karlgaard, John Van Norman, and Paul M. Siemers
Analytical Mechanics Associates, Inc., Hampton, Virginia

Mark Schoenenberger, and Michelle M. Munk
Langley Research Center, Hampton, Virginia

October 2014

NASA STI Program . . . in Profile

Since its founding, NASA has been dedicated to the advancement of aeronautics and space science. The NASA scientific and technical information (STI) program plays a key part in helping NASA maintain this important role.

The NASA STI Program operates under the auspices of the Agency Chief Information Officer. It collects, organizes, provides for archiving, and disseminates NASA's STI. The NASA STI Program provides access to the NASA Aeronautics and Space Database and its public interface, the NASA Technical Report Server, thus providing one of the largest collection of aeronautical and space science STI in the world. Results are published in both non-NASA channels and by NASA in the NASA STI Report Series, which includes the following report types:

- TECHNICAL PUBLICATION. Reports of completed research or a major significant phase of research that present the results of NASA programs and include extensive data or theoretical analysis. Includes compilations of significant scientific and technical data and information deemed to be of continuing reference value. NASA counterpart of peer-reviewed formal professional papers, but having less stringent limitations on manuscript length and extent of graphic presentations.
- TECHNICAL MEMORANDUM. Scientific and technical findings that are preliminary or of specialized interest, e.g., quick release reports, working papers, and bibliographies that contain minimal annotation. Does not contain extensive analysis.
- CONTRACTOR REPORT. Scientific and technical findings by NASA-sponsored contractors and grantees.
- CONFERENCE PUBLICATION. Collected papers from scientific and technical conferences, symposia, seminars, or other meetings sponsored or co-sponsored by NASA.
- SPECIAL PUBLICATION. Scientific, technical, or historical information from NASA programs, projects, and missions, often concerned with subjects having substantial public interest.
- TECHNICAL TRANSLATION. English-language translations of foreign scientific and technical material pertinent to NASA's mission.

Specialized services also include creating custom thesauri, building customized databases, and organizing and publishing research results.

For more information about the NASA STI Program, see the following:

- Access the NASA STI program home page at ***http://www.sti.nasa.gov***
- E-mail your question via the Internet to help@sti.nasa.gov
- Fax your question to the NASA STI Help Desk at 443-757-5803
- Phone the NASA STI Help Desk at 443-757-5802
- Write to:
  NASA STI Help Desk
  NASA Center for AeroSpace Information
  7115 Standard Drive
  Hanover, MD 21076–1320

NASA/TM–2014–218535

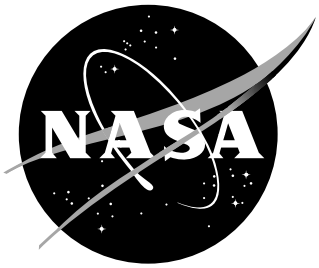

Mars Entry Atmospheric Data System Modeling, Calibration, and Error Analysis

Christopher D. Karlgaard, John Van Norman, and Paul M. Siemers
Analytical Mechanics Associates, Inc., Hampton, Virginia

Mark Schoenenberger, and Michelle M. Munk
Langley Research Center, Hampton, Virginia

National Aeronautics and
Space Administration

Langley Research Center
Hampton, Virginia 23681-2199

October 2014

Acknowledgments

The authors are grateful for contributions from Roger Beck, Artem Dyakonov, Noah Favaregh, Chris Kuhl, Stephen O'Keefe, Jeremy Shidner, and Brady White in the areas of estimator design, system modeling, wind tunnel data reduction, and calibration. The authors are also grateful to Karen Bibb, Ron Merski, Matt Rhode, Eric Walker, and Henry Wright for helpful comments and suggestions.

Available from:

NASA Center for AeroSpace Information
7115 Standard Drive
Hanover, MD 21076-1320
443-757-5802

Abstract

The Mars Science Laboratory (MSL) Entry, Descent, and Landing Instrumentation (MEDLI)/Mars Entry Atmospheric Data System (MEADS) project installed seven pressure ports through the MSL Phenolic Impregnated Carbon Ablator (PICA) heatshield to measure heatshield surface pressures during entry. These measured surface pressures are used to generate estimates of atmospheric quantities based on modeled surface pressure distributions. In particular, the quantities to be estimated from the MEADS pressure measurements include the dynamic pressure, angle of attack, and angle of sideslip. This report describes the calibration of the pressure transducers utilized to reconstruct the atmospheric data and associated uncertainty models, pressure modeling and uncertainty analysis, and system performance results. The results indicate that the MEADS pressure measurement system hardware meets the project requirements.

Contents

List of Figures

List of Tables

List of Symbols

a_s	=	Speed of sound, m/s
A_c	=	Tube cross-sectional area
a_0, a_1, a_2	=	Transducer calibration coefficients
b_0, b_1, b_2, b'	=	Knudsen model coefficients
c_0, c_1, c_2	=	Potter model coefficients
C	=	Sutherland constant
C_p	=	Pressure coefficient
D	=	Tube Diameter, in
d^+	=	Orifice Reynolds number
$\boldsymbol{F}$	=	Calibration coefficient matrix
$\boldsymbol{H}$	=	Linearization of pressure distribution model
$\boldsymbol{h}$	=	Pressure distribution model, Pa
$\boldsymbol{I}$	=	Identity matrix
L	=	Tube length
L_{max}	=	Maximum leak rate
M_∞	=	Mach number
$\boldsymbol{P}$	=	State covariance
P_0	=	Input pressure (Laplace domain)
P_L	=	Lagged pressure (Laplace domain)
p	=	Pressure, Pa
δp	=	Pressure error, Pa
$\hat{p}$	=	Adjusted pressure, Pa
$\tilde{p}$	=	Quantized pressure measurement, Pa
$\bar{p}$	=	Saturated pressure measurement, Pa
p_∞	=	Static pressure, Pa
p_t	=	Total pressure, Pa
$\boldsymbol{p}$	=	Pressure measurement vector, Pa
q_∞	=	Dynamic pressure, Pa
$\boldsymbol{R}$	=	Measurement covariance matrix
R_d	=	Acoustic impedance
R_g	=	Specific gas constant
$\mathcal{R}$	=	Pressure ratio, $\mathcal{R} = p_\infty/p_t$
r	=	Length scale
S	=	Reference area, m^2
s	=	Laplace variable
T	=	Gas temperature
T_0	=	Reference temperature

T_1	=	Transducer temperature, C
T_2	=	SSE temperature, C
t	=	Time, s
V	=	Voltage
v	=	Transducer entrapped volume
$\boldsymbol{x}$	=	Atmospheric state vector, $\boldsymbol{x} = [\alpha, \beta, p_\infty, q_\infty]^T$
$\boldsymbol{y}$	=	Linearized residual
$\boldsymbol{z}$	=	Calibration parameter array, $\boldsymbol{z} = [T_1, T_2, V, a_0, a_1, a_2]^T$
α	=	Angle of attack, rad
α_T	=	Total angle of attack, rad
β	=	Angle of sideslip, rad
γ	=	Ratio of specific heats
$\boldsymbol{\epsilon}$	=	Pressure measurement error vector, Pa
ζ	=	Lag model damping
η_p	=	Transducer measurement noise
κ	=	Knudsen number
λ	=	Mean free path
μ	=	Viscosity
μ_0	=	Reference viscosity
$\boldsymbol{\xi}$	=	Calibration coefficient array, $\boldsymbol{\xi} = [a_0, a_1, a_2]^T$
ρ	=	Density, kg/m^3
σ	=	Standard deviation
τ	=	Pneumatic lag time constant, s
τ_w	=	Shear stress
$\boldsymbol{\Omega}_z$	=	Covariance of $\boldsymbol{z}$
ω_n	=	Lag model natural frequency, rad/s

List of Acronyms

AFE	=	Aeroassist Flight Experiment
CFD	=	Computational Fluid Dynamics
DOE	=	Design of Experiments
EDL	=	Entry, Descent, and Landing
FADS	=	Flush Air Data System
IFZ	=	In-Flight Zero
IMU	=	Inertial Measurement Unit
LAURA	=	Langley Upwind Relaxation Algorithm
MEADS	=	Mars Entry Atmospheric Data System
MEDLI	=	MSL Entry, Descent, and Landing Instrumentation
MSL	=	Mars Science Laboratory
OML	=	Outer Mold Line
PICA	=	Phenolic Impregnated Carbon Ablator
SEADS	=	Shuttle Entry Air Data System
SSE	=	Sensor Support Electronics
TPS	=	Thermal Protection System
UPWT	=	Unitary Plan Wind Tunnel

Chapter 1

Introduction

This report documents transducer calibration, system error modeling, pressure, pressure uncertainty models and system performance results and uncertainty quantification for the Mars Science Laboratory (MSL) Mars Entry Atmospheric Data System (MEADS) [1, 2]. MEADS is a seven-port flush air data system (FADS) integrated with the 4.5 m diameter MSL aeroshell, the largest aeroshell ever flown to Mars [3]. The Mars Science Laboratory entry vehicle was comprised of a 70 degree sphere-cone heatshield and backshell consisting of a stack of three truncated cones. The forebody was similar to the heatshield geometry developed for the Viking Mars landers. Phenolic Impregnated Carbon Ablator (PICA) was used for the Thermal Protection System (TPS) material. The backshell configuration was also similar to Viking, with a third cone section added to accommodate the parachute volume. The MSL vehicle as-built outer mold line is shown in Fig. 1.1. During most of entry, the capsule used a radial center of mass offset to fly at an angle of attack (approximately 16 degrees at hypersonic conditions). This attitude produced lift to fly a guided entry profile, reducing the landing footprint to a much smaller size than any previous Mars mission. To fly the guided entry, the vehicle carried four pairs of reaction control system jets to perform maneuvers and damp rates. The four pairs of jets could be fired rapidly in different combinations to provide control torques about roll, pitch, yaw, or any other axis by modulating the pulses of the jet.

The MSL heatshield differs from previous Mars mission designs in that the TPS is based upon a tiled scheme, bonded directly to the aeroshell structure with a room temperature vulcanization (RTV) sealant. Viewed exteriorly, MEADS surface pressure orifices are holes of approximately 2 mm diameter drilled directly through the PICA TPS tiles. Metallic spools through the carbon fiber-on-aluminum honeycomb aeroshell structure complete the flowpath from surface orifice to transducer tube as shown in Figure 1.2(a). MEADS therefore represents somewhat of a departure from traditional aircraft FADS, or even the Shuttle Entry Air Data System (SEADS) [4–7], where orifices are precisely machined to relatively small diameters in smooth metallic or nonablating materials with negligible surface roughness. The MEADS ports are arranged in a cruciform pattern over the heatshield windside (see Figure 1.2(b)), in locations where the boundary layer is predicted to remain laminar and aeroheating is predicted to remain relatively low over the expected entry trajectory [1]. All of the pressure ports are located a minimum of 3-inches from the PICA tile seams.

Figure 1.3 shows a timeline of the different events along MSL's entry, descent, and landing (EDL) trajectory [8]. Note that the event times correspond to the nominal trajectory. Actual times differed from the nominal event times due to dispersions in the entry time and atmospheric uncertainties. EDL consists of six major segments: Exo-Atmospheric, Entry, Parachute Descent,

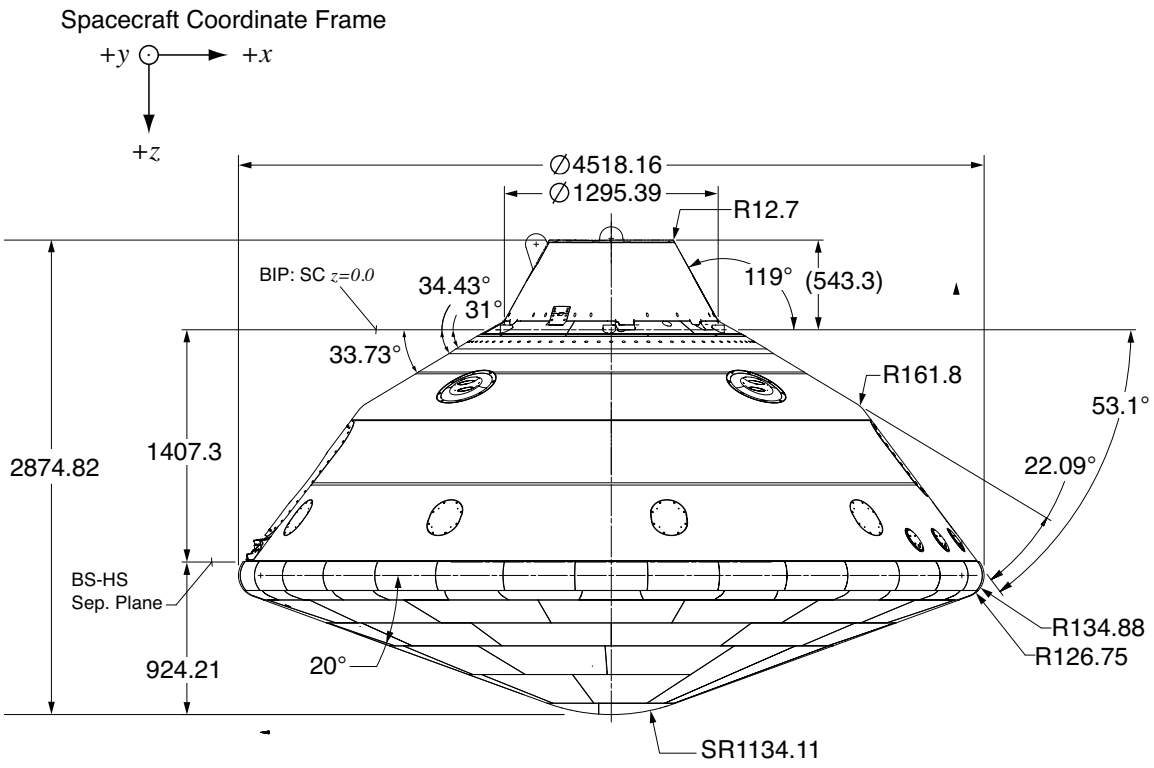

Figure 1.1: Vehicle Geometry

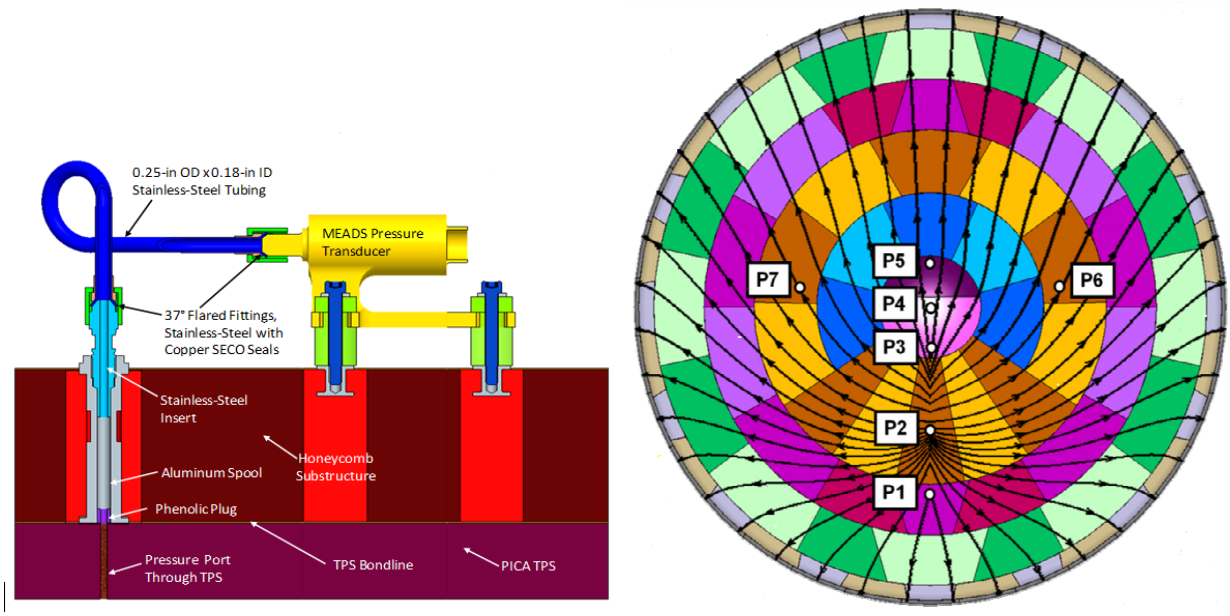

(a) MEDLI/MEADS Tube Configuration

(b) MEDLI/MEADS Pressure Port Locations

Figure 1.2: MEDLI/MEADS Geometry

Powered Descent, Sky Crane, and Fly Away [9]. The Exo-Atmospheric segment begins once the cruise stage separation command is sent. Once the cruise stage separates, Guidance, Navigation,

and Control (GNC) is enabled. Once enabled, the entry body is despun and turned to its entry attitude. Then, the two 75-kg Cruise Balance Masses (CBMs) are jettisoned to enable aerodynamic lift.

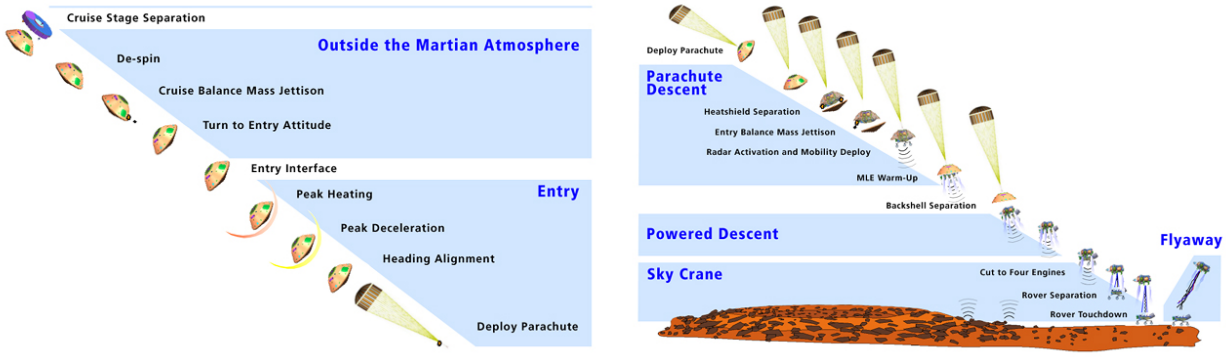

(a) Cruise Stage Separation to Parachute Deployment

(b) Parachute Deployment to Touchdown

Figure 1.3: MSL Entry, Descent, and Landing

The Entry segment starts with the vehicle at the Entry Interface Point (EIP) defined at 3522.2 km from the center of Mars, approximately 540 seconds after cruise stage separation. During the Entry segment, the vehicle goes through peak heating and peak deceleration, the Reaction Control System (RCS) controls the lift vector to achieve the desired down-range and cross-range target. Just prior to parachute deployment, six 25-kg Entry Balance Masses (EBMs) are jettisoned to eliminate lift and the vehicle rolls to point the Terminal Descent Sensor (TDS) to the ground. This maneuver is called the Straighten Up and Fly Right (SUFR) maneuver. Figures 1.4 and 1.5 shows the nominal trajectory over the time period from entry interface to parachute deployment.

The Parachute descent segment starts with the parachute deployment triggered once the vehicle reached Mach 1.7. Once the vehicle achieves a speed of Mach 0.7, the heat shield is jettisoned and the TDS starts acquiring the ground. Note that the MEDLI instruments are powered off 10 seconds prior to heat shield jettison. The command to jettison the backshell and the parachute is issued at an altitude of 1.6 km and at a velocity of approximately 79 m/s. Just before backshell separation, the Mars Landing Engines (MLEs) are primed in preparation for the start of the powered descent segment.

The Powered Descent segment begins at backshell separation. During powered descent, eight independently throttleable MLEs are actuated, initially to execute a divert maneuver for backshell avoidance which brings the vehicle to vertical flight at a descent rate of 32 m/s. Once vertical flight is achieved, a descent at constant velocity to adjust for altitude error at backshell separation starts. This constant velocity phase is followed by a constant deceleration phase, which reducs the vehicle's speed to 0.75 m/s in preparation for the sky crane segment. At this time, the four inboard MLEs are throttled down to near shutdown (1%) while the four remaining MLEs were throttled at 50%. The Sky Crane segment starts following issuance of the rover separation command, which occurrs at an altitude of approximately 18.6 m. The rover is lowered to 7.5 m below the descent stage. Then, the descent stage continues to descend until post-touchdown is detected.

The Fly Away segment starts after touchdown is sensed. Once the descent stage stops it's vertical motion, the bridle and electrical umbilical devices are cut and two of the MLE engines are throttled up to 100% while the other two engines are at slightly less than 100%. This causes the descent stage to pitch to 45 degrees. Once the turn maneuver is completed, all four engines are

throttled up to 100%. Constant thrust is applied to ensure the descent stage impacts the surface at least 300 m from the landing point.

MEADS collects pressure data at a rate of 8 Hz over the portion of MSLs entry from atmospheric interface to 10 seconds before heatshield separation, the latter which occurs at a freestream Mach number of approximately 1.5. As a basic objective, the MEADS hardware is intended to be capable of furnishing data that, without any additional data sources, can be used to recover aerodynamic angles and dynamic pressure. Accuracy to within 0.5 degrees in angle of attack and sideslip are required over portions of the trajectory where freestream dynamic pressures exceed 1750 Pa and 1250 Pa, respectively. Dynamic pressure measurements are required to within 2% where the freestream value exceeds 850 Pa. Used in combination with inertial measurement unit (IMU) data and analyzed with Extended Kalman Filter (EKF) methods [10–14], MEADS data will be used for post-flight reconstruction of vehicle attitude, dynamic pressure, Mach number, atmospheric density, and wind velocity [15]. As MSL is breaking new ground as the first tiled ablator NASA has flown on an entry vehicle heatshield, MEADS is unique in its distinction as the first heatshield-integrated FADS to be employed on an extraplanetary mission on an aeroshell larger than and in an aerothermal environment more extreme than experienced in any previous Mars mission [16].

This document describes how the uncertainties in the as-built MEADS hardware system and pressure models contribute to the uncertainties in the reconstructed data. The remainder of this document is organized as follows. Chapter 2 describes the basic MEADS data processing algorithm, in which pressure measurements are used in conjunction with a model of the surface pressure distribution (based on CFD models) to determine the freestream atmospheric conditions (dynamic pressure, static pressure, angle of attack, and angle of sideslip) using a nonlinear least-squares algorithm. Also in Chapter 2, the CFD pressure models are described along with some description of experimental validation.

The MEADS pressure transducer calibration is described in Chapter 3. A basic overview of the calibration methodology is described, and results from thermal vacuum testing are given along with an uncertainty analysis. Chapter 4 describes hardware system error modeling and CFD pressure distribution uncertainty models. These uncertainty models are then utilized in Chapter 4 to quantify how these uncertainties map to uncertainties in the reconstructed air data state. Concluding remarks are given in Chapter 5.

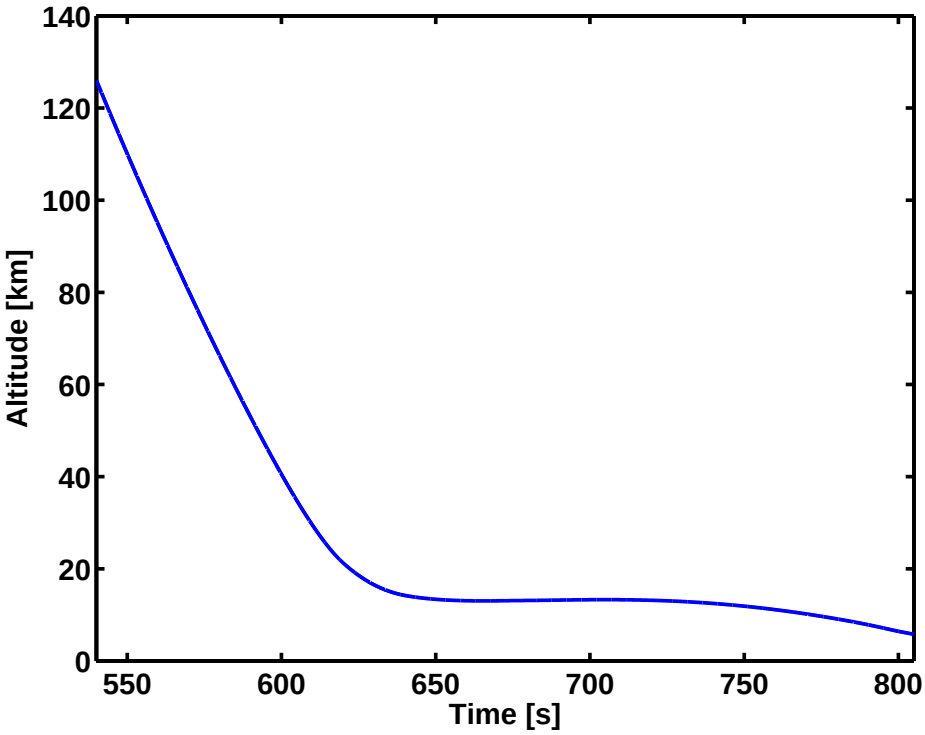

(a) Altitude

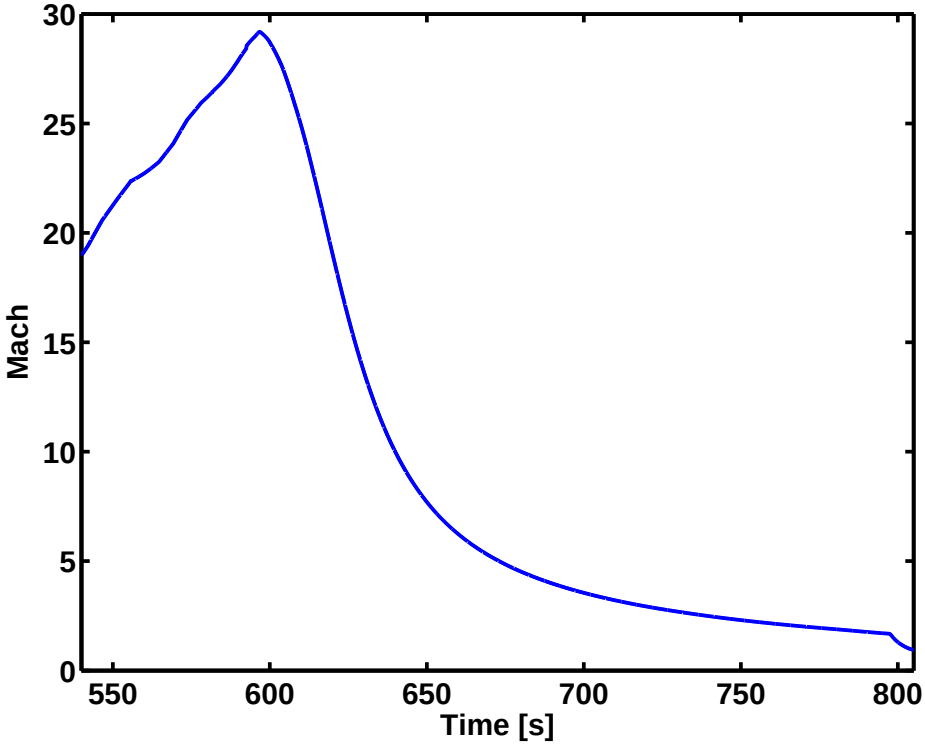

(b) Mach

Figure 1.4: MSL Nominal Trajectory: Altitude and Mach Number

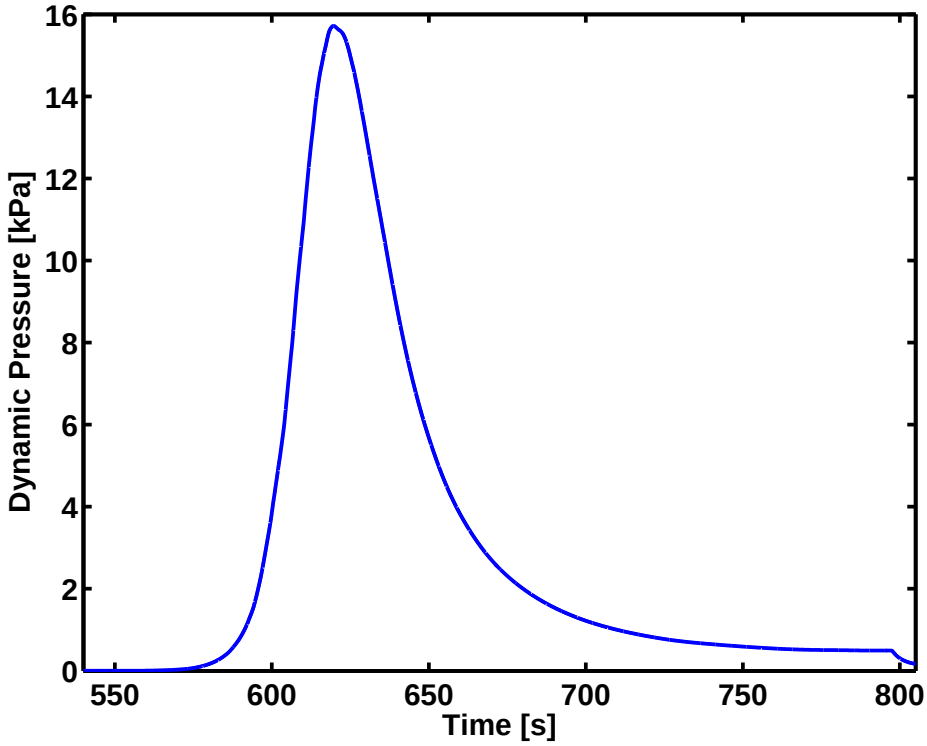

(a) Dynamic Pressure

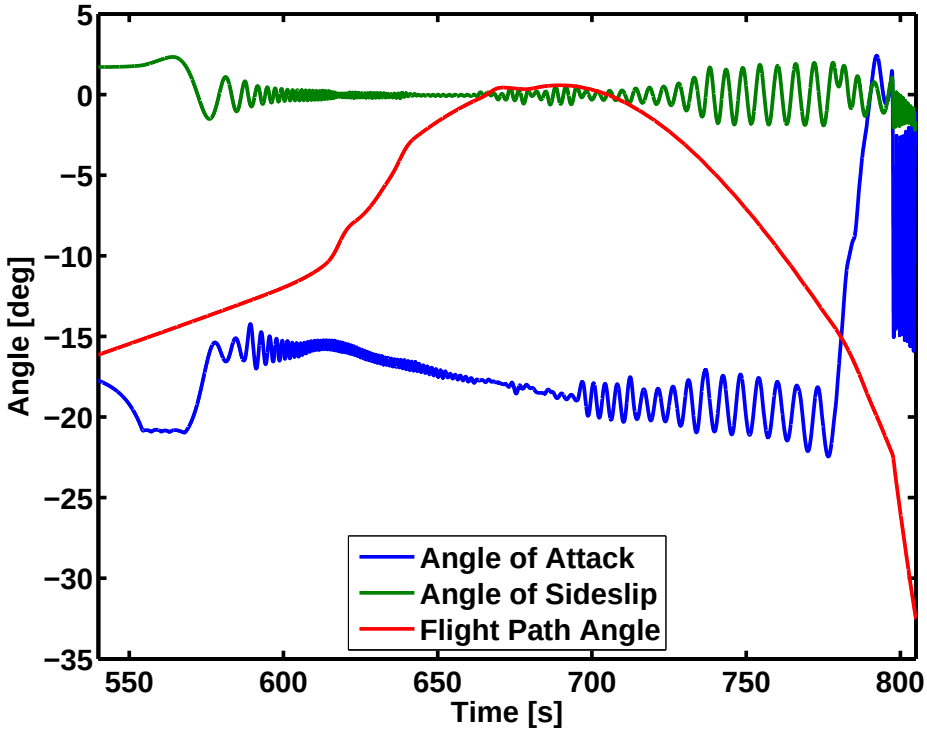

(b) Aerodynamic and Trajectory Angles

Figure 1.5: MSL Nominal Trajectory: Dynamic Pressure and Aerodynamic Angles

Chapter 2

Atmospheric State Estimation and Surface Pressure Modeling

The basic MEADS atmospheric state estimation procedure is essentially similar to the Shuttle Entry Air Data System (SEADS) state estimation described in [4], a point–wise least squares fit of the surface pressure measurements to the modeled pressure distribution to determine minimum–variance estimates of the atmospheric states. This algorithm requires a model of the surface pressure distribution at each port location as a function of the free stream flight conditions. For MSL, this model consists of tabulated CFD pressure solutions for a range of flight conditions that encapsulate the expected trajectories. An uncertainty model of the pressure distribution and sensor hardware is also required for appropriate weighting of the measurements in the least-squares algorithm.

The core of the MEADS pressure model is based on CFD predictions run at representative nominal Mars entry conditions, while the pressure uncertainty model borrows from off-nominal Mars entry CFD, wind tunnel experimentation, and CFD simulation of wind tunnel experiments. Surface pressures are extracted from CFD solutions at the MEADS port locations, which are well known from flight article laser scan metrology. Comparisons between experimental and numerical results were to be used to validate computations and model estimates of error in CFD simulations at flight conditions, however these results are beyond the scope of this report.

2.1 Least–Squares State Variable Estimation

By defining the atmospheric state vector as $\boldsymbol{x} = [\alpha, \beta, q_\infty, p_\infty]^T$, $\mathbf{p}$ as the vector of N observed surface pressures, and the pressure model as $\boldsymbol{h}(\boldsymbol{x}, t)$ then the pressure measurement model can be written compactly as

$$\boldsymbol{p} = \boldsymbol{h}\left(\boldsymbol{x}, t_k\right) + \boldsymbol{\epsilon} \tag{2.1}$$

where $\boldsymbol{\epsilon}$ is the vector of pressure measurement errors and t_k is the measurement sampling time at time increment k. Definition of the aerodynamic angles is shown in Figure 2.1. The pressure measurement model can be approximated by means of the truncated series expansion

$$\boldsymbol{p} \approx \boldsymbol{h}\left(\bar{\boldsymbol{x}}, t_k\right) + \boldsymbol{H}(t_k)\left(\boldsymbol{x} - \bar{\boldsymbol{x}}\right) + \boldsymbol{\epsilon} \tag{2.2}$$

where $\bar{\boldsymbol{x}}$ is a reference state and $\boldsymbol{H}(t_k)$ is the Jacobian matrix

$$\boldsymbol{H}(t_k) = \left[\frac{\partial \boldsymbol{h}}{\partial \boldsymbol{x}}\right]_{\boldsymbol{x}=\bar{\mathbf{x}}} \tag{2.3}$$

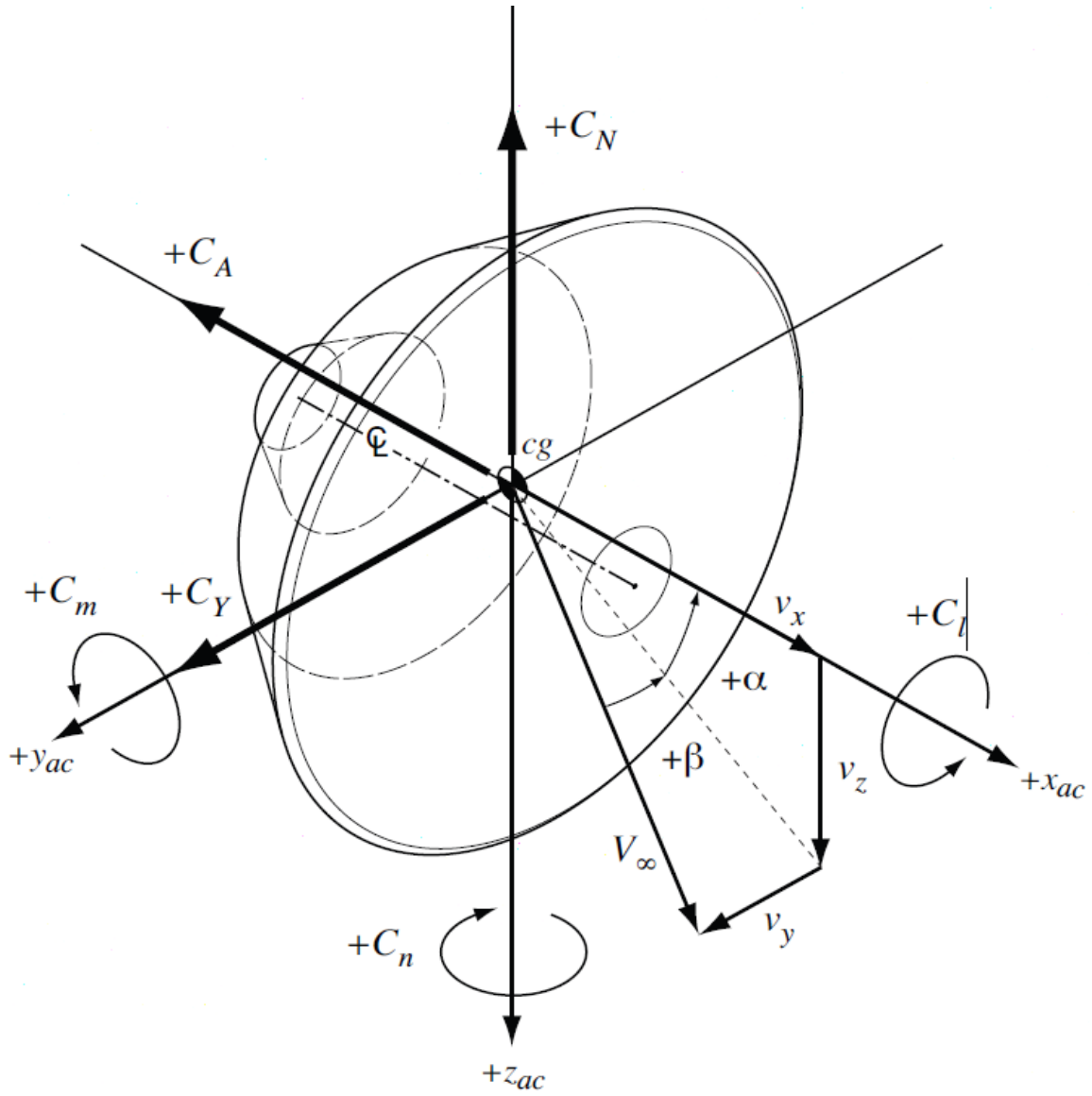

Figure 2.1: MSL Coordinate System

The problem can be reduced to that of a linear regression problem

$$\boldsymbol{y} = \boldsymbol{H}\boldsymbol{x} + \boldsymbol{\epsilon} \tag{2.4}$$

where $\boldsymbol{y} = \boldsymbol{p} - \boldsymbol{h}\left(\bar{\boldsymbol{x}}, t_k\right) + \boldsymbol{H}\bar{\boldsymbol{x}}$. By virtue of the Gauss–Markov theorem, the best linear unbiased estimate of $\boldsymbol{x}$ is the weighted least-squares solution [17],

$$\hat{\boldsymbol{x}} = \left(\boldsymbol{H}^T\boldsymbol{R}^{-1}\boldsymbol{H}\right)^{-1}\boldsymbol{H}^T\boldsymbol{R}^{-1}\boldsymbol{y} \tag{2.5}$$

where $\boldsymbol{R}$ is the pressure measurement error covariance matrix. Since the original relationship between the states and the measurement in Eq. (2.1) is nonlinear, the estimation scheme can be iterated until convergence by successively replacing $\bar{\boldsymbol{x}}$ by $\hat{\boldsymbol{x}}$, using the converged state estimate from the previous sampling time (t_{k-1}) as the initial reference state $\bar{\boldsymbol{x}}$. The state estimate error

covariance matrix $\hat{\boldsymbol{P}}$ can then be computed from

$$\hat{\boldsymbol{P}} = \left(\boldsymbol{H}^T \boldsymbol{R}^{-1} \boldsymbol{H}\right)^{-1} \tag{2.6}$$

Note that the atmospheric state vector formulation is not unique. In particular, any two variables from the set of p_∞, p_t, q_∞, $\mathcal{R}$, and M_∞ can be used in the estimator in addition to α and β. The remaining state variables not used directly in the estimator can be calculated as parameters, having first estimated the atmospheric state variables. Note that the SEADS algorithm [4] made use of p_∞ and p_t in the estimator formulation.

2.2 Nominal Flight CFD Pressure Modeling

The MEADS pressure model is built on CFD solutions from the MSL nominal aerodatabase, computed at points of interest along reference trajectory 05-22 as shown in Fig. 2.2(a). Computations were carried out with the Langley Upwind Relaxation Algorithm (LAURA) code [18] using a two-temperature thermochemical nonequilibrium gas model representative of the Martian atmosphere with a freestream composed of 97 percent CO_2 and 3 percent N_2 by mass. A representative LAURA solution is shown in Fig. 2.2(b). A total of 8 species (CO_2, CO, N_2, O_2, NO, C, N, O) were allowable to model the chemical reactions which take place at energetic flow conditions [19]. A super-catalytic wall boundary condition was used, which imposes recombination of species to freestream composition at the wall so as to yield conservative aeroheating predictions [20]. The vibrational temperature relaxation model of Camac [19] was used throughout, as it has been assumed more accurate than the Millikan-White model [19], however analysis validating differences between the models is beyond the scope of this work. Thin-layer Navier-Stokes (TLNS) equations were used in the computations, a subset of the full Navier-Stokes equations which omits viscous cross terms and thereby reduces the number of calculations required to converge a solution. Previous work had shown that differences between solutions computed with the TLNS and full Navier-Stokes equations were insignificant for the purpose of computing aerodynamics [19]. During a LAURA computation, grids are shock-fitted to the evolving solution with an iterative grid adaptation scheme which maintains orthogonality and enforces $Re_{cell} \sim \mathrm{O}(1)$ at the wall for aeroheating computations. Grid adaptation cycles are repeated until integrated aerodynamic coefficients are constant to within three significant figures, after which final numerical convergence is obtained using a line relaxation algorithm [21]. The nominal aerodatabase runs were computed for the Outer Mold Line (OML) on a 7-block volume grid with 0.23 million points. During design iterations leading up to the final flight configuration (designated OML13-F), the flight TPS was changed from a monolithic ablator design to tiled Phenolic Impregnated Carbon Ablator (PICA) design, changing OML proportions slightly. Point check cases were run at nominal 05-22 trajectory conditions on a volume grid more closely describing the flight article heatshield (MSL-OML13F-21806-clean-heatshield.g) with a total of 1.25 million points. Fig. 2.3(a) and (b) show comparisons between point check and nominal aerodatabase CFD results are used to obtain an estimate of MEADS pressure sensitivity to changes in the flight article OML, grid topology, and grid refinement.

Numerical solutions at off-nominal flight conditions were used to bound the expected ranges of MEADS port environments and sensitivities. LAURA solutions from runs utilizing 09-TPS-01 and -02 trajectory conditions were analyzed, as these particular trajectories were designed for stressing TPS environments [22]. Cases with simulated gap filler protrusions along reference trajectory 08-01A were queried for estimates of pressure augmentation factors in the vicinity of step discontinuities in the heatshield surface. Comparisons between 05-22 and 09-TPS trajectories are shown against

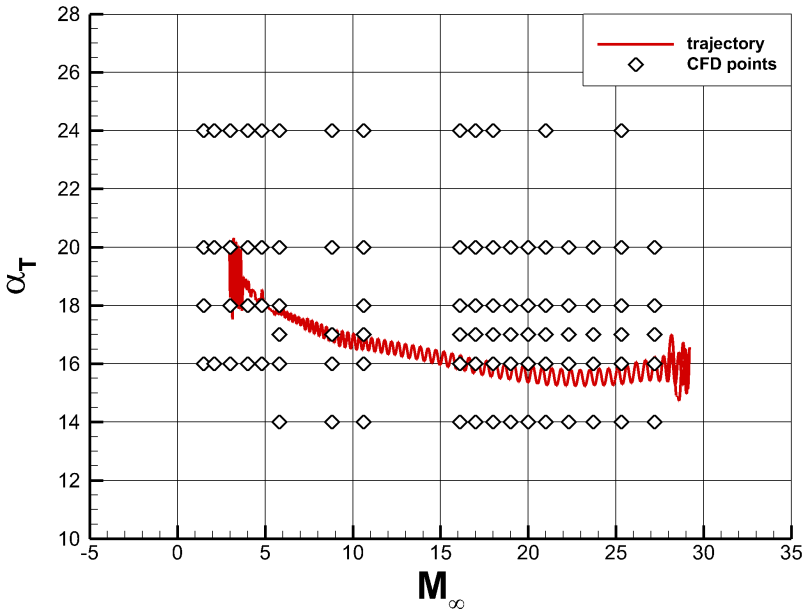

(a) Nominal Flight α_T and CFD Point Coverage

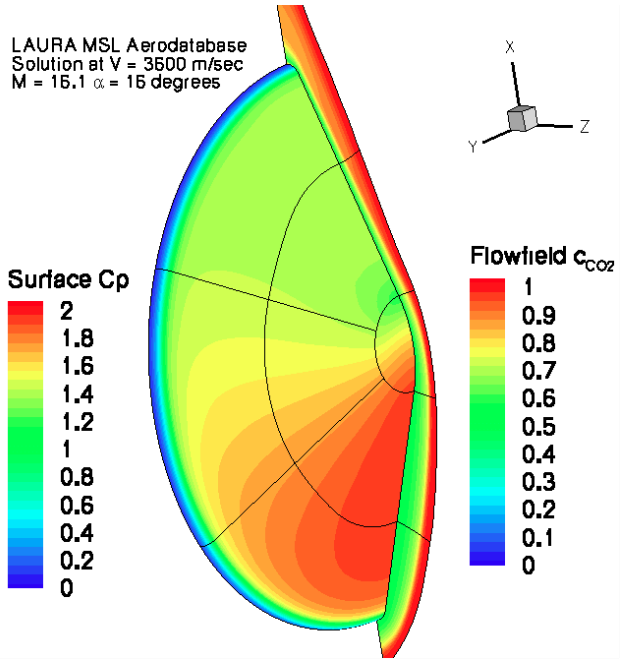

(b) Representative LAURA Solution

Figure 2.2: CFD Solutions

the current nominal trajectory 12-GAL-01, where t=0 is defined as the point of entry interface, and curves are plotted over the portion of the trajectory where dynamic pressures exceed 850 Pa.

The CFD database pressures were nondimensionalized using the freestream pressure and dynamic pressure of each solution. The nondimensionalization transforms the forebody pressures into

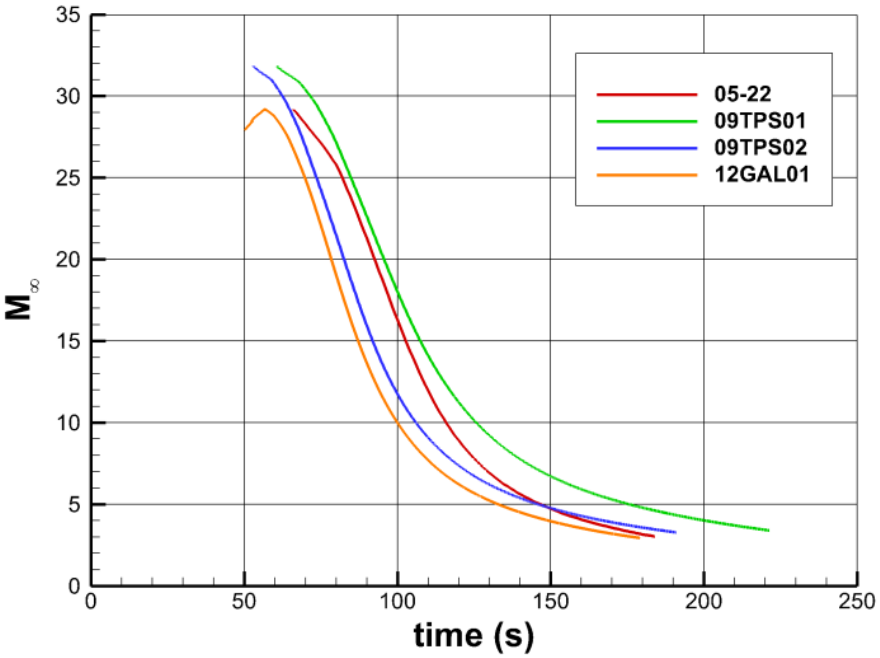

(a) Mach Number

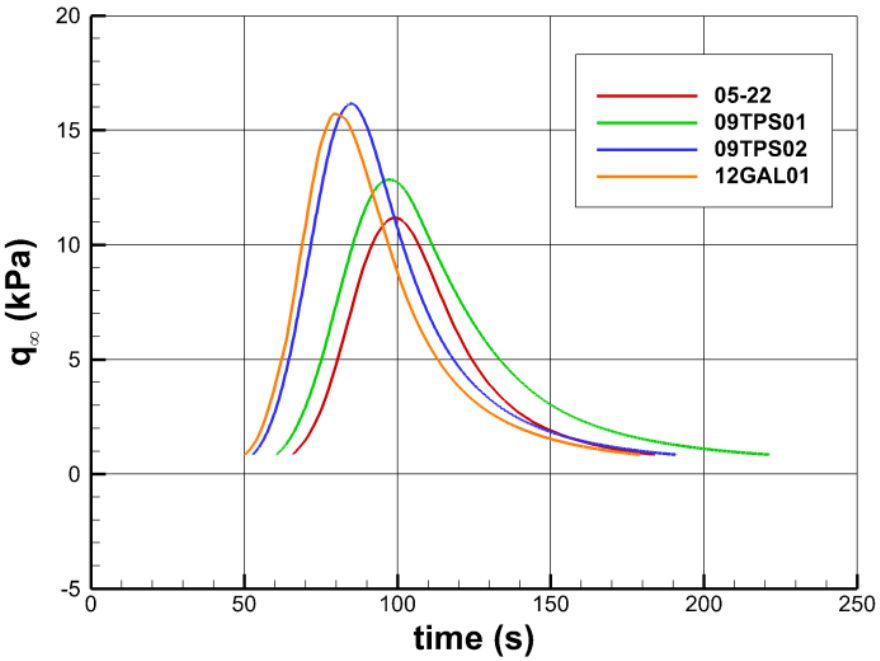

(b) Dynamic Pressure

Figure 2.3: Comparison of Mach Number and Dynamic Pressure Along Different Trajectories

pressure coefficients, defined as $C_p = (p - p_\infty)/q_\infty$. Modeling the surface pressures in coefficient form allows the CFD solutions to be used across a wide range of trajectories with different density and velocity profiles. The data were re-interpolated from the 7 block grid to a single-zone grid of

clock and cone angles. This alteration simplifies the interpolation of surface conditions without the complications of search routines required to handle multiple zones. Each CFD matrix point consists of a full surface pressure distribution solution, with 37 clock angles in uniform 5 degree increments and 61 cone angles with non-uniform increments. These matrix points can be interpolated as needed to provide estimates of the pressure distribution at any point on the aeroshell.

The nominal MEADS pressure model is a tabulation of the nondimensional pressure coefficient Cp at each MEADS port mapped over (M, α_T, ϕ) space, where all data are taken from nominal Mars entry simulations along the 05-22 trajectory. The dimensionless form is used so that changes in absolute surface pressure are scaled according to the freestream dynamic pressure for any desired trajectory. The tables were constructed from LAURA results by extracting surface pressure coefficients from each (M,α_T) solution at the MEADS port locations, then rotating the solution about the body axis by a roll angle increment and repeating as necessary to fill the desired (α,β) space. As MSL's absolute angle of sideslip is predicted not to exceed 1 degree during the portion of nominal flight where freestream dynamic pressure exceeds 850 Pa, the tables have been constructed for each (M, α_T) over the range $-9 \leq \phi \leq 9$ in 3 degree increments, providing for more than adequate coverage in β space. For nonlifting flight after balance mass jettison, the tables are constructed over the entire roll angle range from $-180 \leq \phi \leq 180$, using the same 3 degree increments in order to cover the entire possible range of vehicle attitude. In addition to the surface pressure coefficient, the magnitude of its gradient was also calculated using an internal Tecplot function and tabulated for use in the pressure uncertainty model, where it is part of a port location uncertainty expression.

2.3 Experimentation and Simulation

Note that the pressure model utilized for atmospheric state estimation is based entirely on these tabulated CFD solutions. The CFD modeling approach was validated in air in wind tunnel experiments at Mach numbers of 2.5, 3.5, 4.5, and 10. Residuals between computed and measured pressures were within the measurement accuracy obtained in the wind tunnel experiments.

Wind-tunnel experiments were conducted in the NASA Langley Research Center (LaRC) Unitary Plan Wind Tunnel (UPWT) with a 6-inch diameter MSL pressure model at Mach numbers from 2.5 to 4.5. Two tunnel entries were undertaken, one in 2010 and another in 2011. Test 1835 was the first UPWT entry and utilized a single model/sting configuration, whereas the second entry, test 1855, utilized three model/sting configurations in an attempt to keep the model in the same region of the test section regardless of angle of attack. Test 1855 data showed significant variability in pressure measurements due to changes in the model location within the test section, as shown in Fig. 2.4. Flow surveys show that the UPWT has nonuniform Mach number and flow angularity throughout the test section, and that these changes can occur over length scales of the same order as the wind tunnel model diameter [23]. A study of pressure error correction techniques based on flow survey data were outside the scope of this work.

UPWT experiments were simulated with the LAURA code, using a calorically perfect gas model with the properties of air. The CAD model from which the test article was made was used as the surface definition for the computational volume grid, which was composed of 18 blocks and a total of 0.77 million points. Cases were run over the angle of attack range $0 \leq \alpha \leq 32$ in 4 deg increments, at nominal Mach 2.5, 3.5, and 4.5 UPWT conditions, all using a constant temperature (300 K) viscous wall boundary condition. Grid points were clustered at the bow shock in order to improve its placement and reduce its apparent thickness, or "smear," as shown in Fig. 2.5.

Experimentation was carried out in the LaRC 31-inch Mach 10 tunnel using the same 6-inch diameter model as was used in the UPWT experiments. Experimental results indicated that mea-

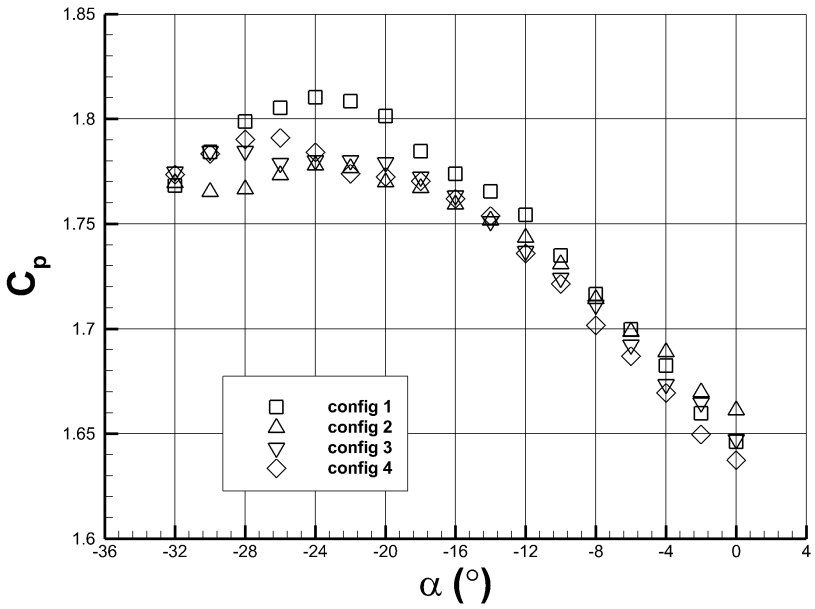

Figure 2.4: Variability in MEADS Port 1 Measurements due to Changes in Model Position

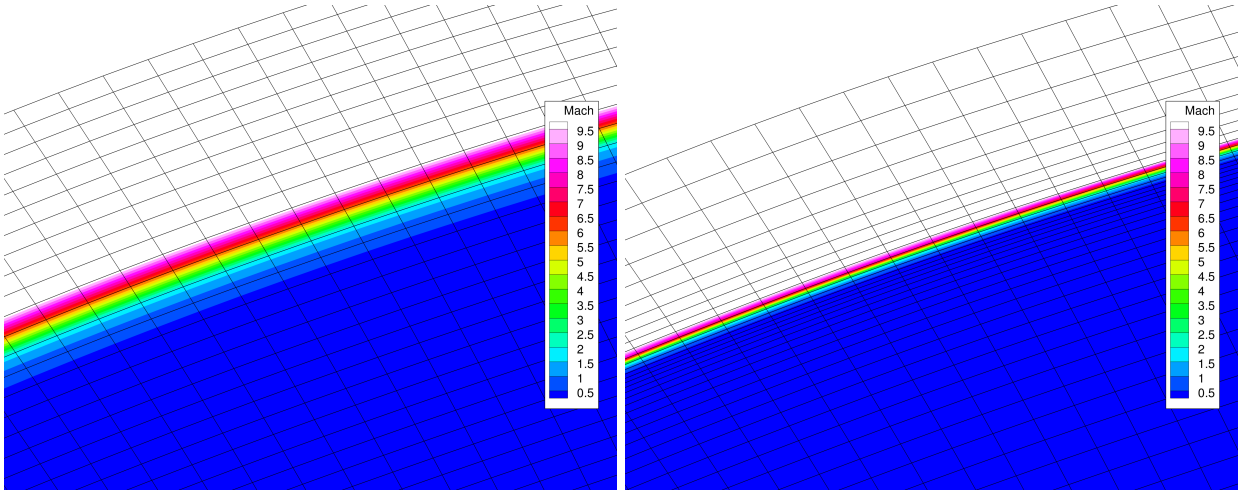

(a) Unclustered (b) Clustered

Figure 2.5: Grid Lines and Mach Contours at Bow Shock for Unclustered and Clustered Grids

sured forebody pressures were extremely sensitive to the model's location within the test section. These data are not used in the pressure or uncertainty models, but are useful to illustrate some of the difficulties and challenges associated with pressure model testing in hypersonic ground facilities, particularly when such experiments are carried out with the intent of validating computations. Simulations of the Mach 10 experiments were conducted using the LAURA code, using the same grids, models, and assumptions as the UPWT simulations.

Chapter 3

MEADS Transducer Calibration

A calibration of the MEADS fight system was conducted in order to compute input pressure as a function of voltage and sensor/electronics temperature. The MEADS calibration program carries two independent calibration efforts. The baseline approach utilizes the industry standard approach that has a long heritage and is referred to as the traditional method by the MEADS project. This method was used with great success by the SEADS program [5, 6] and other FADS programs such as the Aeroassist Flight Experiment (AFE) [24]. The second approach is a proof-of-concept experiment using a Design of Experiments (DOE) method. This calibration method has never before been used to calibrate space fight transducers prior to the MEADS program. The DOE approach is documented in [25, 26] and is not discussed further in this paper.

This chapter describes the calibration approach and the analysis of the final calibration data using the traditional calibration/analysis approach. The final calibration of the transducers was preceded by preliminary thermal testing and acceptance testing. This initial testing led to preliminary selection and rankings for both Flight and Flight Spare transducer sets. The result of this ranking and port assignments are given in Table 3.1.

3.1 Calibration Methodology: General Overview

The traditional calibration approach as applied to a FADS type pressure measurement system is composed of the collection of pressure transducer performance data and a data analysis process originally developed in support of the SEADS experiment. This report briefly describes the calibration data collection process and a detailed description of the analysis methodology and assumptions

Table 3.1: Port Assignments

Port	Flight Serial Number	Flight Spare Serial Number
1	022	026
2	025	020
3	029	031
4	021	030
5	032	027
6	023	034
7	024	036

using final transducer calibration data obtained by the traditional method.

The traditional method acquires a set of input pressure data vs. transducer output Voltage at various temperatures to define transducer sensitivity (scale factor), non-linearity, and bias (zero offset) as a function of temperature. The sensitivity and non-linearity data are collected by process that uses an increasing/decreasing application of pressure over the operating range of the transducer. (In the case of MEADS from zero to 5.5psi.) The number of pressure set points can vary depending on project requirements. Typically a total of 11-13 pressure points have proven to be sufficient in previous applications. A series of pressure versus Voltage output data sets (curves) are obtained at applicable operating temperatures to define the thermal sensitivity of the pressure sensitivity and zero offset. The number of temperature set points can also vary. Typically five temperature set points have proven to be adequate.

Other performance characteristics that are determined from the calibration data set are within test repeatability and pressure/temperature hysteresis. Repeatability is defined here as the amount of change of a measured reading at the same pressure and conditions over a series of pressure cycles from zero to full-scale pressure and back to zero again. To ensure no pressure hysteresis is introduced into repeatability measurements readings are always taken during an increase in pressure or a decrease in pressure but never a mixture of the two in the implementation of the Traditional method.

Typically, due to concerns related to the effect of long space missions where severe environments and test requirements can impact transducer performance, multiple full thermal calibrations are performed at different stages in the transducer acceptance and test process. These tests then allow the quantification of any performance variations that might result from time, environment, testing, and/or operation.

3.2 Implementation of Calibration Approach for MEADS

The MEADS mission and strain gauge pressure transducers configuration resulted in mission specific calibration requirements and a modified Traditional calibration approach. Due to MSL spacecraft constraints the transducer pressure head containing the strain gauge and the electronics were separated and located in regions on the spacecraft with different thermal environments. Additionally, MEADS required that the transducer performance be maximized at the low-pressure end of measurement range. As a result each transducer component - pressure head/strain gauge and electronics was calibrated as an independent variable. A thirteen point increasing/decreasing pressure sequence with a concentration at the lower end of the pressure scale calibration was performed. The final calibration matrix is shown in Table 3.2. Setpoints T2 - T6 are specific to the electronics while T7 - T13 are specific to the pressure head strain gauge. Setpoints T11 - T 13 were incorporated to provide test specific repeatability data due to previous indications relative to transducer thermal repeatability and hysteresis. All temperature setpoints make use of the same pressure sequence, given in Table 3.3.

Due to schedule constraints only one set of Traditional calibration data was collected for MEADS thus the ability to assess and quantify repeatability as a function of time, environmental effects and operation could not be accomplished.

Table 3.2: Calibration Temperature Setpoints

Setpoint Number	Transducer Temperature (deg C)	SSE Temperature (deg C)
T1	20	20
T2	-80	60
T3	-80	30
T4	-80	0
T5	-80	-20
T6	-80	-30
T7	-50	0
T8	-80	0
T9	-100	0
T10	-125	0
T11	-100	0
T12	-80	0
T13	-50	0
T14	20	20

Table 3.3: Pressure Sequence

Sequence Number	Pressure (psi)
1	0.00
2	0.25
3	0.50
4	1.00
5	2.00
6	3.30
7	4.50
8	5.50
9	3.90
10	2.50
11	1.50
12	0.75
13	0.00

3.3 Calibration Analysis: Methodology and Assumptions

The traditional calibration method uses a least-squares fit for each transducer to a model of the form [6]

$$p = a_0\left(T_1, T_2\right) + a_1\left(T_1, T_2\right) V + a_2\left(T_1, T_2\right) V^2 \tag{3.1}$$

where T_1 is the pressure transducer temperature, T_2 is the SSE temperature, V is the Voltage output, and p is the pressure. The coefficients a_0, a_1, and a_2 are termed the bias, sensitivity, and non-linearity, respectively. These coefficients are determined from a least-squares fit of pressure vs. Voltage at specific temperature setpoints using a simple increasing/decreasing applied pressure to create the Voltage response. By varying the temperature setpoints, a database of calibration coefficients can be constructed, and an empirical model developed that uses spline interpolation to look up the values of these coefficients and functions of the two temperatures.

The specific calculations performed at each temperature setpoint is provided in the following. First, the matrix $\boldsymbol{F}$ is defined as

$$\boldsymbol{F} = \begin{bmatrix} 1 & V_1 & V_1^2 \\ \vdots & \vdots & \vdots \\ 1 & V_n & V_n^2 \end{bmatrix} \tag{3.2}$$

where n is the total number of pressure points at each temperature setpoint. Similarly, the array of pressure measurements is written as

$$\boldsymbol{p} = \begin{bmatrix} p_1 & \cdots & p_n \end{bmatrix}^T \tag{3.3}$$

The coefficient array is written as $\boldsymbol{\xi} = \begin{bmatrix} a_0 & a_1 & a_2 \end{bmatrix}^T$. The least-squares estimate of the coefficient array is given by

$$\hat{\boldsymbol{\xi}} = \left(\boldsymbol{F}^T\boldsymbol{F}\right)^{-1}\boldsymbol{F}^T\boldsymbol{p} \tag{3.4}$$

An important byproduct of the least-squares solution is the covariance matrix of the coefficient estimate, given by

$$\mathrm{Cov}\left(\hat{\boldsymbol{\xi}}\right) = \sigma_c^2\left(\boldsymbol{F}^T\boldsymbol{F}\right)^{-1} \tag{3.5}$$

where σ_c is the Mensor pressure controller accuracy. Along with the values of the calibration coefficient, the uncertainties in the coefficients are also stored as a function of the two temperatures. These uncertainties can be used to build a calibration error model to assess system performance. The total system uncertainty model from the calibration also needs to consider the temperature uncertainties and hysteresis. To this end, define

$$\boldsymbol{z} = \begin{bmatrix} T_1 & T_2 & V & a_0 & a_1 & a_2 \end{bmatrix}^T \tag{3.6}$$

It follows from a linear covariance transformation that the total pressure prediction error variance is given by

$$\sigma_p^2 = \left(\frac{\partial p}{\partial \boldsymbol{z}}\right)\boldsymbol{\Omega}_z\left(\frac{\partial p}{\partial \boldsymbol{z}}\right)^T + \tilde{\sigma}_{a_0}^2 + \tilde{\sigma}_{a_1}^2 V^2 + \tilde{\sigma}_{a_2}^2 V^4 \tag{3.7}$$

where

$$\boldsymbol{\Omega}_z = \begin{bmatrix} \sigma_{T_1}^2 & 0 & 0 & \mathbf{0} \\ 0 & \sigma_{T_2}^2 & 0 & \mathbf{0} \\ 0 & 0 & \sigma_V^2 & \mathbf{0} \\ \mathbf{0} & \mathbf{0} & \mathbf{0} & \mathrm{Cov}\left(\hat{\boldsymbol{x}}\right) \end{bmatrix} \tag{3.8}$$

The quantities $\tilde{\sigma}_{a_0}^2$, $\tilde{\sigma}_{a_1}^2$, and $\tilde{\sigma}_{a_2}^2$ account for non-repeatability and hysteresis in the bias, sensitivity, and nonlinearity coefficients in the calibration equation, respectively. These contributions to the uncertainty model are computed from repeated points in the calibration temperature setpoints. In summary, the uncertainty predictions include non-repeatability/hysteresis, calibration error, temperature error, and Voltage error/noise. Note that in this model the temperature uncertainty due to thermocouple bias and noise are lumped together into the total temperature uncertainty.

The in-flight zero obtained prior to Mars entry has the effect of significantly reducing the uncertainties in the pressure data. Essentially, the in-flight zero nearly removes the uncertainties due to bias, but the slope and nonlinearity uncertainties remain, and a small residual bias error remains due to the slope of the bias curve as a function of temperature, coupled with temperature uncertainty and noise. An example of the effect of the in-flight zero is shown in Figure 3.1 based on data from Transducer 022 at temperature setpoint T4 (Transducer temperature -82.9 C and SSE temperature 9.7 C). Figure 3.1(a) shows the pressure vs. Voltage curve from the calibration data for the (true) Mensor controller pressure and the estimates pressure with and without the in-flight zero applied. On this scale, the transducer behaves very linearly with a small correction / bias shift due to the in-flight zero. Figure 3.1(b) shows the pressure error with and without the correction. On this scale, a hysteresis loop and the bias correction due to the in-flight zero can be observed.

To develop an uncertainty model, let T_1^* and T_2^* be the transducer and SSE temperatures, respectively, and V^* be the measured Voltage at the time of the in-flight zero prior to atmospheric entry. Then the pressure error is

$$\delta p = a_0\left(T_1^*, T_2^*\right) + a_1\left(T_1^*, T_2^*\right) V^* + a_2\left(T_1^*, T_2^*\right)\left(V^*\right)^2 \tag{3.9}$$

It follows that the adjusted pressure is given by

$$\hat{p} = p - \delta p \tag{3.10}$$

By substituting Eq. (3.9) into Eq. (3.10) and linearizing for small temperature errors, the pressure measurement uncertainty model following the in-flight zero is given by

$$\begin{aligned}\sigma_p^2 &= \left(\frac{\partial a_0}{\partial T_1}\right)^2 \sigma_{n_1}^2 + \left(\frac{\partial a_0}{\partial T_2}\right)^2 \sigma_{n_2}^2 + \left[\sigma_{a_1}^2 + \tilde{\sigma}_{a_1}^2 + \left(\frac{\partial a_1}{\partial T_1}\right)^2 \left(\sigma_{b_1}^2 + \sigma_{n_1}^2\right) + \left(\frac{\partial a_1}{\partial T_2}\right)^2 \left(\sigma_{b_2}^2 + \sigma_{n_2}^2\right)\right] V^2 \\ &\quad + \left[\sigma_{a_2}^2 + \tilde{\sigma}_{a_2}^2 + \left(\frac{\partial a_2}{\partial T_1}\right)^2 \left(\sigma_{b_1}^2 + \sigma_{n_1}^2\right) + \left(\frac{\partial a_2}{\partial T_2}\right)^2 \left(\sigma_{b_2}^2 + \sigma_{n_2}^2\right)\right] V^4 \end{aligned} \tag{3.11}$$

where σ_{n_1}, σ_{b_1}, σ_{n_2}, and σ_{b_2} are the thermocouple noise and bias uncertainties for temperature measurements T_1 and T_2, respectively.

3.4 Analysis of Final Calibration Data

Data from the final calibration of the MEADS/SSE system were analyzed according to the methodology described in the preceding section. The traditional data points collected during the calibration are shown in Table 3.2. The desired vs. actual temperature setpoints acquired in the calibration are shown in Fig. 3.2 for the Flight and Flight Spare calibrations. Additional data were collected for the DOE calibration, which included several "pressure profiles" that attempt to simulate the pressures during Mars entry. No data were excluded from these datasets, although the ambient test points were analyzed but are not incorporated into the flight data reduction database since these points are not within the flight temperature space. No other data was utilized for the purposes of this calibration report, including ambient performance tests and acceptance testing data.

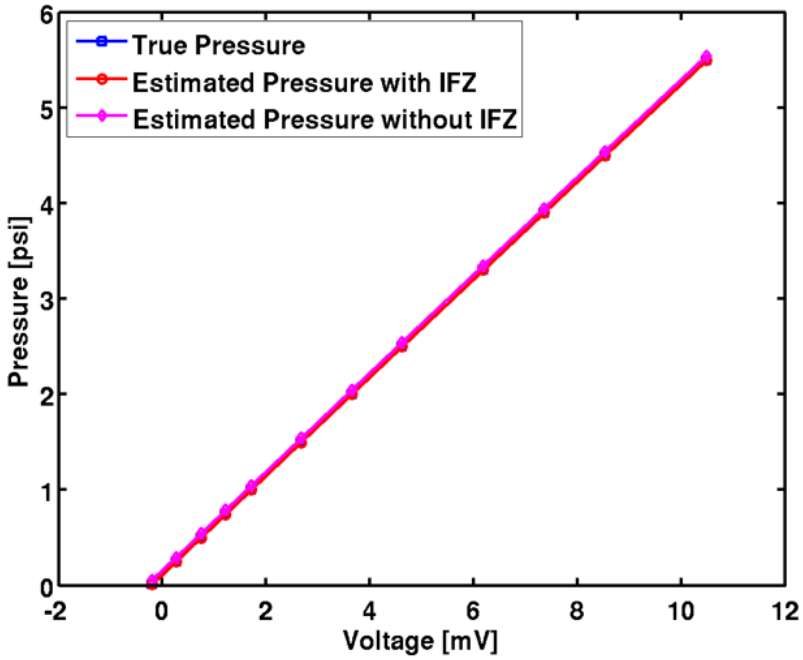

(a) Pressure

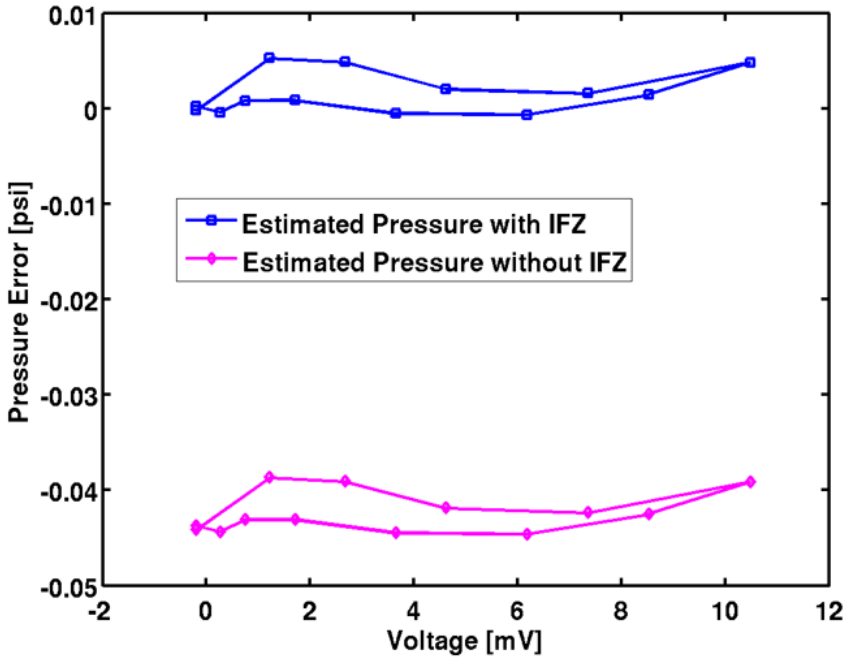

(b) Pressure Error

Figure 3.1: Effect of In-Flight Zero

Recall that replications are made involving temperature setpoints (T1,T14) at ambient, (T4, T8, T12) at -80/0, (T7, T13) at -50/0 and (T9, T11) at -100/0. These replications allow the repeatability and hysteresis of the transducer to be evaluated. Both the Flight and Flight Spare

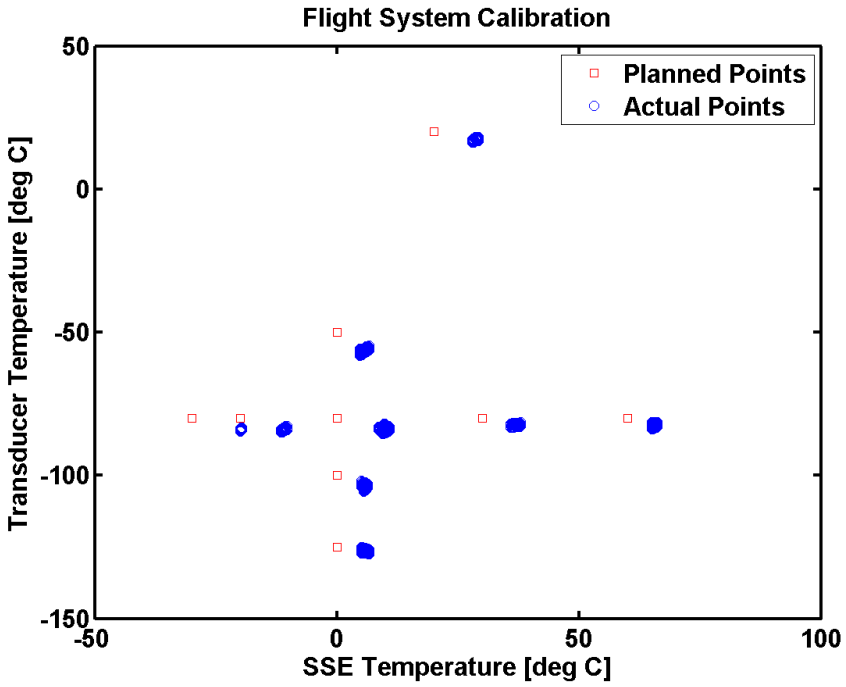

(a) Flight System

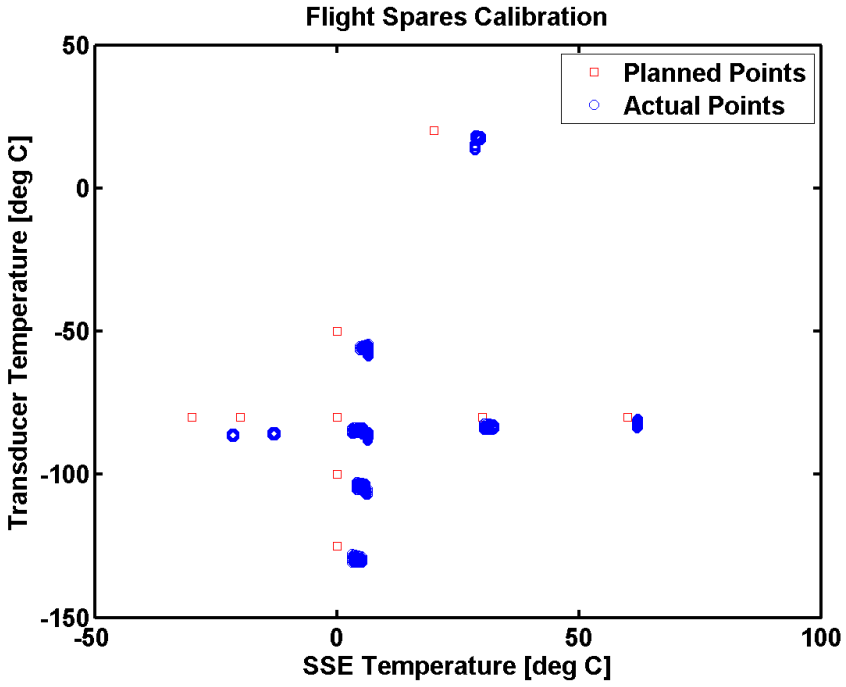

(b) Flight Spare System

Figure 3.2: Temperature Set Points

transducers make use of the same temperature set points in order to enable direct comparisons between both systems.

The non-repeatability/hysteresis uncertainties were calculated from the repeated temperature

Table 3.4: Flight Transducer Non-Repeatability/Hysteresis Uncertainties

Transducer Serial Number	$\tilde{\sigma}_0$ Bias Uncertainty [% FS]	$\tilde{\sigma}_1$ Sensitivity Uncertainty [% FS/mV]	$\tilde{\sigma}_2$ Nonlinearity Uncertainty [% FS/mV^2]	Within Temp. Repeatability [% FS]	Between Temp. Repeatability [% FS]
020	0.348	7.98e-3	4.12e-4	0.051	0.347
021	0.838	1.06e-2	6.12e-4	0.060	0.735
022	1.233	7.38e-3	5.81e-4	0.060	1.078
023	0.658	5.04e-3	4.91e-4	0.067	0.573
024	0.470	3.62e-3	3.03e-4	0.042	0.414
025	0.769	8.87e-3	4.03e-4	0.065	0.684
026	0.407	7.50e-3	4.16e-4	0.048	0.407
027	0.225	9.31e-3	6.11e-4	0.042	0.225
029	0.914	5.79e-3	3.50e-4	0.059	0.801
030	0.633	8.23e-3	4.83e-4	0.071	0.613
031	0.428	8.48e-3	6.11e-4	0.064	0.416
032	0.619	9.96e-3	6.75e-4	0.054	0.545
034	0.937	3.35e-2	3.01e-3	0.046	0.960
036	0.945	1.25e-2	9.25e-4	0.040	0.956

setpoints listed above. The results for the transducers are shown in Table 3.4. This table shows the 1-σ uncertainties in the calibration equation coefficients used in the uncertainty modeling, with pressure units in percent full scale. It is possible to generate rankings based on any of these uncertainties, but it is not recommended, since the total system uncertainty is a preferable metric as it includes all uncertainty sources together. However, several interesting observations can be made about this data. Namely, transducer 024 has the lowest uncertainty in all three coefficients among the Flight set. Many transducers from the Flight Spares set (020, 026, 027, and 031) have slightly better bias uncertainty than 024, but 024 exhibits the best sensitivity and nonlinearity uncertainty among all transducers. Transducer 034 is an outlier in the sense that its sensitivity and nonlinearity uncertainties are an order of magnitude larger than all other transducers. Also shown in these tables are the Within and Between Temperature Repeatability uncertainties. These uncertainties are utilized by the DOE method and are shown here simply for comparison purposes. Details on how these uncertainties are calculated can be found in [27]. Interestingly, the between temperature repeatability trends correlate with the bias uncertainties.

The quadratic calibration equation coefficients were calculated from the least-squares fit to the pressure/Voltage data across all temperature setpoints in the region of interest to flight data reduction (i.e. T2-T13). Next, the repeated points were averaged together and extrapolations were conducted, treating the transducer temperature and SSE temperature as independent variables, to create data tables suitable for 2-Dimensional look-up routines to determine the pressure as a function of Voltage, transducer temperature, and SSE temperature. The look-up tables are tabulated in Appendix A. For the results described in this document, the Matlab-based griddata routine was utilized to perform the look-ups, using the cubic interpolation method. The linearizations required for calculating the uncertainty estimates are computed using a centered divided difference method with 0.5 deg C temperature perturbations.

The resulting calibration model was utilized to predict the DOE and Pressure Profile data (with and without the simulated in-flight zero) to asses performance of the model itself as well as the

Table 3.5: Flight Transducer Non-Repeatability/Hysteresis Uncertainties

Transducer Serial Number	DOE Actual RMS Error [% FS]	DOE Predicted RMS Error [% FS]	Profile Actual RMS Error [% FS]	Profile Predicted RMS Error [% FS]	Profile Actual RMS Error [% FS]	Profile Predicted RMS Error [% FS]
020	0.385	0.408	0.217	0.404	0.214	0.080
021	0.928	0.805	0.841	0.801	0.229	0.074
022	1.326	1.200	1.316	1.197	0.245	0.067
023	0.660	0.655	0.600	0.654	0.138	0.085
024	0.460	0.459	0.392	0.458	0.110	0.045
025	0.816	0.756	0.750	0.754	0.175	0.045
026	0.705	0.497	0.174	0.497	0.182	0.066
027	0.251	0.266	0.252	0.263	0.194	0.087
029	0.962	0.891	1.008	0.890	0.173	0.079
030	0.630	0.708	0.414	0.707	0.302	0.042
031	0.356	0.470	0.279	0.465	0.196	0.076
032	0.680	0.610	0.677	0.606	0.171	0.049
034	1.277	1.055	0.704	1.038	0.667	0.102
036	0.884	1.039	0.624	1.037	0.467	0.057

uncertainty predictions based on the linear covariance transformations. The results are tabulated in Table 3.5. These results show that the predicted uncertainties agree with the actual uncertainties reasonably well. The in-flight zero uncertainty predictions do not match as well as the other cases, but this difference could be due to how the profiles were executed during the calibration. Further analysis is required to show this is the case.

Based on these results it is possible to generate rankings of transducer performances based on the in-flight zero results, which are the most representative of actual system performance. Sorted in ascending order, the recommended flight system ranking is 024, 023, 032, 029, 025, 021, and lastly 022. Since the best two transducers are currently assigned to ports 6 and 7, recommendations were made to re-order the port assignments in order to improve the dynamic pressure and angle of attack performance. Due to schedule constraints it was not possible to do so.

3.5 Uncertainty Analysis

An analysis of uncertainties from the final calibration data was conducted to examine transducer performance relative to system requirements of 0.5% accuracy of pressure reading. The analysis described in this section is based on the 09-HOL-01 nominal trajectory. The nominal port pressures along this trajectory are shown in Figure 3.3. The 850 Pa dynamic pressure boundaries are indicated, as well as the 5 psi full scale pressure threshold.

The calibration uncertainties along the reference trajectory are shown in Figure 3.4. Note that the error uncertainties are shown as a percent of reading. These uncertainties include the transducer calibration uncertainties alone, with all other error sources ignored and the in-flight zero applied. The errors are based on the 09-HOL-01 nominal trajectory. These curves have been generated using the expression for the error variance given in Section 3.3 with appropriate terms set to zero.

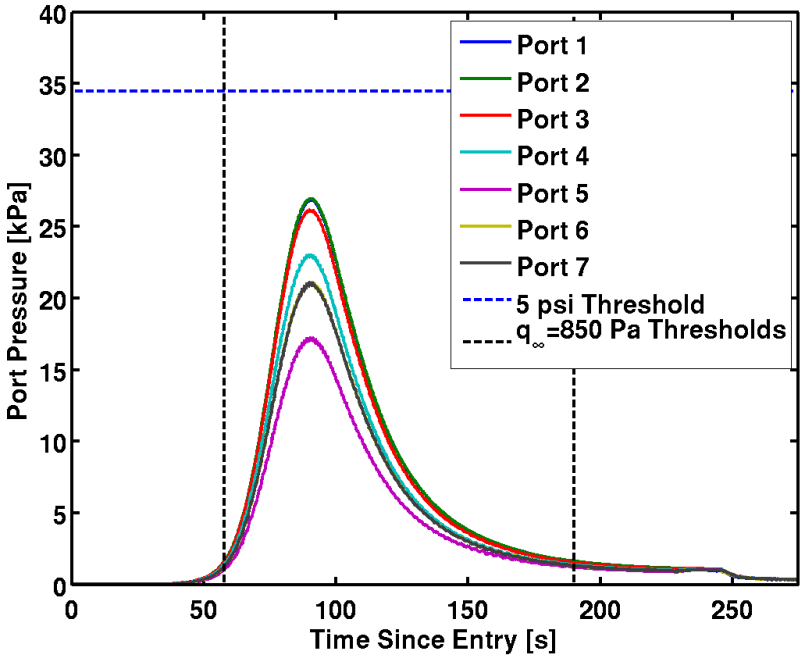

Figure 3.3: 09-HOL-01 Nominal Pressures

The reduced expression is

$$\sigma_p^2 = \left(\sigma_{a_1}^2 + \tilde{\sigma}_{a_1}^2\right) V^2 + \left(\sigma_{a_2}^2 + \tilde{\sigma}_{a_2}^2\right) V^4 \tag{3.12}$$

The error transformed into percent of reading is simply

$$\%Error = \left(\frac{\sigma_p}{p}\right) \times 100 \tag{3.13}$$

The uncertainty reduces to a constant value at zero pressure due to the limit being a ratio of two slopes. To a first-order approximation (equating 10 mV to 5 psi), an expression for the error as a function of pressure is

$$\Delta p = \epsilon_1 p + \epsilon_2 p^2 \tag{3.14}$$

where $\epsilon_1 = 2\Delta a_1$ and $\epsilon_2 = 4\Delta a_2$. The percent error reduces to

$$\%Error = \left(\frac{\sigma_p}{p}\right) \times 100 = (\epsilon_1 + \epsilon_2) \times 100 = 100\epsilon_1 + 100\epsilon_2 p \tag{3.15}$$

This result indicates that the percent error is a linear function of pressure, reaching a constant value at zero pressure and maximum value at peak pressure. Note that the percent error results are less than 0.5% for all transducers except 034 and 036. Transducer 036 has less than 0.5% error over most of the trajectory but exceeds slightly during the peak dynamic pressure regime. All other transducers meet the requirement of less than 0.5% error over the entire trajectory.

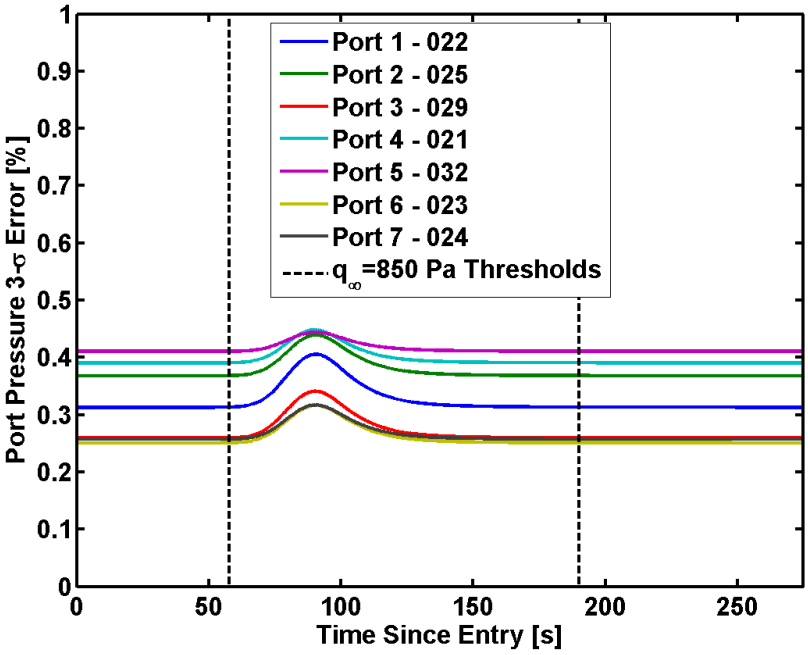

(a) Flight System

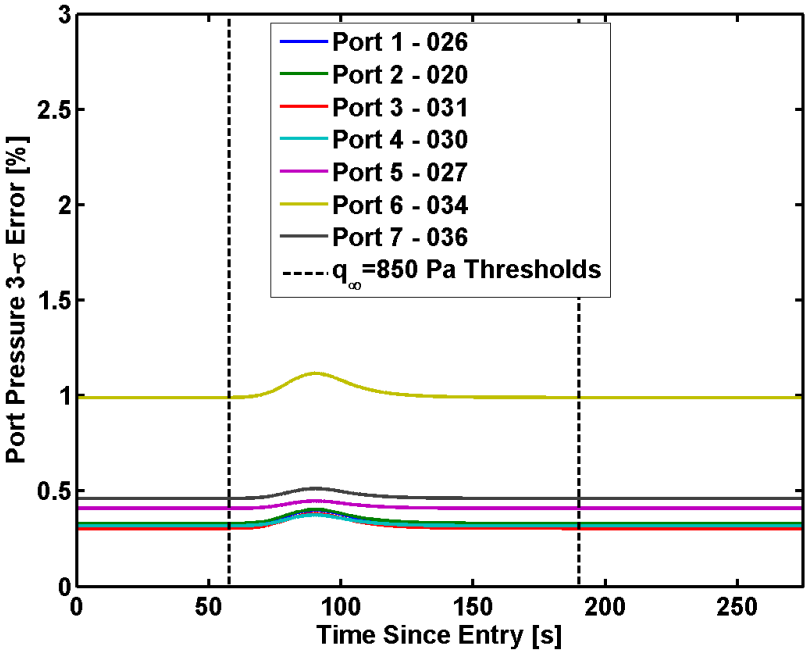

(b) Flight Spare System

Figure 3.4: Pressure Errors

Chapter 4

Uncertainty Modeling

At the MEDLI project outset, no top-down error budget was formulated to determine the hardware requirements. To meet the available schedule at the time, analysis or engineering judgment was used to identify the sources of error that were both (1) expected to contribute significantly to errors in the returned data, and (2) controllable through manufacturing. The MEADS Level 4 requirements were written to minimize uncertainties in the final data return. The hardware was then produced, calibrated, and integrated to the Level 4 requirements.

In parallel with MEADS hardware development, an error allocation was devised for the angle of attack and angle of sideslip data products. This error budget hierarchy is shown in Figure 4.1. The Level 2 requirement for angle of attack knowledge (PS-372) is +/- 0.5 degrees 3-sigma, shown in the top box of the hierarchy. The contributors to the uncertainty come from the transducer assembly, the Sensor Support Electronics, the Aeroshell manufacturing, and the system time latency. Each box lists the uncertainty requirement on that specific contributor, or the as-built value achieved, if applicable, and the error in angle of attack that results from that uncertainty. The following sections explain the analysis that produced these results.

The hierarchy for the angle of sideslip is identical except for the pressure transducer contribution to the errors; each of the seven transducers is unique, and sideslip takes advantage of the two ports and transducers that are symmetric about the vehicle centerline.

The impact of individual error sources and the effects of selected failure modes are examined in this chapter. These error sources include port location knowledge, sensor noise and quantization, telemetry time stamp errors, pneumatic lag, thermal transpiration, and system calibration uncertainties. Errors due to CFD pressure distribution uncertainties are also described in this chapter. The associated error models are reviewed in the following sections before showing sensitivity simulation results and the overall error budget results compared to the project requirements.

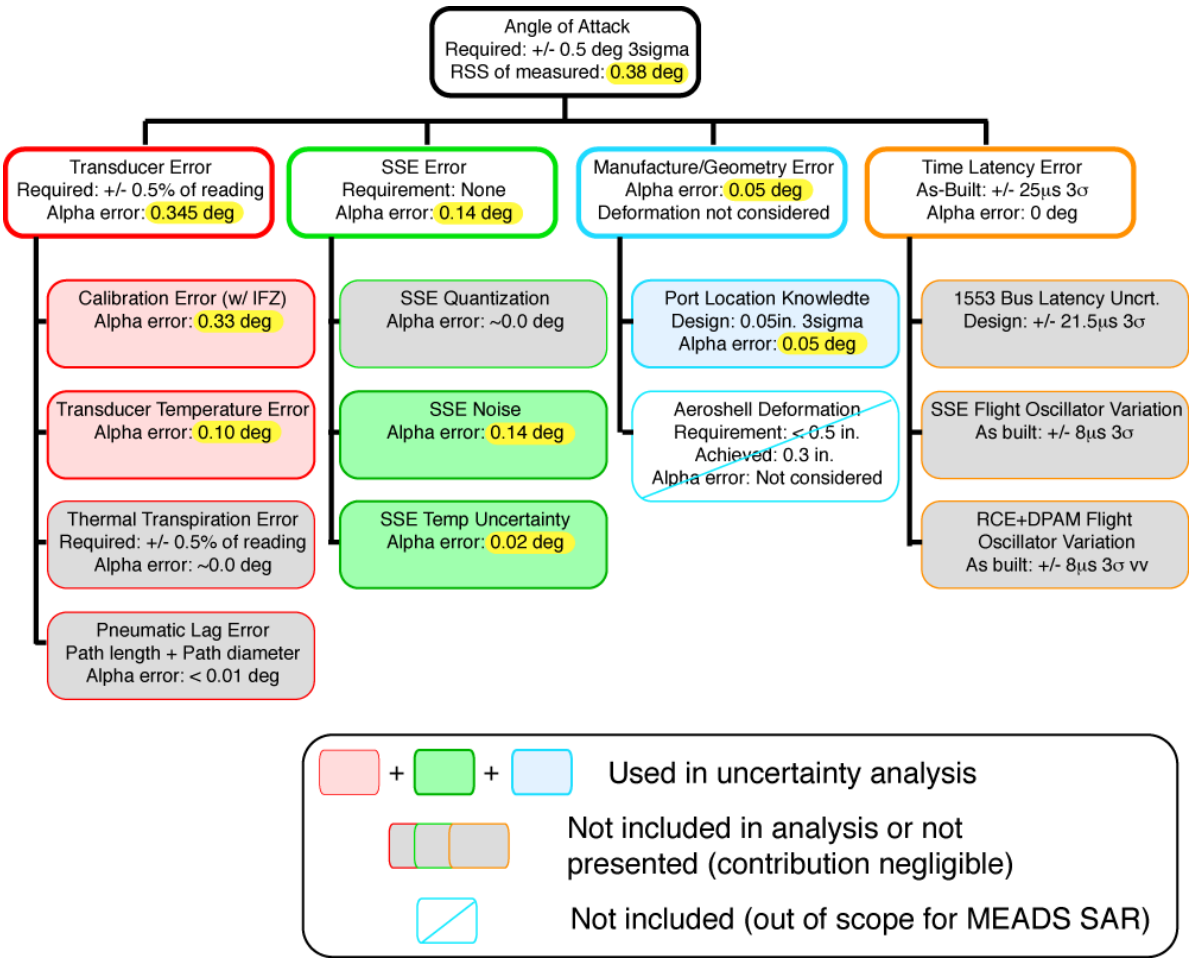

Figure 4.1: Angle of Attack Error Budget Hierarchy

4.1 Hardware System Error Models

4.1.1 Port Location Uncertainties

Errors in the knowledge of the port location after installation are cast as random longitudinal perturbations at constant clock angle and a random tangential perturbation at constant cone angle. The errors are specified as uncorrelated zero-mean Gaussian random numbers. The measurement system is accurate to within 0.04.

4.1.2 Sensor Noise and Quantization

Sensor noise is modeled using the equation

$$\delta p = (p_{max} - p_{min})\,\eta_p \tag{4.1}$$

where p_{max} and p_{min} are the maximum and minimum pressure range of the sensor system, respectively. The variable η_p is a uniform random variable between $\pm N/2^n$ where N is the number of counts of noise and n is the system effective bit size.

Sensor quantization can be modeled using the equation

$$\tilde{p} = \left(\frac{p_{max} - p_{min}}{2^n}\right) \text{Int}\left[\left(\frac{p}{p_{max} - p_{min}}\right) 2^n\right] \tag{4.2}$$

Finally, sensor saturation can be modeled as $\bar{p} = \max\left[\min\left(\tilde{p}, p_{min}\right), p_{max}\right]$.

4.1.3 Time Tag Error

Relative errors in the telemetry time stamp between measurements at different port locations introduces a distortion effect that corrupts the pressures used as input to the basic data reduction algorithm. Timing errors include both random and systematic components. The systematic timing errors can the adjusted in pre-processing of the flight data, leaving only the random error to be considered in error budgeting. These errors are simulated by first casting a uniform random number for each port in the range of $\pm 25\mu$s, and then shifting the truth state used to calculate the measured surface pressures.

4.1.4 Pressure Leak Rate Error

The MEADS pressure transducers cannot be tested with applied pressure once they are mounted on the MSL aeroshell, since contact with the PICA thermal protection system material is prohibited. Therefore, the project developed and tested an installation process that minimizes leaks along the pressure path. Pressure leak analysis is described in 28, 29.

Pressure system leaks can be modeled as a multiplicative loss on the measured pressure at the transducer relative to the port pressure. Since pressure leaks are a one-sided distribution, the errors can be reformulated as a two-sided distribution with half the total error by adjusting the pressure up, assuming the mean value of the leak rate. The adjusted pressure measurement is given by

$$\hat{p} = \left(1 + \frac{L_{max}}{2}\right) p \tag{4.3}$$

where L_{max} is the maximum expected leak rate, assuming that the leak rate is uniformly distributed. Following this adjustment, the pressure leak errors are uniformly distributed in the interval

$$\ell \in \mathcal{U}\left[-\frac{L_{max}}{2}, \quad \frac{L_{max}}{2}\right] \tag{4.4}$$

It then follows that the simulated pressure errors due to leaks are given by

$$\hat{p} = (1 + \ell)\, p \tag{4.5}$$

4.1.5 Vibration Error

Tests were performed to assess pressure error due to vibration during EDL. The tests were performed with 4 MEADS transducers (S/N 002, 028, 033, and 035) at 1.33 grms vibration conditions during a simulated pressure profile. Three vibration tests were performed for each axis of the transducer, where the y-axis test is directed along the pressure path. The measured transducer outputs from these tests are shown in Figures 4.2–4.4.

The noise due to vibration was then estimated from this test data. First, an "in-flight" zero was applied to the data to remove bias, and then residuals were computed between the true pressure and the measured pressure. These residuals were filtered using 1 Hz optimal Fourier filter. The

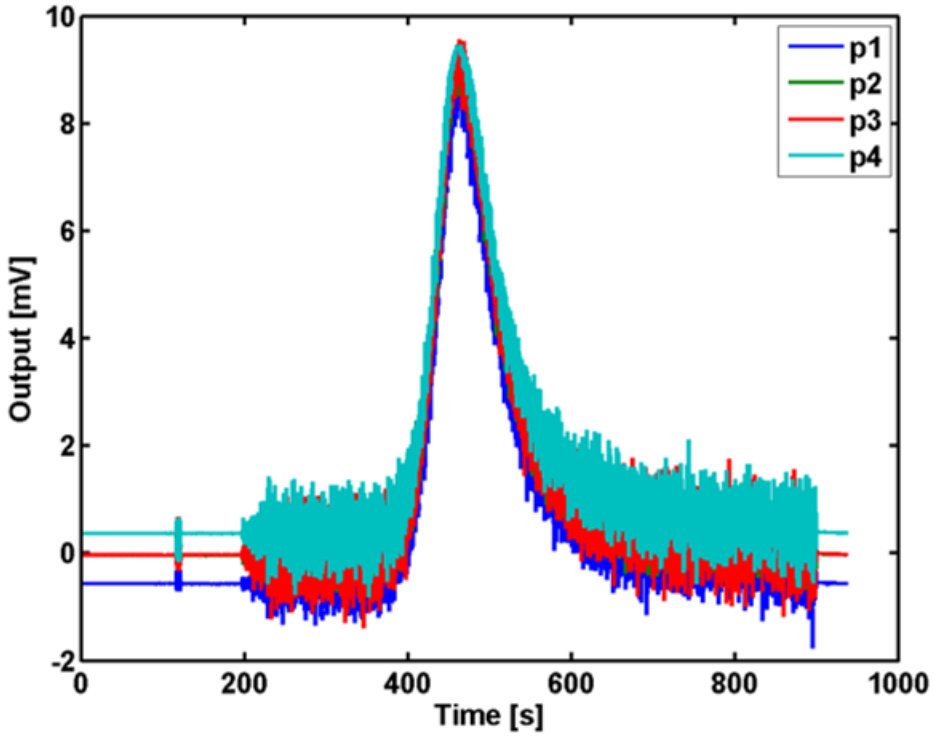

Figure 4.2: X-Axis Vibration Test Data

Table 4.1: Vibration Errors, 1σ % Full Scale

Transducer	Axis	Stationary Noise	Unfiltered Error	Filtered Error
P1	X	0.0135	2.5576	1.245
P2	X	0.0097	2.7153	1.2752
P3	X	0.0124	3.8236	1.7622
P4	X	0.0104	3.3704	1.6166
P1	Y	0.0102	3.8372	1.8969
P2	Y	0.0072	10.029	4.4757
P3	Y	0.0089	3.3062	1.559
P4	Y	0.0076	5.2139	2.5568
P1	Z	0.0167	0.4979	0.3481
P2	Z	0.0346	0.6368	0.3618
P3	Z	0.0143	0.4401	0.3044
P4	Z	0.0174	0.4994	0.3291

errors due to vibration were then computed from these filtered residuals. Error statistics from these residuals are shown in Table 4.1.

From these results, an uncertainty model of the form

$$\sigma_{noise} = \frac{q}{q_{max}} \sqrt{\sigma_{vibe}^2 - \sigma_0^2} \tag{4.6}$$

is introduced, where σ_{vibe} is the total measured error, σ_0 is the stationary noise uncertainty, and

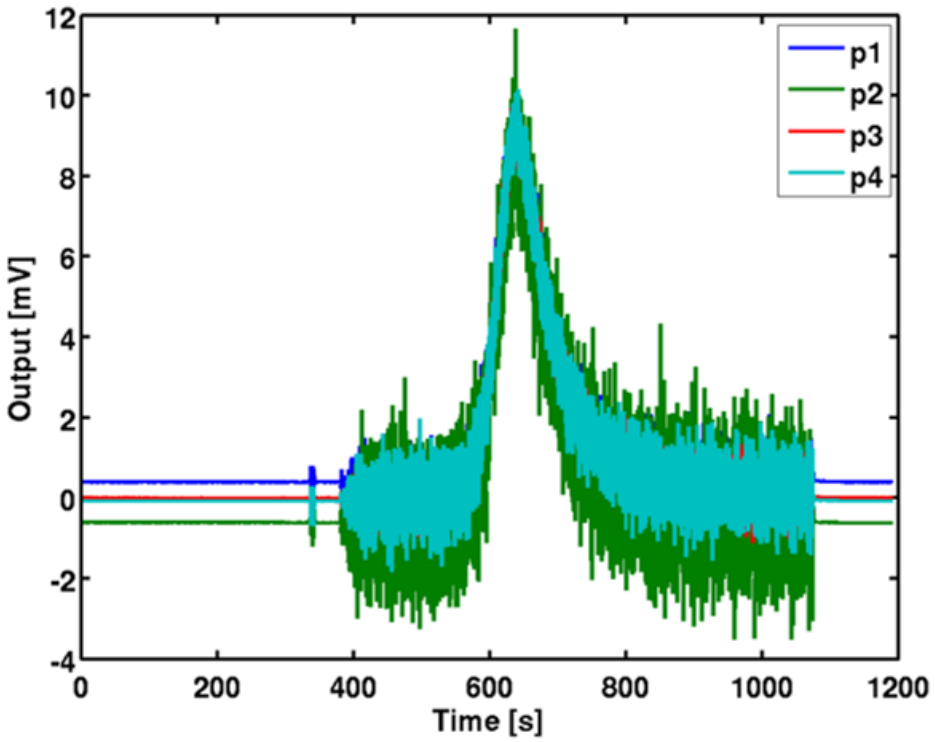

Figure 4.3: Y-Axis Vibration Test Data

σ_{noise} is the noise uncertainty due solely to vibration. The vibrational noise term is then scaled by the ratio of instantaneous dynamic pressure to the maximum dynamic pressure.

Next, a study of this noise model for different filtering frequencies was conducted. First, the errors introduced by filtering perfect data was studied. A 1 Hz filter and a 0.1 Hz filter were applied to the data. In this case, some true high frequency vehicle dynamics are removed by low pass filtering. This behavior is illustrated for the Port 5 pressure in Figure 4.5. Figure 4.5 shows the entire pressure profile, Figure 4.6 shows a detail view of the pressure at maximum dynamic pressure. Here it can be seen that the 0.1 Hz filter effectively removed all rigid body dynamics of the vehicle. Figure 4.7 shows the errors in pressure that arise due to filtering the truth data.

Figures 4.8 and 4.9 show a similar set of results for the case with 0.5% (of full scale) measurement noise at peak dynamic pressure. Figure4.10 shows the errors between unfiltered and filtered pressures at 1 and 0.1 Hz. Here, the 0.1 Hz filter has large errors because it has filtered the rigid body dynamics. The 1 Hz filter produces lower errors because it filters some of the noise while retaining the rigid body motion of the capsule oscillations.

A more stressful case is shown in Figure 4.11–4.13, in which the vibrational noise is set to 5% of the full scale pressure at peak dynamic pressure. In this case, the noise is large enough in amplitude that it dominates over the capsule's rigid body motions. As a result, the 0.1 Hz filter produces a better estimate of the true pressure. The results of these three experiments are summarized in Table 4.2, which show the 1-σ pressure errors over the entire trajectory for each case. These results indicate that the choice of filter cutoff frequency should be guided by the expected vibration noise environment. This is further illustrated in Figures 4.14–**??**, which shows power spectral densities for each of the three test cases, and for unfiltered, 1 Hz filter, and 0.1 Hz filter data. From these plots, it can clearly be seen that the vibration noise dominates over the rigid body modes as the

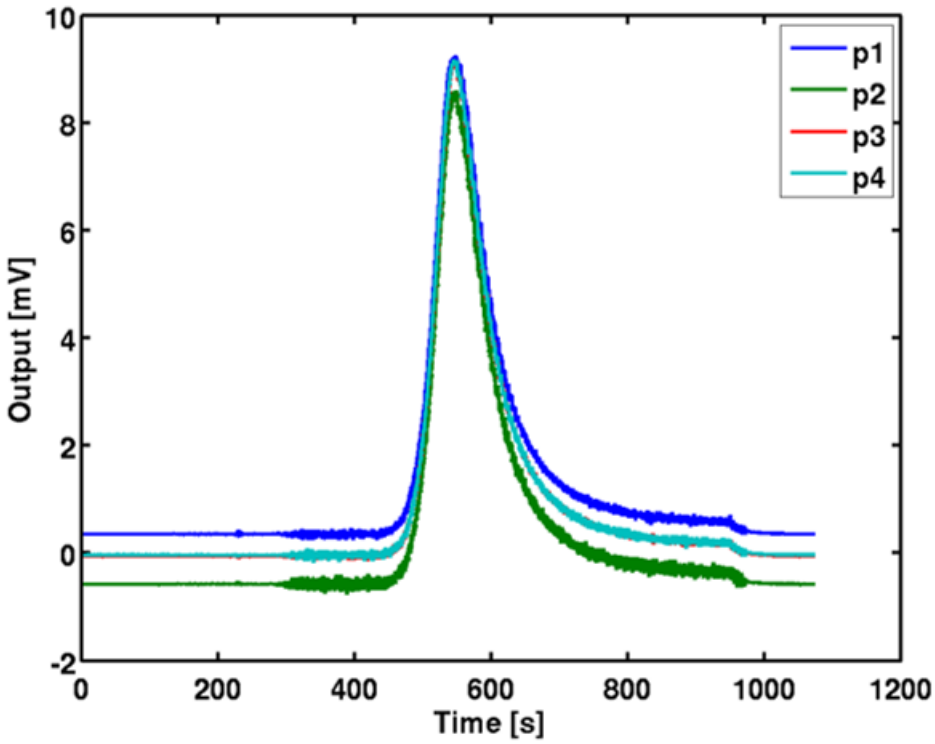

Figure 4.4: Z-Axis Vibration Test Data

noise level increases. Given these results and the expected noise environment based on vibration tests, the 1 Hz filter is recommended for use on MEADS data reduction.

Table 4.2: Pressure Errors over Trajectory, 1σ % Full Scale

	No Noise	0.5% FS Noise	5.0% FS Noise
Unfiltered	0.0	0.1596	1.5817
1 Hz filter	0.0471	0.0932	0.7289
0.1 Hz filter	0.1172	0.1193	0.2026

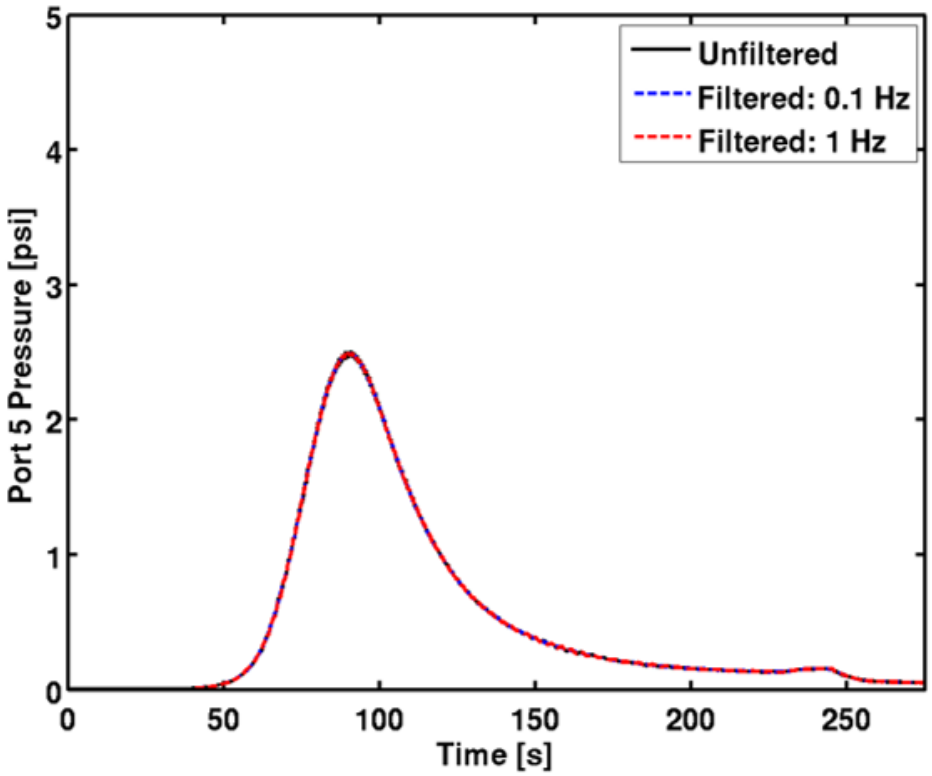

Figure 4.5: Port 5 Pressure: No Noise

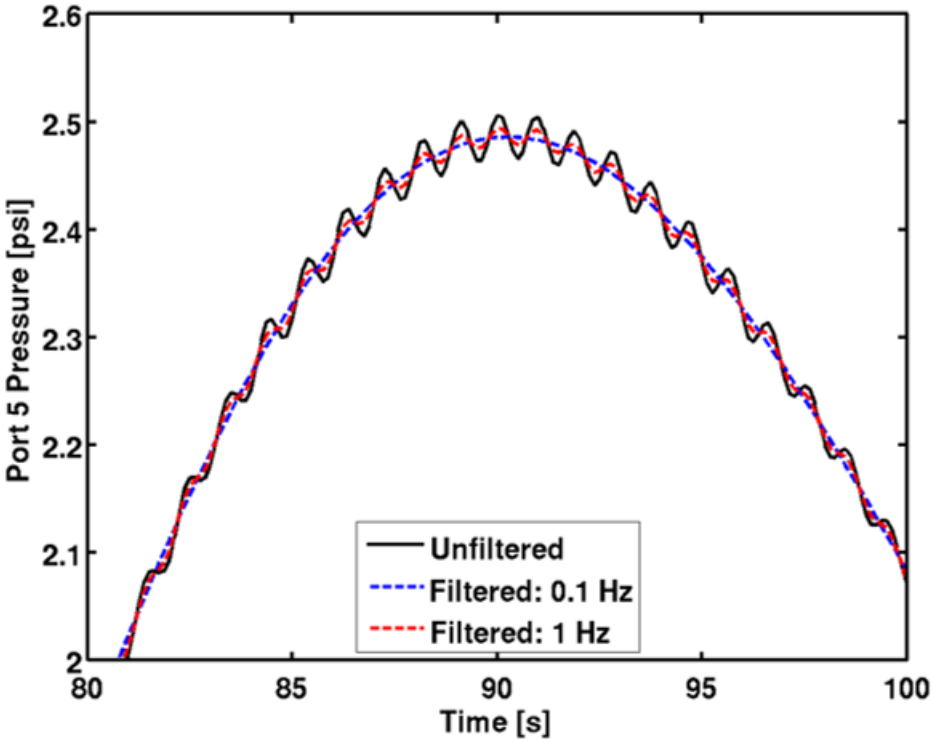

Figure 4.6: Port 5 Pressure: No Noise (Detail)

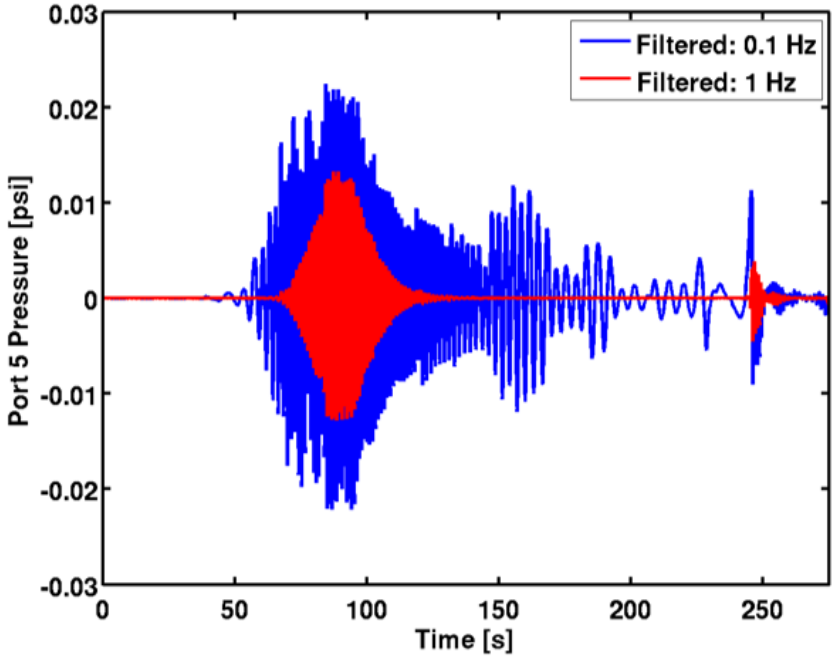

Figure 4.7: Pressure Error Due to Filtering

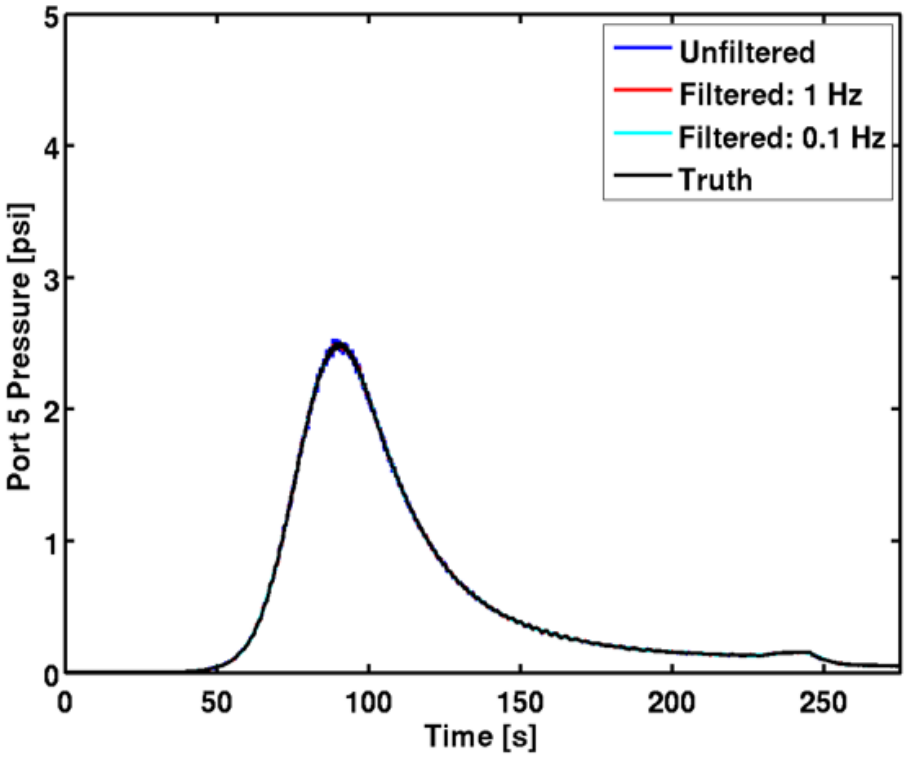

Figure 4.8: Port 5 Pressure: 0.5% Full Scale Noise at Maximum Dynamic Pressure

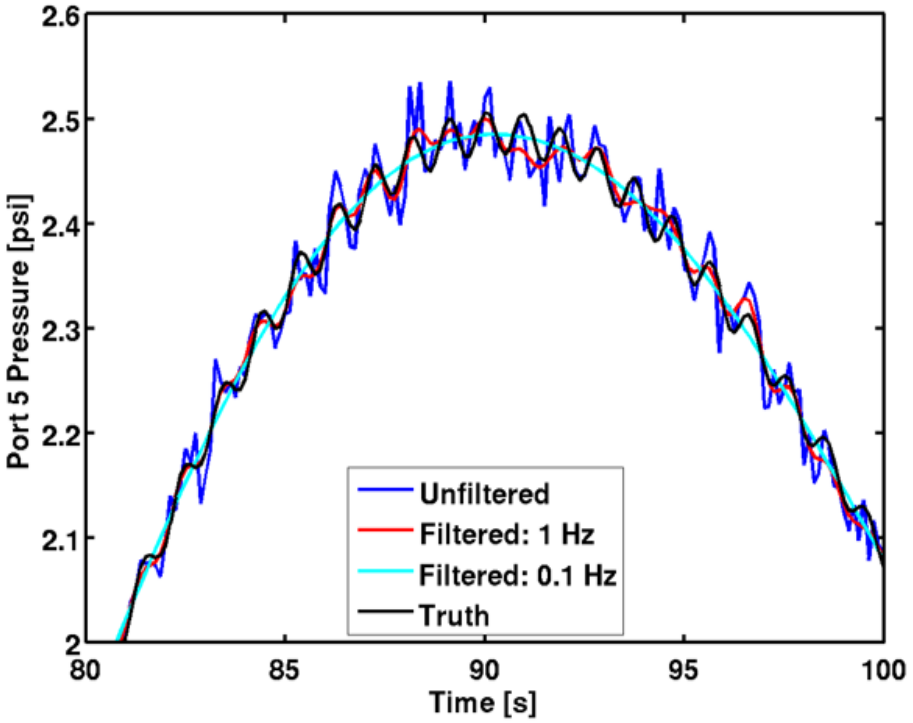

Figure 4.9: Port 5 Pressure: 0.5% Full Scale Noise at Maximum Dynamic Pressure (Detail)

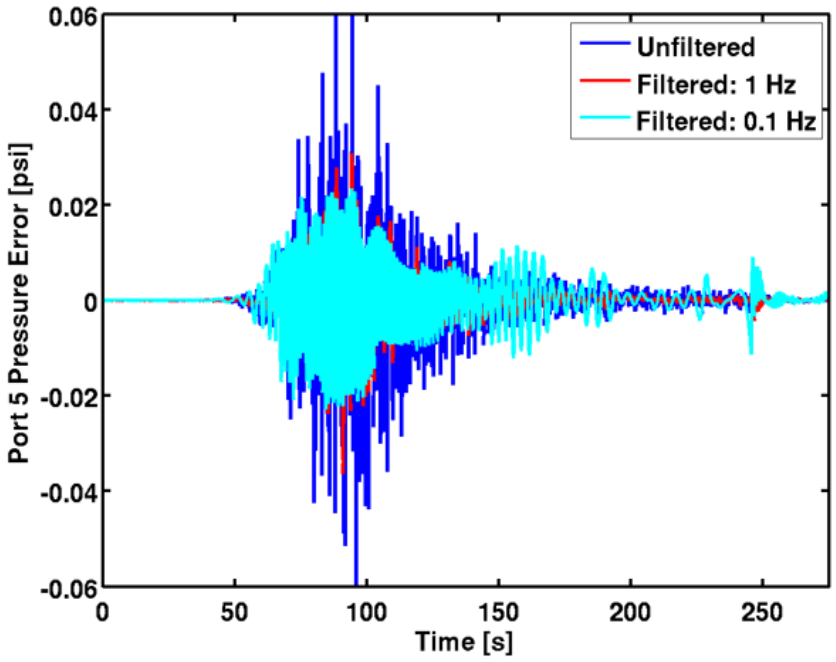

Figure 4.10: Pressure Error Due to Filtering

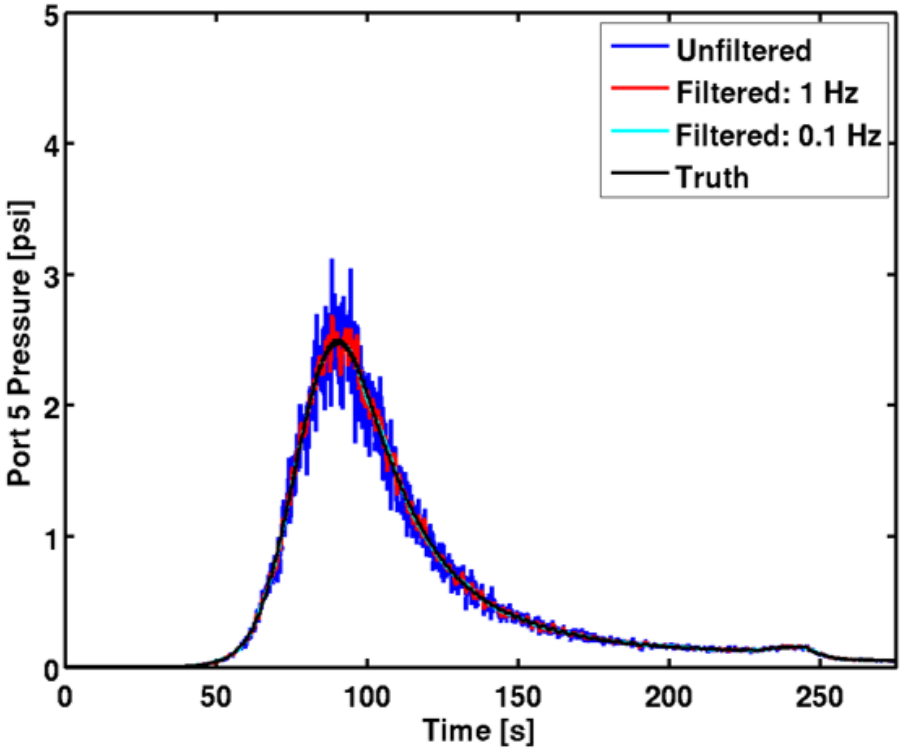

Figure 4.11: Port 5 Pressure: 5% Full Scale Noise at Maximum Dynamic Pressure

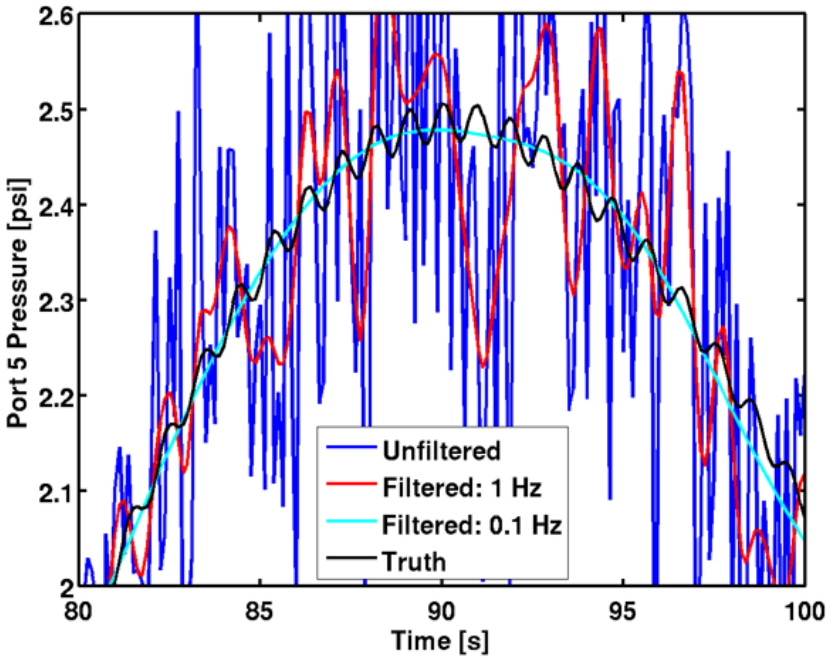

Figure 4.12: Port 5 Pressure: 5% Full Scale Noise at Maximum Dynamic Pressure (Detail)

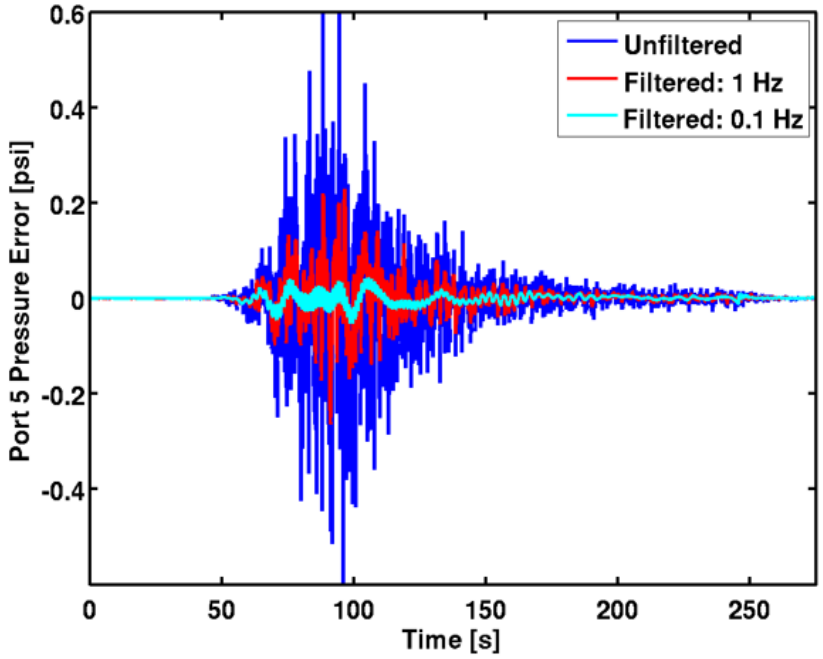

Figure 4.13: Pressure Error Due to Filtering

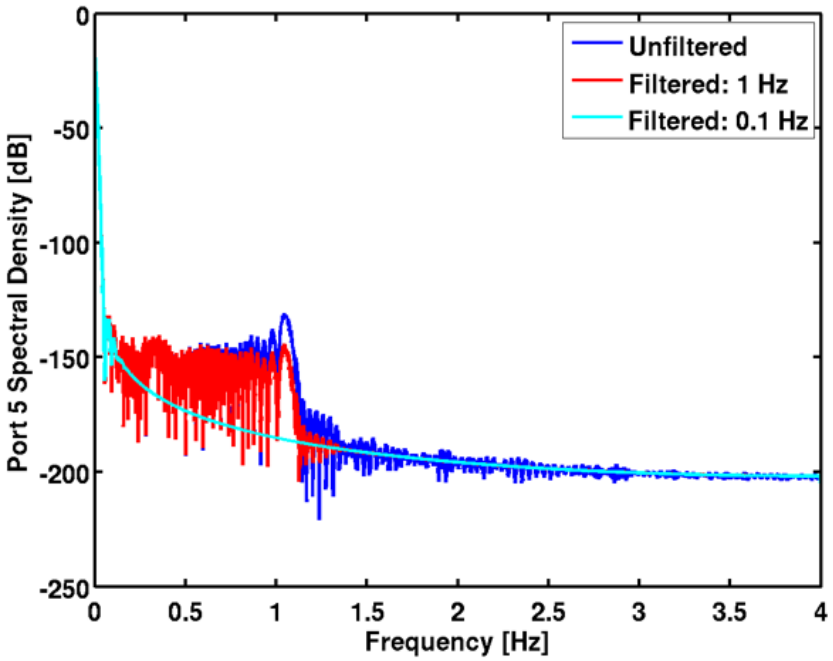

Figure 4.14: Port 5 Power Spectral Density: No Noise

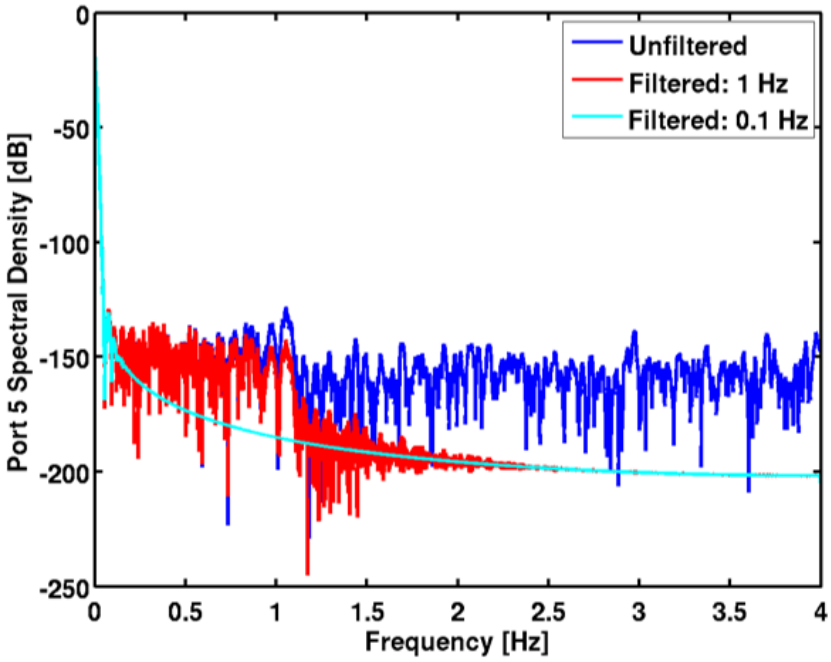

Figure 4.15: Port 5 Power Spectral Density: 0.5% Noise

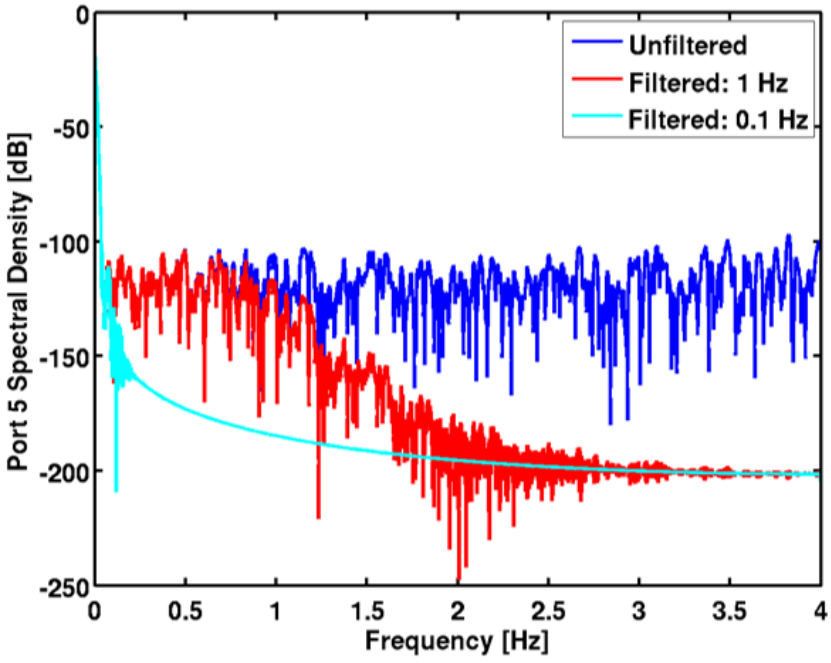

Figure 4.16: Port 5 Power Spectral Density: 5% Noise

4.1.6 Pneumatic Lag

The MEADS system response model, or lag model, captures the dynamics of the pressure measurement from the surface port location to the pressure transducer (the sensor). In general, these characteristics are a function of the line properties (tube diameter and length), fluid properties (density, dynamic viscosity, etc.), as well as flight conditions (pressure and temperature at the port and temperature at the transducer). The system response models are used to accomplish two objectives: firstly, to accurately model the response so that pre-flight simulation can be used to assess hardware, algorithms, and telemetry rates, and secondly, to characterize the system response so that measured pressures can be corrected to actual surface pressures for use in generating atmospheric data estimates.

High–fidelity response models based on the Navier–Stokes equations are available in the literature, in particular the infinite–order frequency–domain Bergh–Tijdeman response model [30] and variations on this model for branched systems developed by Whitmore [31]. In these models, the pneumatic system is broken up into a series of segments, each with constant line and fluid properties. The end to end frequency response from port to transducer becomes the product of the individual response functions for each segment. Entrapped volume in any of the segments can also be captured. In this manner changes in tubing diameter as well as temperature gradients can be explicitly modeled. The response is evaluated across a range of input frequencies and the result is a complex frequency response that can be represented as magnitude and phase.

The frequency domain results for each flight condition are not readily suited either for time domain simulation or for direct analysis of time histories of measured pressure. For these purposes, a low–order response model must be utilized. For simple 2nd order systems, this response can be characterized by a natural frequency and damping, with transfer functions of the form

$$\frac{P_L}{P_0} = \frac{\omega_n^2}{s^2 + 2\zeta\omega_n + \omega_n^2} \tag{4.7}$$

where P_0 is the applied pressure, P_L is the lagged pressure, and ζ and ω_n are the damping ratio and natural frequency, respectively, and s is the Laplace variable.

A variety of 2nd order models based on simplified fluid mechanics relations are available in the literature with varying assumptions and classifications [32]. A new 2nd order response model based on first principles is presented in [32]. This model is derived directly from the Bergh–Tijdeman equations using order reduction techniques and was found to be more accurate than other 2nd order models. The natural frequency and damping coefficients of this model are

$$\omega_n^2 = \frac{A_c a_s^2 / Lv}{(LA_c/2v)\left[1 + (1/12)\left(\gamma L R_d\right)^2 / \left(a_s\rho_0\right)^2\right] + 1 + (1/6)\left(\gamma L R_d\right)^2 / \left(a_s\rho_0\right)^2} \tag{4.8}$$

$$\zeta = \frac{\omega_n}{2}\left(\frac{\gamma R_d}{\rho_0}\right)\left[\frac{vL}{A_c a_s^2} + \frac{1}{2}\left(\frac{L}{a_s}\right)^2\right] \tag{4.9}$$

where L is the tube length, A_c is the cross-sectional area, v is the transducer entrapped volume, ρ_0 is the fluid density in the tube, c is the speed of sound, and γ is the ratio of specific heats. The parameter R_d is known as the acoustic impedance and can be calculated as a function of Reynolds number to capture laminar, transitional, or turbulent flow conditions, as described in [32].

Another approach to time domain analysis is look for a low-order system that matches the model response. This assumed form of this equivalent system is chosen to capture the modeled dynamics and to facilitate efficient simulation. Numerical optimization techniques have been utilized to fit transfer function models to the high-fidelity frequency response model, including up to 4th order

systems with pure time delay. These results were not found to significantly improve the 2nd order model and thus were not used to model lags for MEADS error analysis.

Due to computational complexities of simulating the tube and transducer response, these models were employed in a stand–alone manner in order to assess impacts to system performance. These studies include both the high–fidelity frequency domain models suitable for analyzing specific flight conditions as well as 2nd–order approximate models suitable for analyzing time histories.

The first study is an assessment of the port diameter of 0.1 in. Three flight conditions were explored using the high–fidelity frequency response model, including a high Mach/low pressure case, the maximum pressure case, and a low Mach/low pressure case. The frequency response for these three conditions are shown in Fig. 4.17 and 4.18. The frequency response of the 2nd order model is also shown for comparison. Table 4.3 shows several important metrics of the frequency response for these three flight conditions. Here, the time constant and the time delay (computed from phase loss at 1 Hz frequency) are shown corresponding to the high–fidelity (HF) model as well as the 2nd order model. While differences are apparent between the HF and 2nd order models, the trends and orders of magnitude are similar. These results agree to within a factor of 2 or better with an independent implementation using a reduced–order Bergh–Tijdeman model described in [33]. These results indicate that the response time is acceptable even for the worst–case lag time at the low Mach, low pressure condition.

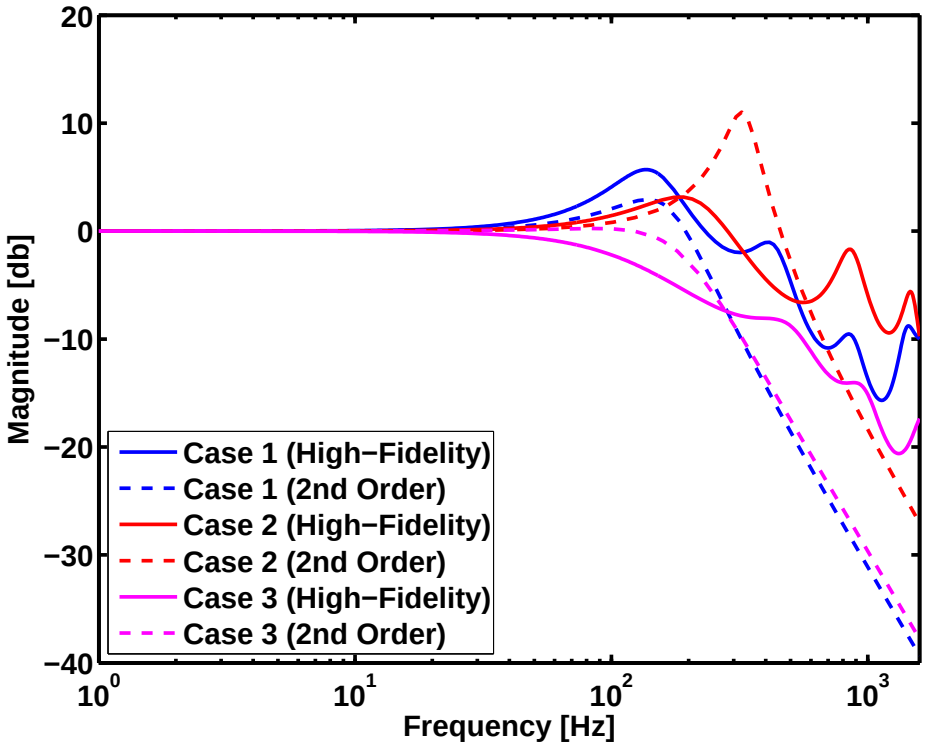

Figure 4.17: Tube Response: Magnitude

A time history of the pressure difference computed using the 2nd order model is shown in Fig. 4.19. If the input signal is of sufficiently low frequency content, then these lag effects are completely deterministic in nature and can effectively be corrected for by inverting the transfer function to solve for the pressure signal at the port. Assuming no model uncertainties, then the lag effects can be corrected without error. However, errors can arise due to the presence of tube

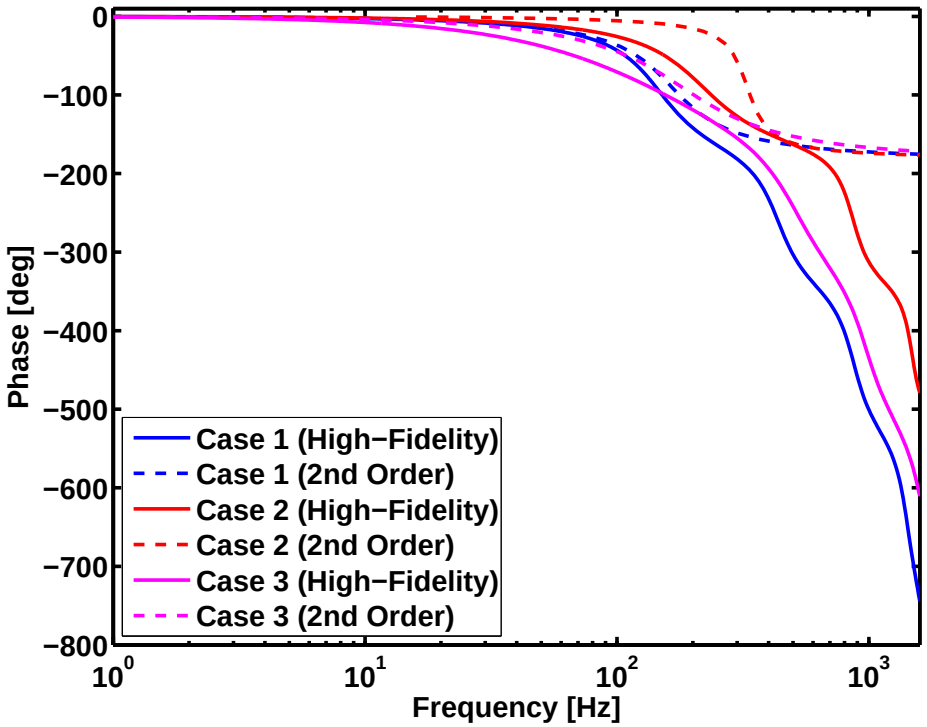

Figure 4.18: Tube Response: Phase

Table 4.3: Response Model Conditions and Results

Condition	M_∞	q_∞, Pa	P, Pa	τ, sec (HF)	τ, sec (2nd)	Δt, sec (HF)	Δt, sec (2nd)
1 (High Mach)	29.0	850.0	1630.0	$0.34{\cdot}10^{-3}$	$0.72{\cdot}10^{-3}$	$0.70{\cdot}10^{-3}$	$0.75{\cdot}10^{-3}$
2 (Max q_∞)	16.8	14015.3	26788.5	$0.45{\cdot}10^{-3}$	$0.33{\cdot}10^{-3}$	$0.55{\cdot}10^{-3}$	$0.14{\cdot}10^{-3}$
3 (Low Mach)	3.1	850.0	1595.7	$1.31{\cdot}10^{-3}$	$0.78{\cdot}10^{-3}$	$2.01{\cdot}10^{-3}$	$1.09{\cdot}10^{-3}$

geometry uncertainties. Therefore it is of interest to understand the sensitivities to diameter and length uncertainties.

Table 4.4: Response Model Port Diameter Results

Port Diameter, in	τ, sec (HF)	τ, sec (2nd)	Δt, sec (HF)	Δt, sec (2nd)
0.07	$6.13{\cdot}10^{-3}$	$0.86{\cdot}10^{-3}$	$6.61{\cdot}10^{-3}$	$1.21{\cdot}10^{-3}$
0.04	$5.69{\cdot}10^{-2}$	$0.96{\cdot}10^{-3}$	$5.49{\cdot}10^{-2}$	$1.36{\cdot}10^{-3}$
0.02	2.62	$1.04{\cdot}10^{-3}$	0.22	$1.47{\cdot}10^{-3}$

Table 4.4 shows the results of a study varying the port diameter for the worst–case flight condition (low pressure, low Mach) discussed above. Here, the port diameter is varied to as low as 0.02 in. These results indicate that the 0.07 in case may be acceptable but the 0.04 in case and below quickly become unacceptable. Figures 4.20 and 4.21 show the frequency response of the high-fidelity and 2nd-order models for these port diameters. Discrepancies between the HF and 2nd

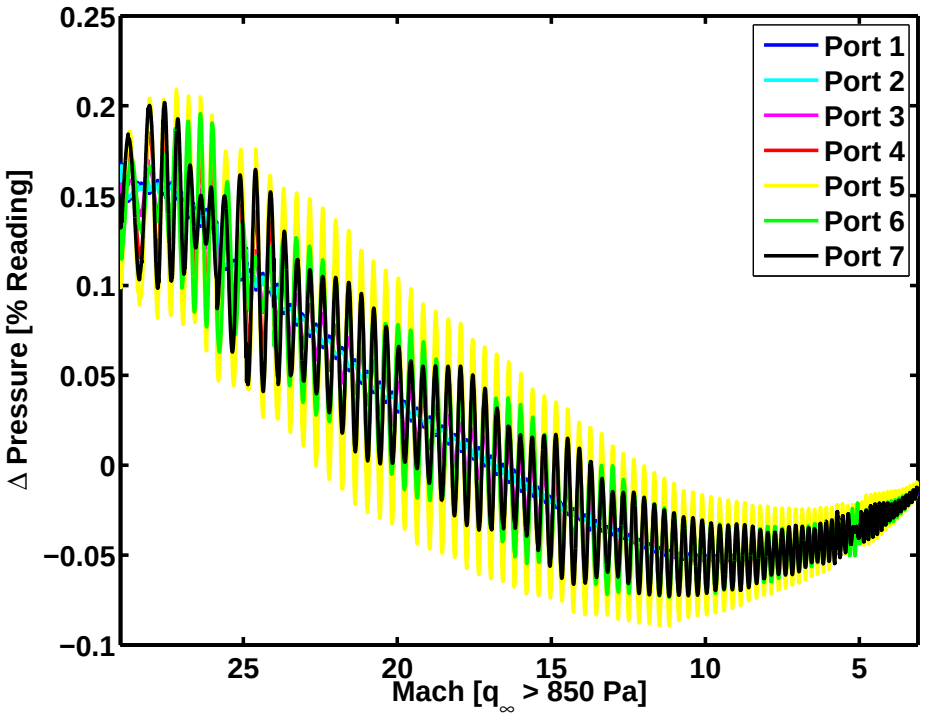

Figure 4.19: Nominal Pressure Lab

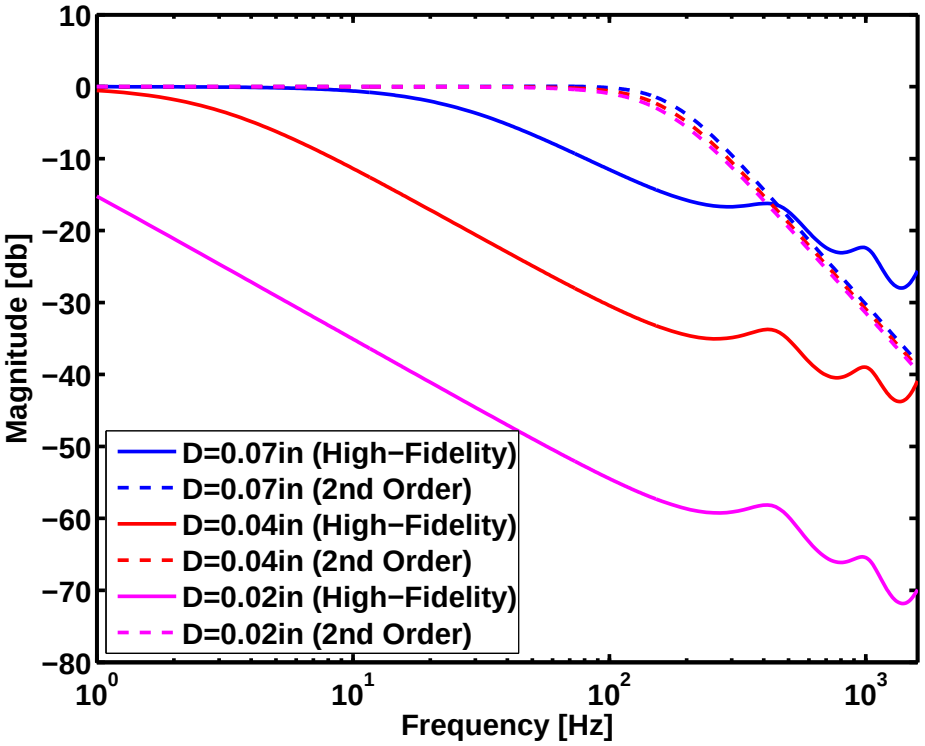

Figure 4.20: Diameter Sensitivity: Magnitude

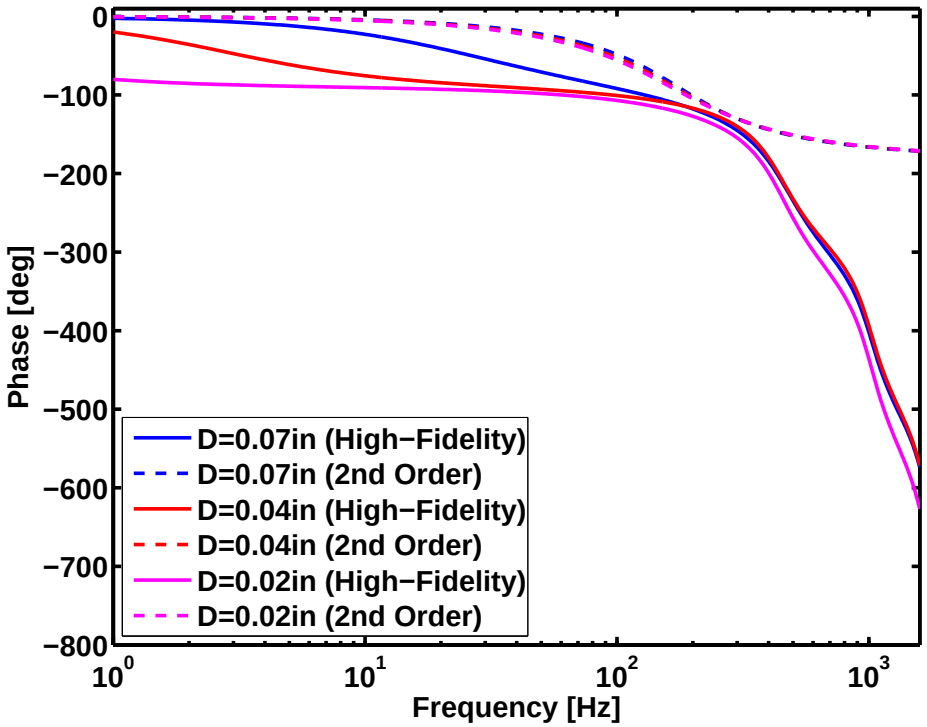

Figure 4.21: Diameter Sensitivity: Phase

order models tend to increase with decreasing port diameter. Arc jet tests conducted for various port diameters indicate that the 0.10 in case is acceptable, therefore the diameter has been kept as originally designed. However, these results serve to indicate the sensitivity to the port diameter, therefore the diameter uncertainties should be kept as small as possible. The port 5 (worst–case port) pressure lag error due to diameter uncertainty is shown in Fig. 4.22 for a range of diameter uncertainty up to 0.03 in. In all cases the lag error is small (note that the errors are shown in % of reading).

Table 4.5: Response Model Tube Length Results

Tube Length, in	τ, sec (HF)	τ, sec (2nd)	Δt, sec (HF)	Δt, sec (2nd)
+0.1	$1.22{\cdot}10^{-3}$	$0.80{\cdot}10^{-3}$	$2.03{\cdot}10^{-3}$	$1.11{\cdot}10^{-3}$
+0.25	$1.26{\cdot}10^{-3}$	$0.82{\cdot}10^{-3}$	$2.08{\cdot}10^{-3}$	$1.14{\cdot}10^{-3}$
+0.5	$1.31{\cdot}10^{-3}$	$0.84{\cdot}10^{-3}$	$2.15{\cdot}10^{-3}$	$1.18{\cdot}10^{-3}$

Next, a study was conducted to assess the sensitivity to tube length. Three cases were investigated using at the low pressure, low Mach flight condition. Table 4.5 summarizes the effects perturbing the total tube length by increments of 0.1 in, 0.25 in, and 0.5 in. In each case the time constant and time delay metrics do not change considerably. Figures 4.23 and 4.24 show the frequency response results for these perturbations. These results indicate that the pressure system is not highly sensitive to the tube length. Figure 4.25 shows the time history of the lag error for port 5 induced by length uncertainties of up to 0.5 in. As in the previous case, these errors are acceptably small.

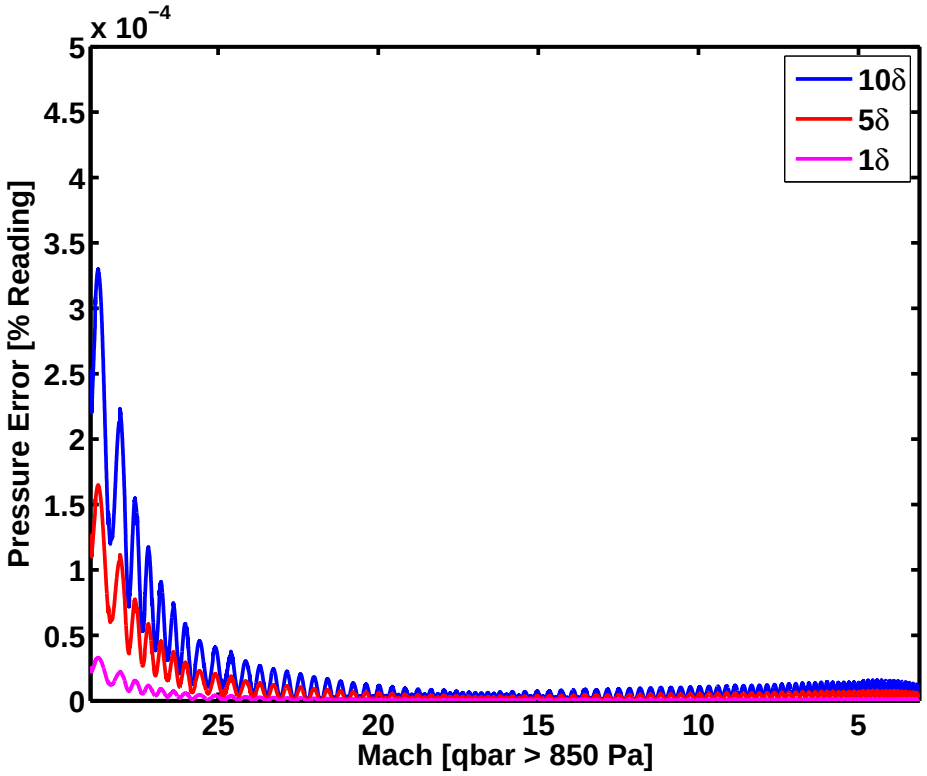

Figure 4.22: Port 5 Lag Sensitivity

Based on the system requirements of 1.41 mm length uncertainty and 0.254 mm diameter uncertainty, a worst-case lag error over the entire trajectory was determined from these sensitivity results to be 6.94e-04% of reading at each port, in a 3σ sense.

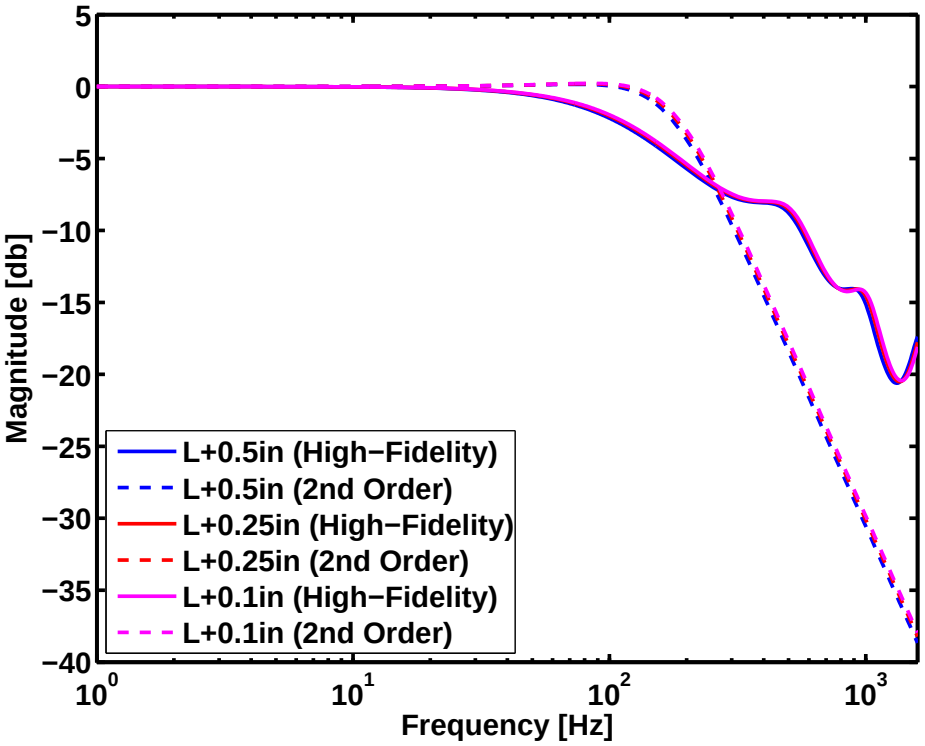

Figure 4.23: Length Sensitivity: Magnitude

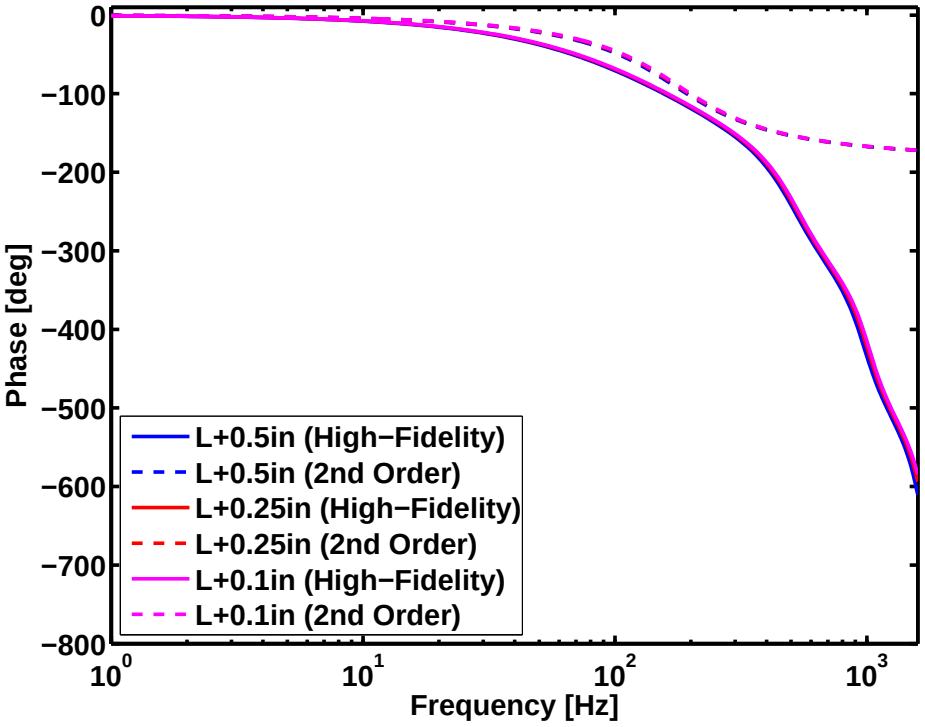

Figure 4.24: Length Sensitivity: Phase

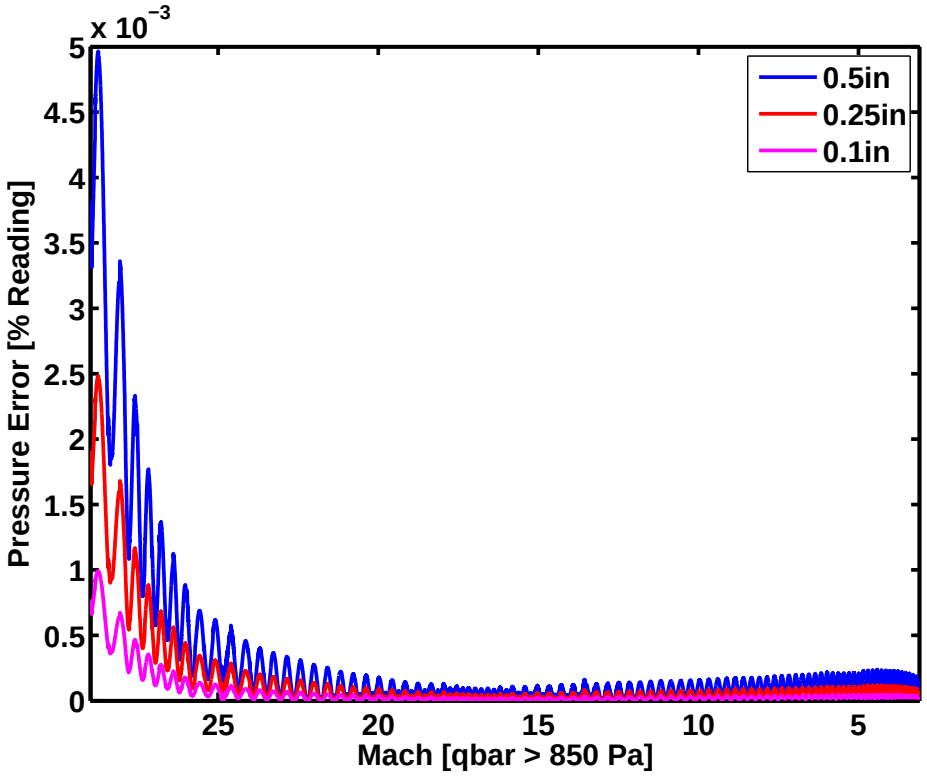

Figure 4.25: Port 5 Lag Sensitivity

4.1.7 Thermal Transpiration

Under rarefied flow conditions, transpiration induced effects within a tubing system can cause the pressure measured by the transducers to be significantly different from the surface pressure. The effects can be divided into those caused by temperature gradients between the transducer and the surface, and those caused by heat transfer and/or shear stress.

A study of the available literature yielded three models to account for transpiration effects; two models for simulating the difference between measured and orifice pressure due to thermomolecular flow effects and one model for simulating the difference between the surface and orifice pressure due to shear stress and/or heat transfer. The first transpiration model is provided in [34], which is an application of thermomolecular flow theory developed by Knudsen in [35, 36]. Knudsen's general formula for the thermomolecular pressure effect is

$$\frac{dp}{dT} = \frac{1}{\left(1 + b'r/\lambda\right)^2} \frac{P}{2T}, \quad \text{where} \quad b' = b_0 \frac{1 + b_1 r/\lambda}{1 + b_2 r/\lambda} \tag{4.10}$$

where r is a physical length scale, λ is the mean free path, P is the pressure, T is the temperature, and b_0, b_1, and b_2 are empirical constants. The empirical constants have been obtained by Knudsen, using least–squares fit to data acquired with hydrogen in glass tubes [35]. The results are $b_0 = 2.46$, $b_1 = 3.15$, and $b_2 = 24.6$.

Assuming that the temperature in the tubing between the surface and the transducer is known as a function of length x, Eq. (4.10) can be written as

$$\frac{\partial p\left(x\right)}{\partial x} = \frac{p\left(x\right)}{2T\left(x\right)} \left[\frac{\partial T\left(x\right)}{\partial x}\right] \left[\frac{\kappa\left(p,T,D\right)^2 + b_0 \kappa\left(p,T,D\right)}{\kappa\left(p,T,R\right)^2 + \left(b_0 + b_1\right)\kappa\left(p,T,D\right) + b_1 b_2}\right]^2 \tag{4.11}$$

Table 4.6: Gas Constants for Carbon Dioxide

Constant	Value
R_g, J/kg-K	191.8
μ_0, Pa-s	$14.8 \cdot 10^{-6}$
T_0, K	293.15
C, K	240.0

where the parameter κ is the Knudsen number, given by

$$\kappa = \frac{\mu}{Dp}\sqrt{\frac{\pi R_g T}{2}} \tag{4.12}$$

where R_g is the specific gas constant. The viscosity μ can be calculated as a function of temperature using Sutherland's relation [37]

$$\mu = \mu_0 \left(\frac{T_0 + C}{T + C}\right)\left(\frac{T}{T_0}\right)^{3/2} \tag{4.13}$$

The constants associated with carbon dioxide are summarized in Table 4.6.

The second transpiration model is based on an algorithm described by Potter. [38]. This model is based on the theoretical formulation of [39] and empirical data obtained in [40]. The empirical data were obtained in a sequence of experiments involving a wide range of tube lengths, diameters, orifice shapes, and gases, including hydrogen, helium, nitrogen, and argon. The model is

$$\frac{\partial p\,(x)}{\partial x} = \frac{p\,(x)}{2T\,(x)}\left[\frac{\partial T\,(x)}{\partial x}\right]\left[1 + \frac{c_0}{\kappa\,(p,T,D)} + \frac{c_1}{\kappa\,(p,T,D) + c_2/\kappa\,(p,T,D)}\right]^{-2} \tag{4.14}$$

where $c_0 = 0.275$, $c_1 = 0.625$, and $c_2 = 24.0$.

Note that both the Knudsen and Potter transpiration models predict that $(\partial p/\partial x) \to 0$ as $\kappa \to 0$.

The last model investigated for this paper is an augmentation of the Potter model [38] that includes non–equilibrium effects due to heat transfer and shear stress. This model is described in [41]. The solution relies on empirical fits to data obtained in a wide range of experiments. The algorithm for calculating non–equilibrium effects is complicated and is not repeated here.

The thermal transpiration models were employed in stand–alone codes in order to assess impacts to system performance. Figure 4.26 shows the results of an analysis comparing the thermal transpiration models along the nominal reference trajectory. Here, the pressure difference between the nominal pressure and the pressure with the thermal transpiration effects is shown for Ports 1 and 5. Results are shown for the Knudsen model, the abbreviated Potter model (i.e. without orifice effects) and the full Potter model including the orifice effects. While some difference are apparent between the Knudsen and Potter models, all show the same trend with similar magnitudes. These results indicate that above 850 Pa dynamic pressure, the thermal transpiration effects are negligible. The effects become more pronounced in the rarefied flow regime below 850 Pa dynamic pressure. For MEADS uncertainty analysis, the worst-case error due to transpiration is assumed to be 5e-4% of reading in a 3σ sense.

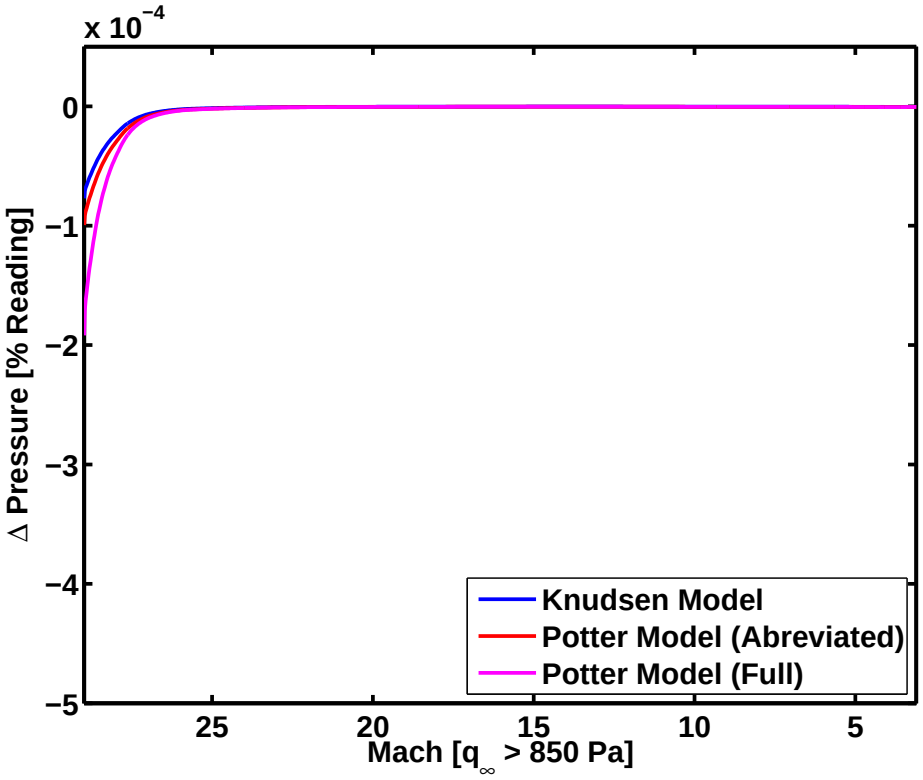

(a) Port 1 Transpiration

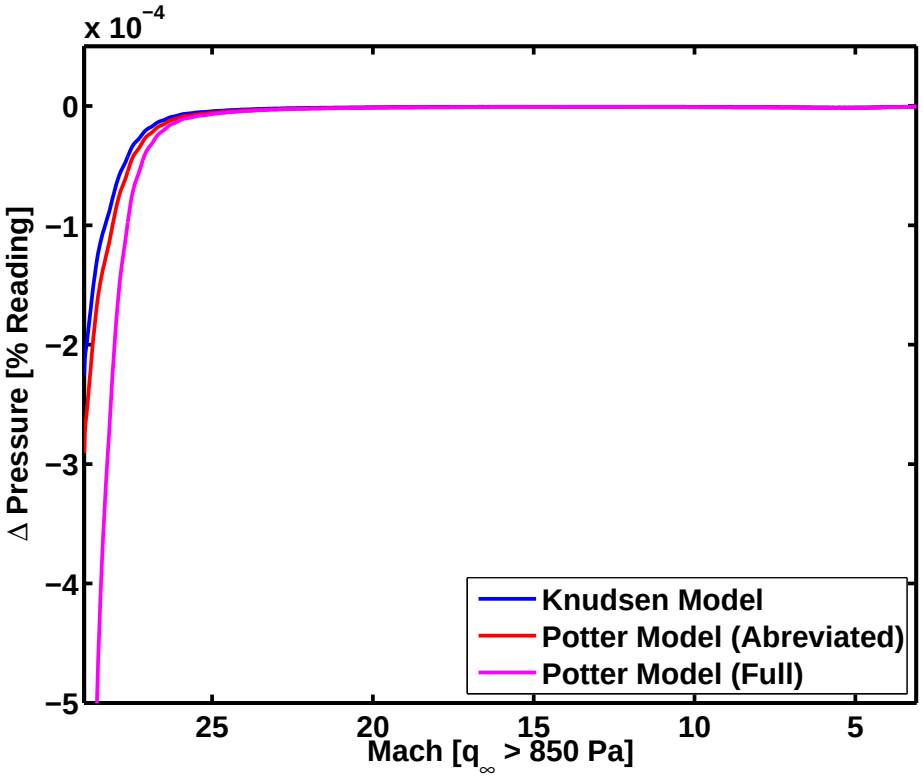

(b) Port 5 Transpiration

Figure 4.26: Thermal Transpiration Results

4.1.8 System Calibration and Temperature Uncertainties

The MEADS calibration error model is based on that described by Eq. 3.11. In summary, the error model consists of calibration parameter uncertainties, transducer and SEE thermocouple errors (noise and bias), and hysteresis and non-repeatability error estimates based on the final calibration. The final calibration and associated uncertainty models are described in Chapter 3.

4.2 CFD Pressure Distribution Uncertainties

Errors in MEADS pressure measurements due to fluid dynamic phenomena not attributable to MEADS hardware or software are estimated from computational and experimental results. Some sources of error can be estimated directly from the CFD simulations at Mars entry conditions, and include contributions from port location uncertainty, effects of grid refinement and topology, design cycle changes to the OML, ablation and deformation, tile gap filler protuberances, and orifice induced errors. These error estimates are calculated by taking the difference between nominal and off-nominal solutions, and scaling to freestream conditions where applicable, or by applying functional relationships found in the literature. Each of these factors are accounted for individually and combined using the root sum square (RSS) method, where each MEADS port is treated seperately. As MEADS pressures are expressed in dimensionless form C_p for scaling purposes, uncertainties in the pressures are expressed in normalized form $\Delta C_p/C_p$, where the numerator is the uncertainty term, and the denominator is evaluated at current conditions. The RSS expression of uncertainty terms can be written as:

$$\Delta C_p = \sqrt{\Delta C^2_{p_{location}} + \Delta C^2_{p_{OML}} + \Delta C^2_{p_{ablation}} + \Delta C^2_{p_{deformation}} + \Delta C^2_{p_{protuberance}} + \Delta C^2_{p_{orifice}}} \tag{4.15}$$

The ability of the LAURA code to yield "correct" answers was also to be estimated by comparing CFD results against those obtained from wind-tunnel experimentation, and thus used to establish confidence in the flight CFD solutions. Significant variability in wind tunnel measurements due to nonuniform test section conditions were experienced. Analysis required to make the data useful for CFD validation purposes is beyond the scope of this work.

4.2.1 Port Location Uncertainty

Laser scan metrology was performed on the MSL heatshield at the Lockheed Martin Space Systems Company in order to provide high-fidelity measurements [42] of the MEDLI/MEADS sensor locations and to help quantify the accuracy of heatshield-to-IMU alignment. The measurements indicated that the MEADS port locations are known to within approximately 1 mm, and so the uncertainty in their locations is quite small in comparison to other heatshield geometric features, e.g., discontinuities at PICA tile edges or protruding gap fillers. The effect of port location uncertainty on MEADS pressure measurement is estimated using the magnitude of pressure coefficient gradient extracted from flight CFD solutions, and is expressed at each port as

$$\Delta C_{p_{location}} = \frac{|\nabla p| \Delta s}{q} \tag{4.16}$$

The 3σ value for port location uncertainty ΔC_p is based on Δs corresponding to the metrology tolerance, or 1 millimeter, and is mapped over the entire nominal trajectory space. In order that it might be scaled to other trajectories, it is expressed in the tables normalized to the current C_p, i.e., $\Delta C_p/C_p$.

4.2.2 Grid Refinement and Topology, OML Design Cycle Changes

The discretization of grids used for computation of the MSL nominal aerodatabase would be considered rather coarse by today's standards. After design cycle changes to the OML brought about as a consequence of changes to TPS requirements, a new grid of much-improved resolution was constructed for the flight geometry and used to compute point checks for comparison against nominal aerodatabase results. The OML differences are shown in Fig. 4.27.

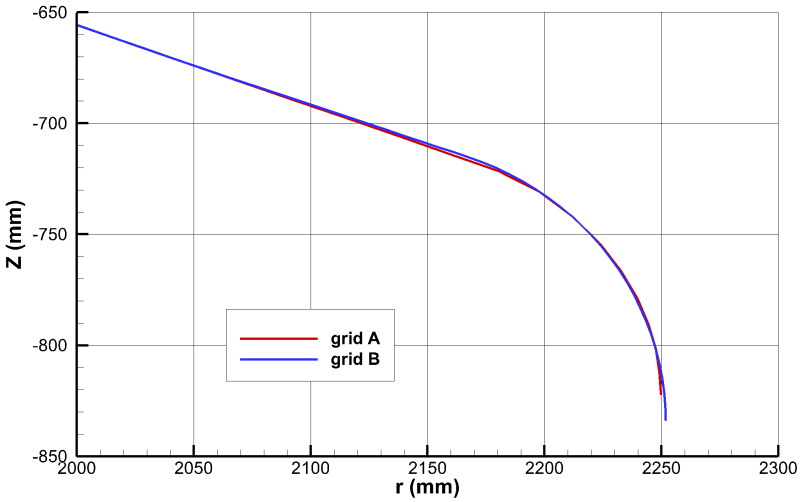

Figure 4.27: Outer Mold Lines Described by Original (Grid a) and Refined (Grid b) CFD Grids

Because the two grids describe different OMLs and are of differering resolution and topology, the effects of changing these three factors are coupled, and so are combined within one uncertainty term. It is important to note the limitations imposed by grid resolution and numerical stability as applicable to the LAURA code. On one hand, the coarse nominal aerodatabase grid is near the lower limit for acceptably resolved solutions; on the other hand, the updated fine grid is near the practical limit for computing solutions without numerical instabilities that occur with LAURA due to point clustering in body-tangent directions. In other words, solution accuracy will not improve monotonically as grid density tends to infinity. For these reasons, only the results from the original aerodatabase grid and the final OML fine grid are used to approximate the errors due to both grid effects and OML changes. The expression for the combined uncertainty term is written as

$$\Delta C_{p_{OML}} = |C_{p_{finegrid}} - C_{p_{coarsegrid}}| \tag{4.17}$$

The left hand side of Eq. (4.17 is assumed to lie at the 2σ bounds, as the data were only available for a few flow conditions. A grid sensitivity study deemed necessary to estimate to 3σ confidence is beyond the scope of this work. The right hand side of Eq. (4.17) is only known over a small portion of the trajectory space and so is implemented in a form amenable to scaling over the entire trajectory, i.e., $\Delta C_p/C_p$. The maximum value of $\Delta C_p/C_p$ is used from the available data at each port and applied over the entirety of the trajectory space.

4.2.3 Ablation and Deformation

Shape changes to the heatshield that occur due to ablation and deformation were modeled for the OML13F configuration. The ablation case was computed at the 07-25 trajectory peak heating condition, for a bounding worst-case scenario where the TPS is recessed to a maximum of approximately 20 millimeters along the symmetry plane leeside [19]. The uncertainty term due to ablation is an engineering estimate defined as the absolute difference between baseline and ablated cases, scaled to the sum of dynamic pressure and heat load, normalized to their maximum and total values, respectively

$$\Delta C_p = |C_{p_{ablated}} - C_{p_{baseline}}| \frac{1}{2} \left(\frac{q}{q_{max}} + \frac{Q}{Q_{max}} \right) \tag{4.18}$$

where Q is the instantaneous heat load and Q_{max} is the total heat load.

For analysis of heatshield deformation and its effect on aerodynamics, a finite element model subjected to 12.2 g decelerative load on the 06-05 nominal trajectory was used to modify the baseline grid, where predicted heatshield apex deflection is approximately 13 millimeters. As the current trajectory has a 3σ high deceleration of 13.4 g, a scale factor is applied to the right hand side in order to reflect the current conditions via linear extrapolation. The expression for the 3σ loading term is then based upon the difference between baseline and deflected solutions, and scaled to the ratio of instantaneous to maximum dynamic pressure. This term is written as

$$\Delta C_{p_{loading}} = 1.1 |C_{p_{deformed}} - C_{p_{baseline}}| \frac{q}{q_{max}} \tag{4.19}$$

The ablation and deformation terms are only known at their corresponding peak conditions, so are implemented over the trajectory space using the $\Delta C_p / C_p$ form as used for the OML term.

4.2.4 Gap Filler Protuberances

The effect of PICA tile gap filler protuberances at maximum heating conditions on the 0801-A trajectory were investigated for three locations on the heatshield [43], where the nose cap case was deemed most relevant to MEADS performance. Heatshield flowfields with gap filler heights of 0.1 inch, 0.2 inch, and 0.4 inch were computed at fully turbulent conditions, and curves of pressure along a surface streamline traversing the protrusion were extracted from the solutions, as shown in Fig. 4.28, where positive distance denotes downstream location.

The radius of influence of these protrusions was shown to be on the order of 0.3 meters. For conditions where the MEADS port is in close proximity to a gap filler protrusion, the corresponding magnitude of error ΔC_p is as large as 0.4 and dwarfs the sum of all other uncertainty terms considered here. In addition, the protrusion radius of influence and magnitude of error would increase if the flow were modeled as laminar. Uncertainty is inferred from the turbulent results and scaled in the same way as the ablation term, where the expression is written as

$$\Delta C_{p_{gapfiller}} = |C_{p_{gapfiller}} - C_{p_{baseline}}| \frac{1}{2} \left(\frac{q}{q_{max}} + \frac{Q}{Q_{max}} \right) \tag{4.20}$$

While a gap filler protuberance term would dominate the uncertainty model, the likelihood of its occurrence was considered low, and so the term was omitted from the model. If gap filler protuberances did occur, they would likely be identifiable in the pressure data as large excursions from the nominal model.

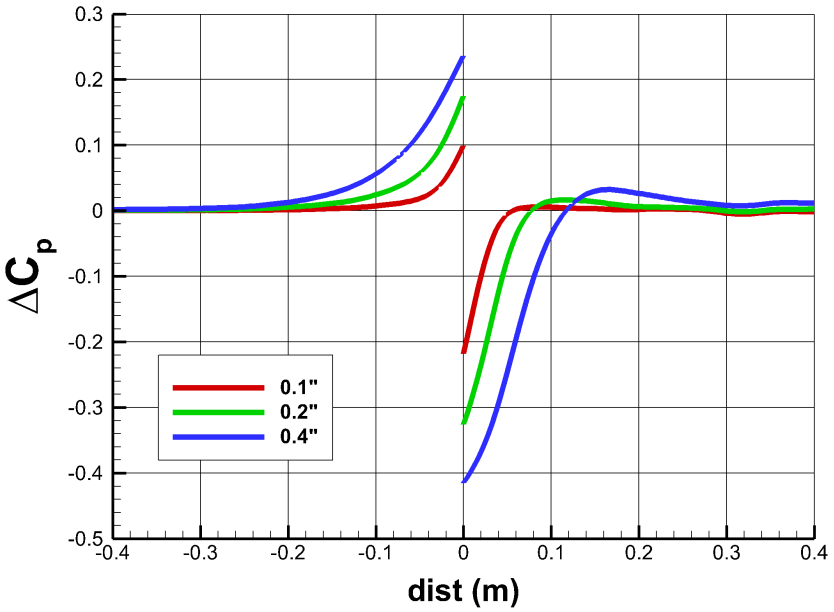

Figure 4.28: Pressure Coefficient Disturbance vs. Relative Distance from a Step Discontinuity on Nose Cap. Flow is From Left to Right.

4.2.5 Orifice Induced Errors

The presence of a pressure orifice in a flowfield can cause errors in surface pressure measurements, where the errors are a function of the orifice diameter, shear stress at the wall, and the working fluid density and viscosity [45]. This relationship may be expressed as

$$\frac{e}{\tau_w} = f\left(d^+\right) \tag{4.21}$$

where e is the pressure error and d^+ is the orifice Reynold's number, $u_\tau d/v$.

The plot of this relationship, shown in Fig. 4.29(a), shows that the left hand side becomes quite small (on order of 0.1) when d^+ is less than 100 [45]. Using the TPS stressing trajectories for reference conditions, the orifice Reynolds number at MEADS port locations never exceeds approximately 70, and so the corresponding pressure error never exceeds approximately 5 Pa. A plot of orifice Reynolds number is shown for the peak dynamic pressure along the most stressful trajectory in Fig. 4.29(b). In $\Delta C_p/C_p$ form, the peak magnitude of this error is of order 1.E-4, and is vanishingly small for all but the lateral ports at conditions at or near peak dynamic pressure. For this reason, and as the curves describing this error relationship are not well established at such low values of orifice Reynolds number and wall shear stress, the term is omitted from the current model.

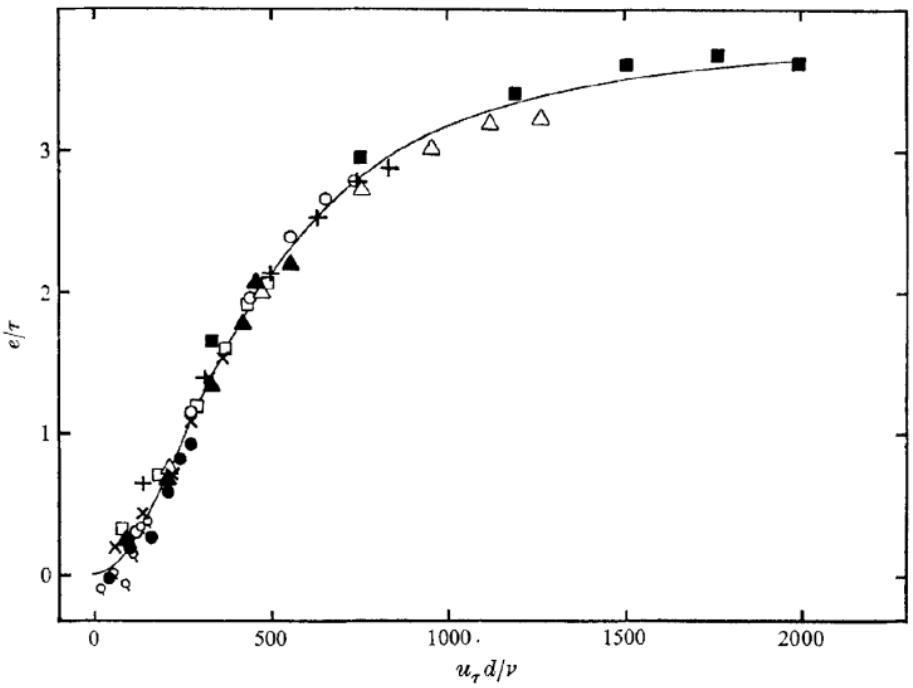

(a) Orifice Induced Error Curve

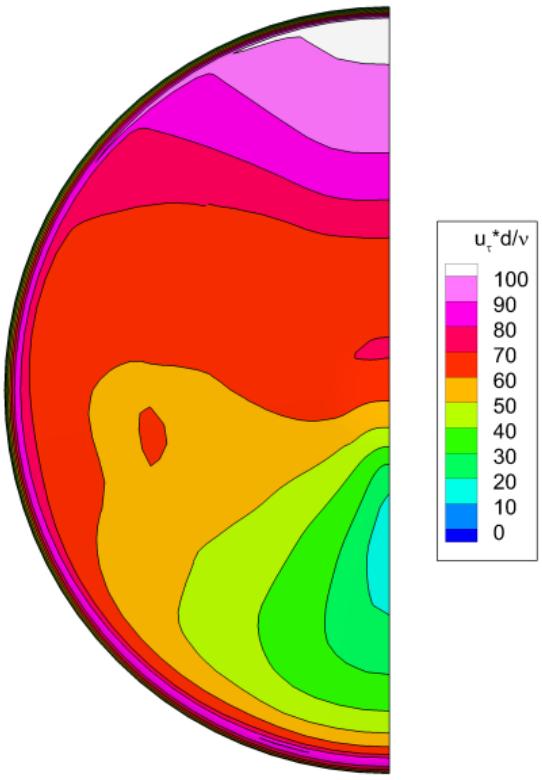

(b) d^+ at Peak Conditions

Figure 4.29: Orifice Effects

4.2.6 Uncertainty Term Implementation

Table 4.7 gives 3σ values for the error terms that are implemented in $\Delta C_p/C_p$ form. To obtain the scaled uncertainty ΔC_p for each, they are multiplied by the base C_p, which is interpolated from the lookup tables for the current flight condition. The terms may then be summed as in equation 4.15.

Table 4.7: 3σ ΔC_p Values for Uncertainty Terms Scaled Over the Trajectory Space

	Port 1	Port 2	Port 3	Port 4	Port 5	Port 6	Port 7
OML + grid	4.711e-03	5.418e-03	3.824e-03	4.080e-3	1.264e-02	4.969e-03	4.969e-03
Ablation	1.000e-03	1.221e-03	1.807e-03	3.469e-02	2.057e-03	7.671e-03	7.671e-03
Deformation	8.400e-04	3.698e-04	3.798e-03	1.223e-02	2.296e-02	1.098e-02	1.098e-02

4.3 Error Analysis Results and Sensitivity Studies

This section describes the total system performance results for both the flight and flight spare transducer sets. Monte Carlo analysis is utilized with the basic pressure-only MEADS algorithm to determine the angle of attack, sideslip, dynamic pressure, and Mach number estimation performance. Monte Carlo analysis described in this section is based on the 09-HOL-01 nominal trajectory.

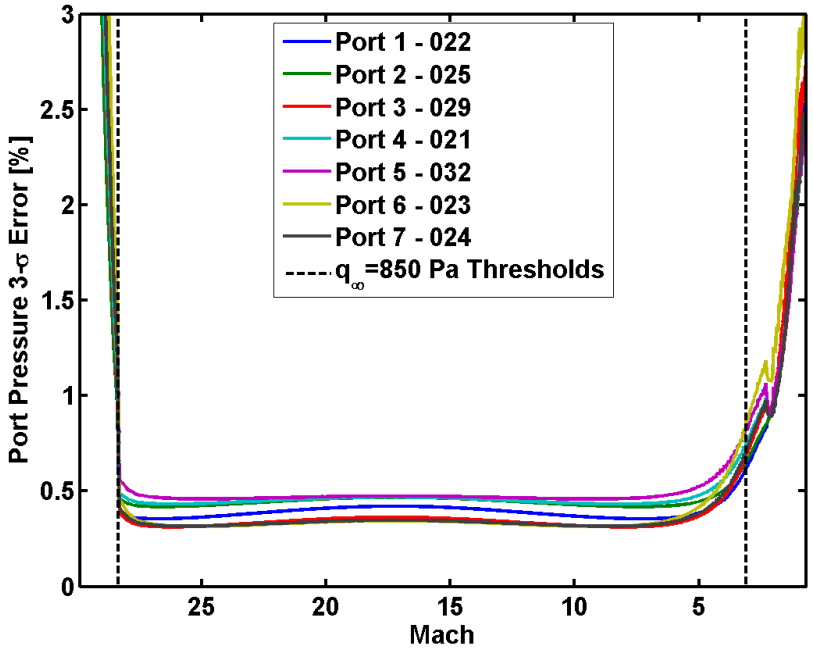

Figure 4.30: Pressure Measurement Errors Along Trajectory

The total uncertainties for the MEADS flight system evaluated along the nominal trajectory are shown in Figure 4.30. The values of the error model parameters are listed in Table 4.8. Note that the error parameters are assumed to be Gaussian except where otherwise noted.

Table 4.8: Error Parameters

Parameter Name	Value
Mensor Accuracy (σ_c) (Ref. 47)	0.001 psi
Transducer Thermocouple Bias (σ_{b_1})	2.5 deg C (uniformly distributed)
SSE Thermocouple Bias (σ_{b_2})	1.5 deg C (uniformly distributed)
Thermocouple Noise ($\sigma_{n_1} = \sigma_{n_2}$)	0.05 deg C
SSE Pressure Channel Noise (σ_V)	10 counts
A/D bit size	14
Time Stamp Error	25 μs (uniformly distributed)
Port Location Uncertainties	0.04 in (uniformly distributed)
Maximum Leak Rate	0.047022% (uniformly distributed)
Pressure Path Length Uncertainty (Ref. 48)	1.41 mm
Pressure Path Diameter Uncertainty (Ref. 48)	0.254 mm

The results of the Monte Carlo analysis are shown in the following figures. Figure 4.31 shows the total system error for the angle of attack estimate, Figure 4.32 shows the total system error for the angle of sideslip estimate, and Figure 4.33 shows the total system error for the dynamic pressure estimate. In these figures, the errors are shown only for the portion over which the MEADS hardware requirements pertain. Specifically the total hardware and total CFD errors are shown (cyan and red curves, respectively) along with the total combined error (blue).for dynamic pressures greater than 1750 Pa for angle of attack errors, greater than 1250 for sideslip errors, and greater than 850 Pa for dynamic pressure errors. These plots indicate that the MEADS hardware meets requirements over the entire dynamic pressure range range.

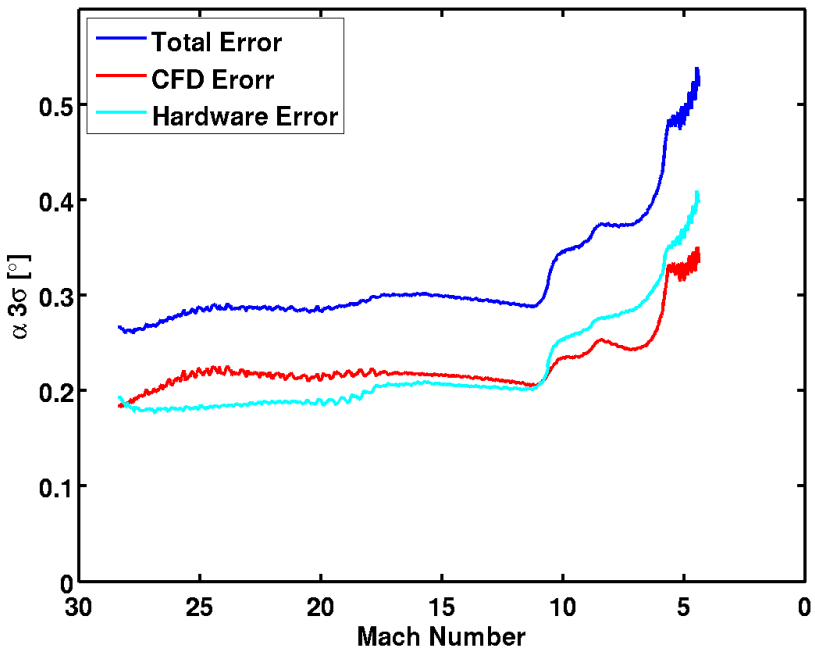

Figure 4.31: Total Estimation Error: Angle of Attack

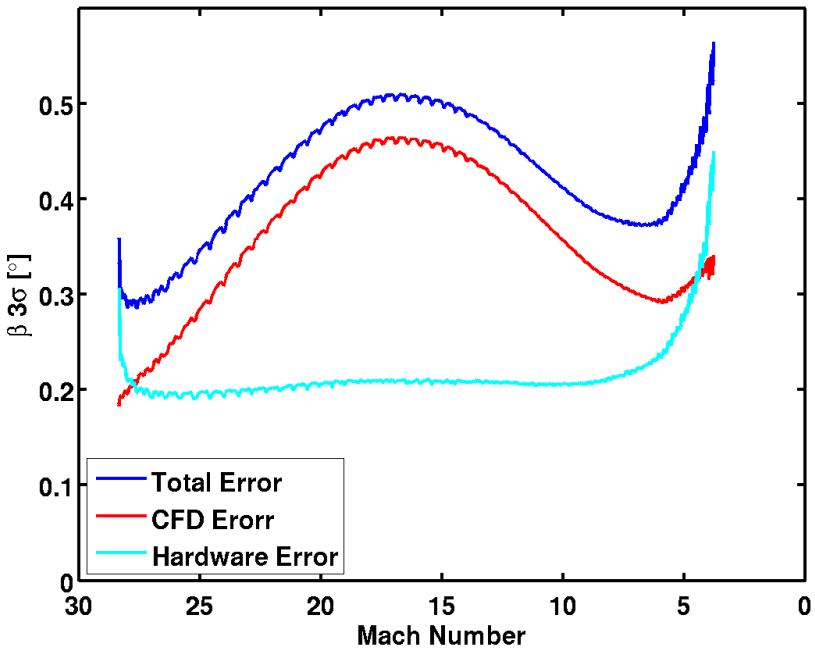

Figure 4.32: Total Estimation Error: Angle of Sideslip

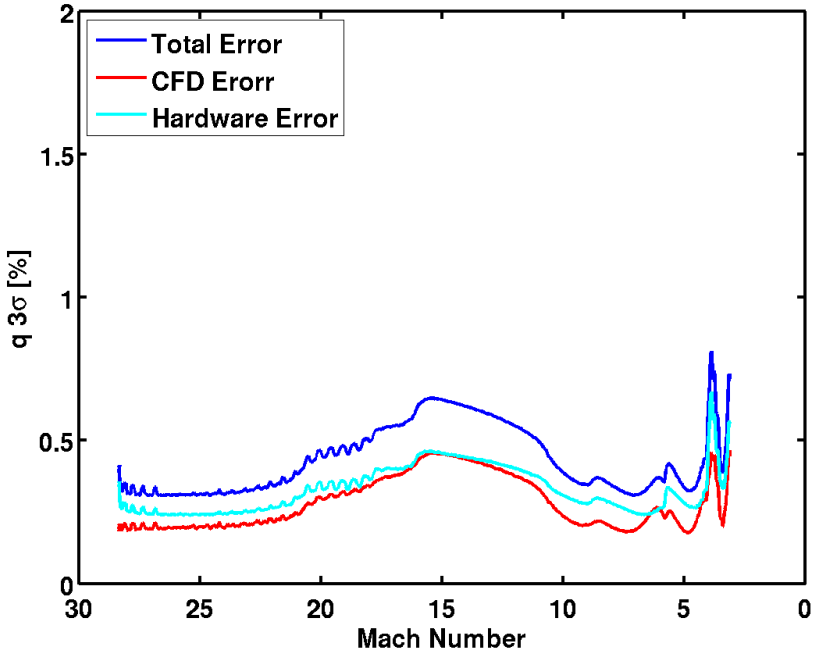

Figure 4.33: Total Estimation Error: Dynamic Pressure

Plots of individual error sources are given in Appendix B. Here, the trajectory average errors for the uncertainties are tabulated in Table 4.9. These uncertainties indicate that, on average, the MEADS system achieves angle of attack and sideslip estimation errors less than 0.5 degrees

and dynamic pressure estimation errors less than 1%. The largest contributors of errors are the transducer performance and the OML/grid CFD errors.

Table 4.9: Trajectory Average Errors (3σ)

Error Model Parameter		Angle of Attack (deg)	Angle of Sideslip (deg)	Dynamic Pressure (%)
Transducer Errors	Calibration Error	0.1982	0.1364	0.2377
	Temperature Uncertainty	0.0788	0.1060	0.1217
SSE Errors	Quantization	0.1205e-11	0.0015e-11	0.7133e-11
	Noise	0.0488	0.0730	0.0971
	Temperature Uncertainty	0.0096	0.0082	0.0170
Geometry Error	Port Location	0.0387	0.0301	0.0268
	Pressure Leak	0.0960	0.1055	0.1228
	Lag Uncertainty	9.4486e-4	1.0377e-3	1.2138e-3
	Thermal Transpiration	6.8808e-4	0.7477e-3	0.8749e-3
Latencies	Time Tag Error	0.1380e-3	0.1233e-3	0.1560e-3
Mechanical	Vibration	0.0823	0.0966	0.0977
CFD	OML/grid	0.1966	0.2088	0.2376
	Ablation	0.0426	0.1293	0.0400
	Deformation	0.1294	0.1879	0.0941
Total Hardware System Error		0.2558	0.2391	0.3262
Total CFD Error		0.2392	0.3092	0.2586
Total (Combined) Error		0.3503	0.3909	1.3785

Chapter 5

Conclusions

This document describes the as-built MEADS error budgets for the angle of attack, angle of sideslip, and dynamic pressure reconstruction based on pressure measurements. The error models include hardware, calibration, vibration, and CFD pressure distribution uncertainties. The MEADS nominal pressure model and its corresponding CFD-based uncertainty model are presented, where uncertainty terms due to OML changes, grid induced error, and flight ablation and deformation effects are approximated using nominal aerodatabase and off-nominal CFD results. It is currently recommended that TPS tile gap filler protuberance effects be omitted from the uncertainty model, as their likelihood and magnitude are not understood. Uncertainties due to orifice induced error are shown to be inconsequential for MEADS at flight conditions. CFD validation and uncertainty models based on wind tunnel data are absent from the present work, as the variability of wind tunnel conditions make such models impractical to implement. Nevertheless, some improvements to the current uncertainty models can be suggested. These would include recomputation of the MSL nominal aerodatabase on the 12-GAL-01 trajectory, using the fine OML-13F grid and full Navier-Stokes equations. Ablation and deformation effect approximations can also be improved in this way. Additional uncertainty terms for code-to-code comparisons relevant to the MSL aerodatabase can also be made using different versions of LAURA, as at least two major versions have been released since the MSL nominal aerodatabase was computed.

Applying Monte Carlo simulation techniques to the MEADS system model shows that the as-built hardware will meet Level 2 requirements over the MSL entry trajectory.The preflight modeling efforts described herein were validated via post-flight data processing and trajectory reconstruction efforts performed after MSL's landing on Mars on August 6th, 2012. The MEDLI flight data and associated reconstruction activities are described in [49–52].

Appendix A

Data Reduction Look-Up Tables

This appendix contains the two-dimensional lookup tables that can be used to convert transducer Voltage outputs into pressures (in units of psi), given the transducer and SSE temperatures. First, the coefficients a_0, a_1, and a_2 are evaluated as a function of temperatures T_1 (Transducer) and T_2 (SSE), and pressure is calculated from the equation $p = a_0 + a_1 V + a_2 V^2$ where V is the Voltage in units on mV. Similarly, the uncertainties in each polynomial coefficient can be interpolated to compute a pressure uncertainty due to calibration uncertainties.

Table A1: Transducer 020 Data Reduction Table

Transducer Temperature [deg C]	SSE Temperature [deg C]	Coefficient a_0 [psi]	Coefficient a_1 [psi/mV]	Coefficient a_2 [psi/mV^2]	Coefficient a_0 Variance [psi^2/σ_c^2]	Coefficient a_1 Variance [psi^2/σ_c^2/mV^2]	Coefficient a_2 Variance [psi^2/σ_c^2/mV^4]
-81.623077	62.115385	0.381954	0.512895	-9.70682e-05	0.155788	0.0600171	0.000772839
-82.984615	31.553846	0.383447	0.513835	-0.000135577	0.15552	0.0601329	0.000777026
-85.161538	5.361539	0.397987	0.513986	-0.000160372	0.152872	0.0593961	0.000776578
-85.707692	-13.030769	0.386094	0.513717	-0.000150185	0.155021	0.0599515	0.000775596
-86.207692	-21.438462	0.386489	0.513746	-0.000142894	0.154947	0.059958	0.000776263
-56.107692	6.050000	0.34376	0.510303	-0.000144974	0.163525	0.0612609	0.000755033
-104.496154	5.496154	0.446123	0.51662	-0.000175457	0.144583	0.0575916	0.000792075
-129.092308	4.307692	0.493424	0.520216	-0.00022702	0.137547	0.0560506	0.000812812
-56.107692	62.115385	0.327923	0.509225	-8.24387e-05	0.166405	0.0618743	0.000751339
-56.107692	31.553846	0.329602	0.510156	-0.000120832	0.166102	0.0619783	0.000755468
-56.107692	-13.030769	0.331422	0.510023	-0.000134406	0.165753	0.061837	0.000754014
-56.107692	-21.438462	0.331968	0.510057	-0.000127047	0.165652	0.0618372	0.000754709
-104.496154	62.115385	0.430129	0.515532	-0.000112304	0.147492	0.058211	0.000788346
-104.496154	31.553846	0.431658	0.51647	-0.000150791	0.147216	0.0583246	0.000792521
-104.496154	-13.030769	0.434144	0.516348	-0.000165196	0.146747	0.058151	0.000791086
-104.496154	-21.438462	0.434568	0.516379	-0.000157892	0.146667	0.0581563	0.000791759
-129.092308	62.115385	0.477094	0.519105	-0.000162541	0.140517	0.0566831	0.000809004
-129.092308	31.553846	0.478299	0.520059	-0.000201228	0.140301	0.056817	0.000813278
-129.092308	-13.030769	0.482213	0.519962	-0.000217417	0.139573	0.0565741	0.000811887
-129.092308	-21.438462	0.482379	0.519986	-0.000210229	0.13954	0.0565904	0.00081251

Table A2: Transducer 021 Data Reduction Table

Transducer Temperature [deg C]	SSE Temperature [deg C]	Coefficient a_0 [psi]	Coefficient a_1 [psi/mV]	Coefficient a_2 [psi/mV^2]	Coefficient a_0 Variance [psi^2/σ_c^2]	Coefficient a_1 Variance [psi^2/σ_c^2/mV^2]	Coefficient a_2 Variance [psi^2/σ_c^2/mV^4]
-82.700000	65.669231	0.187651	0.515953	-0.000286949	0.203231	0.0706643	0.000781292
-82.900000	37.046154	0.187889	0.516344	-0.000296872	0.203159	0.0707406	0.000783181
-83.915385	9.982051	0.220056	0.516448	-0.000328003	0.194283	0.0689952	0.000782594
-84.538462	-10.969231	0.192023	0.516124	-0.000291466	0.201944	0.0704949	0.00078251
-84.484615	-19.853846	0.195609	0.515771	-0.000267428	0.200899	0.0702739	0.000781927
-57.015384	5.673077	0.309001	0.512933	-0.000367269	0.171394	0.0633746	0.000760323
-103.996154	5.823077	0.191348	0.519347	-0.000326041	0.202305	0.0713349	0.000800295
-126.130769	5.884615	0.135011	0.521766	-0.000255454	0.219917	0.0753016	0.000818621
-57.015384	65.669231	0.274089	0.5124	-0.000323038	0.181034	0.0651729	0.000758919
-57.015384	37.046154	0.271713	0.512813	-0.000331182	0.181683	0.0653979	0.000761003
-57.015384	-10.969231	0.286734	0.512676	-0.000338246	0.17748	0.0645659	0.000760256
-57.015384	-19.853846	0.288085	0.512354	-0.000315442	0.177054	0.0644687	0.000759752
-103.996154	65.669231	0.156524	0.518814	-0.000281921	0.211921	0.0731287	0.000798895
-103.996154	37.046154	0.154238	0.519227	-0.000290126	0.212545	0.0733485	0.000800972
-103.996154	-10.969231	0.16888	0.519087	-0.000296756	0.208446	0.0725369	0.000800227
-103.996154	-19.853846	0.170309	0.518764	-0.000273909	0.207999	0.0724353	0.000799721
-126.130769	65.669231	0.100222	0.521234	-0.000211379	0.229523	0.0770936	0.000817223
-126.130769	37.046154	0.0979738	0.521647	-0.00021961	0.230136	0.0773113	0.000819297
-126.130769	-10.969231	0.112461	0.521505	-0.000226062	0.22608	0.0765081	0.000818553
-126.130769	-19.853846	0.113921	0.521182	-0.000203197	0.225624	0.0764047	0.000818045

Table A3: Transducer 022 Data Reduction Table

Transducer Temperature [deg C]	SSE Temperature [deg C]	Coefficient a_0 [psi]	Coefficient a_1 [psi/mV]	Coefficient a_2 [psi/mV^2]	Coefficient a_0 Variance [psi^2/σ_c^2]	Coefficient a_1 Variance [psi^2/σ_c^2/mV^2]	Coefficient a_2 Variance [psi^2/σ_c^2/mV^4]
-81.423077	65.669231	0.112386	0.518522	-0.000501513	0.227443	0.0749766	0.000783464
-81.638462	37.046154	0.113049	0.518706	-0.000506702	0.22722	0.0749912	0.000784429
-82.869230	9.982051	0.157146	0.518431	-0.000503696	0.213534	0.0725437	0.000783847
-83.315385	-10.969231	0.117267	0.518528	-0.000505922	0.225783	0.0747268	0.000783672
-83.507692	-19.853846	0.12063	0.51819	-0.000480845	0.224571	0.0744244	0.00078216
-55.661538	5.673077	0.255562	0.515429	-0.000548161	0.1848	0.0663705	0.000764422
-102.880769	5.823077	0.141666	0.520855	-0.0005088	0.217956	0.0740578	0.000798368
-125.476923	5.884615	0.100757	0.523384	-0.000485264	0.231596	0.0771719	0.000815238
-55.661538	65.669231	0.207339	0.515528	-0.000545809	0.199785	0.0689917	0.000764009
-55.661538	37.046154	0.204444	0.515748	-0.000551646	0.200664	0.0692077	0.000765097
-55.661538	-10.969231	0.223885	0.515506	-0.000549929	0.19453	0.0681046	0.000764283
-55.661538	-19.853846	0.22432	0.515224	-0.00052861	0.194243	0.0679796	0.000762979
-102.880769	65.669231	0.0935633	0.520953	-0.000506453	0.232903	0.0766724	0.000797956
-102.880769	37.046154	0.0907927	0.521173	-0.000512268	0.233745	0.0768815	0.00079904
-102.880769	-10.969231	0.109703	0.520933	-0.000510584	0.227773	0.0758076	0.000798228
-102.880769	-19.853846	0.11024	0.520648	-0.000489134	0.227454	0.0756764	0.000796917
-125.476923	65.669231	0.0527037	0.523482	-0.00048292	0.246527	0.0797839	0.000814827
-125.476923	37.046154	0.0499839	0.5237	-0.000488725	0.247353	0.0799901	0.000815908
-125.476923	-10.969231	0.0686771	0.523462	-0.000487055	0.241449	0.0789281	0.000815098
-125.476923	-19.853846	0.0692557	0.523176	-0.000465551	0.241117	0.0787944	0.000813783

Table A4: Transducer 023 Data Reduction Table

Transducer Temperature [deg C]	SSE Temperature [deg C]	Coefficient a_0 [psi]	Coefficient a_1 [psi/mV]	Coefficient a_2 [psi/mV^2]	Coefficient a_0 Variance [psi^2/σ_c^2]	Coefficient a_1 Variance [psi^2/σ_c^2/mV^2]	Coefficient a_2 Variance [psi^2/σ_c^2/mV^4]
-83.246154	65.669231	0.431721	0.517612	-0.000372652	0.146975	0.0583138	0.000789257
-83.046154	37.046154	0.426987	0.517893	-0.0003573	0.147748	0.0585557	0.000790562
-84.012821	9.982051	0.446653	0.517771	-0.000364253	0.144723	0.0575863	0.000789957
-84.330769	-10.969231	0.425463	0.517553	-0.000346407	0.148011	0.0586036	0.00078953
-84.215385	-19.853846	0.423299	0.517586	-0.000351806	0.148377	0.0586947	0.000789212
-56.630769	5.673077	0.364932	0.513769	-0.000342595	0.159307	0.0607122	0.000765859
-104.273077	5.823077	0.533301	0.520664	-0.000373743	0.132499	0.0540352	0.00080818
-126.953846	5.884615	0.62715	0.523817	-0.000367432	0.122873	0.0503102	0.00082922
-56.630769	65.669231	0.348844	0.513598	-0.000351644	0.161733	0.061496	0.000765104
-56.630769	37.046154	0.342135	0.513911	-0.000334535	0.162814	0.061836	0.000766559
-56.630769	-10.969231	0.3481	0.513596	-0.000328419	0.161919	0.0615203	0.000765519
-56.630769	-19.853846	0.344951	0.513611	-0.000331945	0.162433	0.0616605	0.000765221
-104.273077	65.669231	0.517254	0.520493	-0.000382769	0.134919	0.0548171	0.000807427
-104.273077	37.046154	0.510613	0.520805	-0.000365721	0.135989	0.0551536	0.000808877
-104.273077	-10.969231	0.516317	0.520489	-0.000359439	0.135134	0.0548506	0.000807837
-104.273077	-19.853846	0.513203	0.520504	-0.000363031	0.135643	0.0549891	0.000807538
-126.953846	65.669231	0.611119	0.523646	-0.000376449	0.12529	0.0510913	0.000828468
-126.953846	37.046154	0.604506	0.523958	-0.000359426	0.126356	0.0514264	0.000829916
-126.953846	-10.969231	0.610104	0.523642	-0.000353075	0.125518	0.0511286	0.000828876
-126.953846	-19.853846	0.607003	0.523657	-0.000356694	0.126025	0.0512664	0.000828577

Table A5: Transducer 024 Data Reduction Table

Transducer Temperature [deg C]	SSE Temperature [deg C]	Coefficient a_0 [psi]	Coefficient a_1 [psi/mV]	Coefficient a_2 [psi/mV^2]	Coefficient a_0 Variance [psi^2/σ_c^2]	Coefficient a_1 Variance [psi^2/σ_c^2/mV^2]	Coefficient a_2 Variance [psi^2/σ_c^2/mV^4]
-83.430769	65.669231	0.471553	0.515984	-0.000288337	0.140685	0.0560805	0.00078295
-82.976923	37.046154	0.470648	0.515793	-0.000266242	0.140812	0.0560971	0.000782641
-83.905128	9.982051	0.485604	0.51558	-0.000248678	0.138744	0.0553977	0.000782859
-84.023077	-10.969231	0.470919	0.515272	-0.000228205	0.140765	0.0560331	0.000781536
-83.884615	-19.853846	0.47091	0.515273	-0.000242822	0.14077	0.0560162	0.000780851
-56.369231	5.673077	0.472285	0.51147	-0.000231113	0.140626	0.0551654	0.000758824
-104.261539	5.823077	0.508839	0.518634	-0.000271332	0.135526	0.0549148	0.000800784
-127.246154	5.884615	0.527014	0.521782	-0.000270422	0.133163	0.0546614	0.00081986
-56.369231	65.669231	0.457147	0.511904	-0.00027384	0.142718	0.0559011	0.000758922
-56.369231	37.046154	0.454948	0.511716	-0.000251473	0.143024	0.0559762	0.00075857
-56.369231	-10.969231	0.46062	0.511225	-0.00021485	0.142232	0.0556702	0.000757772
-56.369231	-19.853846	0.459713	0.511207	-0.000226102	0.14236	0.0556947	0.000757105
-104.261539	65.669231	0.493739	0.519067	-0.000313952	0.137612	0.0556487	0.000800881
-104.261539	37.046154	0.491585	0.518879	-0.000291595	0.137912	0.0557217	0.000800531
-104.261539	-10.969231	0.497069	0.518387	-0.000254923	0.137146	0.0554241	0.000799723
-104.261539	-19.853846	0.496193	0.51837	-0.000266292	0.13727	0.0554471	0.000799055
-127.246154	65.669231	0.51193	0.522215	-0.000312999	0.135247	0.0553945	0.000819957
-127.246154	37.046154	0.509794	0.522027	-0.000290646	0.135544	0.0554667	0.000819608
-127.246154	-10.969231	0.515201	0.521534	-0.000253953	0.134789	0.0551726	0.000818795
-127.246154	-19.853846	0.514338	0.521517	-0.00026537	0.134911	0.055195	0.000818127

Table A6: Transducer 025 Data Reduction Table

Transducer Temperature [deg C]	SSE Temperature [deg C]	Coefficient a_0 [psi]	Coefficient a_1 [psi/mV]	Coefficient a_2 [psi/mV^2]	Coefficient a_0 Variance [psi^2/σ_c^2]	Coefficient a_1 Variance [psi^2/σ_c^2/mV^2]	Coefficient a_2 Variance [psi^2/σ_c^2/mV^4]
-81.830769	65.669231	0.207901	0.515277	-0.000224418	0.197279	0.0695058	0.000780613
-82.053846	37.046154	0.208777	0.515673	-0.000231006	0.197019	0.0695431	0.000782573
-83.243590	9.982051	0.235432	0.515732	-0.000239055	0.189908	0.0681314	0.000782818
-83.900000	-10.969231	0.210654	0.515708	-0.000242144	0.196496	0.069454	0.000782522
-83.961538	-19.853846	0.212294	0.515549	-0.000242442	0.196031	0.0693272	0.000781614
-56.165385	5.673077	0.282795	0.511545	-0.000248891	0.177609	0.0645346	0.000757295
-103.253846	5.823077	0.230407	0.519205	-0.00026773	0.191091	0.0692765	0.000802839
-125.569231	5.884615	0.216442	0.522331	-0.000236396	0.194829	0.07092	0.000823775
-56.165385	65.669231	0.253133	0.511054	-0.000233121	0.185551	0.0660153	0.000754919
-56.165385	37.046154	0.251895	0.511476	-0.00023956	0.185853	0.066171	0.000757011
-56.165385	-10.969231	0.263113	0.511525	-0.000251344	0.182843	0.0655852	0.00075706
-56.165385	-19.853846	0.262998	0.511388	-0.000251789	0.182848	0.0655577	0.000756265
-103.253846	65.669231	0.200819	0.518716	-0.000251999	0.199013	0.0707536	0.000800469
-103.253846	37.046154	0.199655	0.519137	-0.000258444	0.199295	0.0709052	0.000802556
-103.253846	-10.969231	0.210547	0.519186	-0.000270205	0.196372	0.0703366	0.000802601
-103.253846	-19.853846	0.210493	0.519048	-0.000270645	0.196361	0.0703057	0.000801803
-125.569231	65.669231	0.186885	0.521841	-0.000220681	0.202743	0.0723955	0.000821407
-125.569231	37.046154	0.185751	0.522262	-0.000227128	0.203017	0.0725454	0.000823492
-125.569231	-10.969231	0.19651	0.522311	-0.00023888	0.200129	0.071984	0.000823536
-125.569231	-19.853846	0.196481	0.522173	-0.000239317	0.200111	0.0719516	0.000822736

Table A7: Transducer 026 Data Reduction Table

Transducer Temperature [deg C]	SSE Temperature [deg C]	Coefficient a_0 [psi]	Coefficient a_1 [psi/mV]	Coefficient a_2 [psi/mV^2]	Coefficient a_0 Variance [psi^2/σ_c^2]	Coefficient a_1 Variance [psi^2/σ_c^2/mV^2]	Coefficient a_2 Variance [psi^2/σ_c^2/mV^4]
-80.738462	62.115385	0.234251	0.514585	-0.000115512	0.189873	0.0680741	0.000781775
-82.423077	31.553846	0.229062	0.514936	-9.86688e-05	0.191315	0.0685121	0.000785204
-84.648718	5.361539	0.244167	0.515653	-0.000172036	0.187323	0.0677282	0.00078546
-85.284615	-13.030769	0.22921	0.515083	-0.00011888	0.191269	0.0684952	0.000784924
-85.815385	-21.438462	0.229628	0.514961	-0.00010379	0.191169	0.0684953	0.000785308
-55.634615	6.050000	0.303789	0.511016	-0.00014066	0.172374	0.063464	0.000759242
-103.911539	5.496154	0.217973	0.518335	-0.000145245	0.194438	0.0699287	0.000803547
-128.376923	4.307692	0.165185	0.521936	-0.000126424	0.21014	0.0738847	0.000826664
-80.738462	62.115385	0.234251	0.514585	-0.000115512	0.189873	0.0680741	0.000781775
-80.738462	31.553846	0.251876	0.515421	-0.000201119	0.185215	0.0671594	0.000782074
-80.738462	-13.030769	0.173138	0.512256	0.00010167	0.205992	0.0712079	0.000779585
-80.738462	-21.438462	0.188924	0.512429	9.72559e-05	0.201864	0.070466	0.000781299
-85.815385	62.115385	0.223722	0.514361	-6.82312e-05	0.192688	0.0686983	0.000783219
-85.815385	31.553846	0.229062	0.514936	-9.86688e-05	0.191315	0.0685121	0.000785204
-85.815385	-13.030769	0.192803	0.513554	3.01867e-05	0.200879	0.0703713	0.000783904
-85.815385	-21.438462	0.200314	0.513568	3.62752e-05	0.19892	0.0700291	0.000784902
-55.634615	62.115385	0.293993	0.509961	-8.48223e-05	0.174893	0.0638057	0.000755601
-55.634615	31.553846	0.28908	0.510318	-6.92214e-05	0.176261	0.0642273	0.000758992
-55.634615	-13.030769	0.288271	0.510425	-8.55143e-05	0.176467	0.0642597	0.000758686
-55.634615	-21.438462	0.288877	0.510307	-7.06614e-05	0.176319	0.0642509	0.000759086
-103.911539	62.115385	0.20808	0.51727	-8.88552e-05	0.196981	0.0702738	0.000799871
-103.911539	31.553846	0.202945	0.517622	-7.22545e-05	0.198409	0.0707085	0.000803292
-103.911539	-13.030769	0.202906	0.517761	-9.16995e-05	0.198412	0.0707013	0.000803008
-103.911539	-21.438462	0.203361	0.51764	-7.66562e-05	0.198303	0.0706997	0.000803394
-128.376923	62.115385	0.155085	0.520848	-6.88512e-05	0.212737	0.0742371	0.00082291
-128.376923	31.553846	0.149472	0.52119	-5.01051e-05	0.214292	0.0747002	0.000826397
-128.376923	-13.030769	0.151085	0.521399	-7.63139e-05	0.213859	0.0746078	0.000826158
-128.376923	-21.438462	0.151218	0.521272	-6.08623e-05	0.213835	0.0746218	0.000826517

Table A8: Transducer 027 Data Reduction Table

Transducer Temperature [deg C]	SSE Temperature [deg C]	Coefficient a_0 [psi]	Coefficient a_1 [psi/mV]	Coefficient a_2 [psi/mV^2]	Coefficient a_0 Variance [psi^2/σ_c^2]	Coefficient a_1 Variance [psi^2/σ_c^2/mV^2]	Coefficient a_2 Variance [psi^2/σ_c^2/mV^4]
-82.784615	62.115385	-0.132842	0.51698	-0.000203774	0.335124	0.0899824	0.000790633
-83.953846	31.553846	-0.133255	0.516177	-9.84903e-05	0.335531	0.0900399	0.00079165
-86.071795	5.361539	-0.127222	0.517164	-0.000175696	0.332108	0.0897095	0.000792722
-86.300000	-13.030769	-0.134484	0.516775	-0.000148329	0.336108	0.0901826	0.000792546
-86.753846	-21.438462	-0.13527	0.517125	-0.000181281	0.336485	0.0902651	0.000792915
-56.850000	6.050000	-0.0411581	0.512574	-0.000179086	0.289647	0.0829441	0.000765335
-105.569231	5.496154	-0.17526	0.519847	-0.000146235	0.358633	0.093863	0.000811474
-130.015385	4.307692	-0.245017	0.523474	-0.000123133	0.400663	0.0999095	0.000835837
-56.850000	62.115385	-0.0467105	0.512392	-0.000206823	0.292627	0.0832137	0.000763271
-56.850000	31.553846	-0.0470329	0.511613	-0.000103909	0.29298	0.0832658	0.000764291
-56.850000	-13.030769	-0.0486925	0.51217	-0.000150694	0.293796	0.0834349	0.000765152
-56.850000	-21.438462	-0.0494129	0.512534	-0.000184814	0.294136	0.083514	0.000765533
-105.569231	62.115385	-0.180867	0.519663	-0.000174246	0.361642	0.0941353	0.00080939
-105.569231	31.553846	-0.181262	0.518865	-6.94264e-05	0.362039	0.0941918	0.000810408
-105.569231	-13.030769	-0.182576	0.519455	-0.000118668	0.362662	0.0943396	0.000811297
-105.569231	-21.438462	-0.183349	0.519808	-0.000151848	0.363032	0.0944214	0.000811668
-130.015385	62.115385	-0.250742	0.523286	-0.000151732	0.403735	0.100187	0.000833709
-130.015385	31.553846	-0.251293	0.522446	-4.28205e-05	0.404224	0.100253	0.000834722
-130.015385	-13.030769	-0.251863	0.523106	-9.73333e-05	0.404433	0.100355	0.000835671
-130.015385	-21.438462	-0.252748	0.523436	-0.000128498	0.404867	0.100443	0.000836022

Table A9: Transducer 029 Data Reduction Table

Transducer Temperature [deg C]	SSE Temperature [deg C]	Coefficient a_0 [psi]	Coefficient a_1 [psi/mV]	Coefficient a_2 [psi/mV^2]	Coefficient a_0 Variance [psi^2/σ_c^2]	Coefficient a_1 Variance [psi^2/σ_c^2/mV^2]	Coefficient a_2 Variance [psi^2/σ_c^2/mV^4]
-82.300000	65.669231	0.417556	0.515048	-0.00025281	0.149345	0.0585483	0.000778709
-82.484615	37.046154	0.416928	0.515417	-0.000263106	0.149456	0.0586514	0.000780482
-83.569231	9.982051	0.446872	0.515248	-0.000267522	0.144857	0.0571659	0.000779474
-84.200000	-10.969231	0.418472	0.515005	-0.000255466	0.149183	0.0584734	0.000778078
-84.261538	-19.853846	0.418068	0.514883	-0.000248292	0.149251	0.0584736	0.000777658
-56.442308	5.673077	0.413831	0.511341	-0.000241016	0.150235	0.0579129	0.000756892
-103.696154	5.823077	0.501892	0.517906	-0.000282286	0.13657	0.0550735	0.000795513
-126.092308	5.884615	0.536681	0.520776	-0.000276451	0.131995	0.054032	0.000814114
-56.442308	65.669231	0.382246	0.511125	-0.000225166	0.15507	0.0594023	0.000756067
-56.442308	37.046154	0.379119	0.511537	-0.000235897	0.155567	0.0596349	0.00075806
-56.442308	-10.969231	0.391272	0.511148	-0.00023144	0.153671	0.0589515	0.000755782
-56.442308	-19.853846	0.389187	0.511028	-0.000224563	0.153994	0.0590317	0.000755337
-103.696154	65.669231	0.470386	0.517691	-0.000266475	0.141392	0.0565591	0.00079469
-103.696154	37.046154	0.467346	0.518101	-0.000277191	0.141875	0.0567872	0.000796675
-103.696154	-10.969231	0.479129	0.517711	-0.000272623	0.140036	0.0561214	0.000794393
-103.696154	-19.853846	0.477103	0.517591	-0.000265736	0.140351	0.0561989	0.000793949
-126.092308	65.669231	0.505207	0.520562	-0.000260656	0.136813	0.0555162	0.000813293
-126.092308	37.046154	0.502203	0.520971	-0.000271367	0.13729	0.0557424	0.000815275
-126.092308	-10.969231	0.513835	0.520581	-0.000266753	0.135475	0.0550838	0.000812991
-126.092308	-19.853846	0.511832	0.520461	-0.000259862	0.135785	0.0551601	0.000812547

Table A10: Transducer 030 Data Reduction Table

Transducer Temperature [deg C]	SSE Temperature [deg C]	Coefficient a_0 [psi]	Coefficient a_1 [psi/mV]	Coefficient a_2 [psi/mV^2]	Coefficient a_0 Variance [psi^2/σ_c^2]	Coefficient a_1 Variance [psi^2/σ_c^2/mV^2]	Coefficient a_2 Variance [psi^2/σ_c^2/mV^4]
-82.223077	62.115385	0.227641	0.519137	-0.000476796	0.191665	0.0689259	0.00079033
-83.753846	31.553846	0.225166	0.519655	-0.000465804	0.192341	0.0692083	0.000793953
-85.948718	5.361539	0.247918	0.519916	-0.000498186	0.186454	0.0680424	0.000794571
-86.284615	-13.030769	0.227609	0.519749	-0.000498694	0.191697	0.0690882	0.000793448
-86.746154	-21.438462	0.227983	0.51979	-0.000494254	0.191603	0.0691018	0.000794121
-56.992307	6.050000	0.270934	0.51569	-0.000511567	0.180467	0.0657271	0.000768559
-105.253847	5.496154	0.258503	0.523118	-0.000536056	0.183554	0.0682659	0.000812993
-129.623077	4.307692	0.251818	0.525927	-0.000441487	0.185197	0.0695407	0.000835818
-56.992307	62.115385	0.250903	0.514921	-0.000490436	0.185615	0.0665998	0.00076437
-56.992307	31.553846	0.24878	0.515436	-0.000480036	0.186199	0.0668623	0.000767958
-56.992307	-13.030769	0.249865	0.515517	-0.000512094	0.185905	0.066812	0.000767394
-56.992307	-21.438462	0.250487	0.515561	-0.000507534	0.185747	0.0668137	0.000768097
-105.253847	62.115385	0.238274	0.52234	-0.000514717	0.188753	0.0691472	0.000808762
-105.253847	31.553846	0.235868	0.522858	-0.000503841	0.189411	0.0694257	0.000812379
-105.253847	-13.030769	0.238045	0.52295	-0.000536568	0.188835	0.0693193	0.000811861
-105.253847	-21.438462	0.238468	0.522991	-0.000532104	0.188729	0.0693306	0.00081254
-129.623077	62.115385	0.231165	0.525134	-0.0004197	0.190505	0.0704406	0.000831498
-129.623077	31.553846	0.228151	0.525656	-0.000407802	0.191321	0.0707535	0.000835176
-129.623077	-13.030769	0.232673	0.52577	-0.000441965	0.190139	0.0705265	0.000834759
-129.623077	-21.438462	0.232667	0.525806	-0.000437709	0.190143	0.0705584	0.000835385

Table A11: Transducer 031 Data Reduction Table

Transducer Temperature [deg C]	SSE Temperature [deg C]	Coefficient a_0 [psi]	Coefficient a_1 [psi/mV]	Coefficient a_2 [psi/mV^2]	Coefficient a_0 Variance [psi^2/σ_c^2]	Coefficient a_1 Variance [psi^2/σ_c^2/mV^2]	Coefficient a_2 Variance [psi^2/σ_c^2/mV^4]
-81.592308	62.115385	0.726873	0.513782	-6.89746e-05	0.116373	0.044317	0.000780263
-83.323077	31.553846	0.730343	0.514638	-0.000122926	0.116203	0.0442713	0.000782944
-85.612821	5.361539	0.744678	0.514508	-9.40716e-05	0.11562	0.0436851	0.000783761
-86.038462	-13.030769	0.732697	0.514532	-9.8784e-05	0.116097	0.0441949	0.000783866
-86.538462	-21.438462	0.73315	0.514402	-9.73839e-05	0.116076	0.0441705	0.000783468
-56.657692	6.050000	0.630285	0.510356	-7.70179e-05	0.122657	0.0478691	0.000759371
-104.815384	5.496154	0.835552	0.517234	-9.57254e-05	0.113018	0.0403901	0.000800438
-129.084615	4.307692	0.95118	0.520953	-0.000127936	0.112986	0.036427	0.000823021
-56.657692	62.115385	0.612696	0.509638	-5.22254e-05	0.123401	0.0484933	0.000755916
-56.657692	31.553846	0.616326	0.510482	-0.000105113	0.123225	0.0484398	0.000758576
-56.657692	-13.030769	0.617854	0.510381	-8.19067e-05	0.123152	0.0483979	0.00075948
-56.657692	-21.438462	0.61846	0.510247	-8.04153e-05	0.123125	0.0483669	0.000759071
-104.815384	62.115385	0.81779	0.516509	-7.0688e-05	0.113769	0.0410205	0.000796948
-104.815384	31.553846	0.82129	0.517363	-0.000124431	0.113598	0.0409732	0.000799625
-104.815384	-13.030769	0.823483	0.517258	-0.000100472	0.113498	0.0409036	0.000800543
-104.815384	-21.438462	0.823966	0.517128	-9.90543e-05	0.113476	0.0408779	0.000800143
-129.084615	62.115385	0.933044	0.520214	-0.000102373	0.113752	0.0370706	0.000819458
-129.084615	31.553846	0.936267	0.521088	-0.000157951	0.113592	0.0370367	0.000822171
-129.084615	-13.030769	0.939884	0.520976	-0.000132379	0.113435	0.0369076	0.00082312
-129.084615	-21.438462	0.940105	0.520852	-0.000131118	0.113424	0.0368933	0.00082274

Table A12: Transducer 032 Data Reduction Table

Transducer Temperature [deg C]	SSE Temperature [deg C]	Coefficient a_0 [psi]	Coefficient a_1 [psi/mV]	Coefficient a_2 [psi/mV^2]	Coefficient a_0 Variance [psi^2/σ_c^2]	Coefficient a_1 Variance [psi^2/σ_c^2/mV^2]	Coefficient a_2 Variance [psi^2/σ_c^2/mV^4]
-83.030769	65.669231	0.0350482	0.517963	-0.000411366	0.256492	0.0794932	0.000784902
-82.984615	37.046154	0.0349066	0.518198	-0.000415031	0.256479	0.0795084	0.00078553
-84.015384	9.982051	0.0561545	0.518261	-0.000444352	0.248371	0.0782544	0.000784695
-84.507692	-10.969231	0.0370359	0.51811	-0.000421946	0.255649	0.0793648	0.000784891
-84.407692	-19.853846	0.0386804	0.517924	-0.000421536	0.254965	0.0791894	0.00078353
-56.884615	5.673077	0.105545	0.514236	-0.000467475	0.230084	0.0742528	0.000759953
-104.215385	5.823077	0.0454301	0.521806	-0.000461583	0.252396	0.0799131	0.000805555
-126.661538	5.884615	0.0240557	0.52496	-0.000406474	0.260869	0.0822746	0.000828137
-56.884615	65.669231	0.0828059	0.513914	-0.000431937	0.238833	0.0755875	0.000760176
-56.884615	37.046154	0.0809145	0.514162	-0.000433486	0.239483	0.0757064	0.00076092
-56.884615	-10.969231	0.0903589	0.514116	-0.000449678	0.235865	0.0751348	0.000760108
-56.884615	-19.853846	0.0905949	0.513947	-0.000447954	0.235726	0.0750528	0.000758956
-104.215385	65.669231	0.0227475	0.521485	-0.000426133	0.261123	0.0812444	0.000805777
-104.215385	37.046154	0.020917	0.521732	-0.000427756	0.261749	0.0813598	0.000806518
-104.215385	-10.969231	0.0301067	0.521685	-0.000443625	0.258229	0.0808031	0.000805712
-104.215385	-19.853846	0.0303918	0.521515	-0.000441947	0.258071	0.0807178	0.000804552
-126.661538	65.669231	0.00139633	0.524639	-0.000371061	0.269587	0.0836046	0.00082836
-126.661538	37.046154	-0.000409183	0.524886	-0.000372714	0.270204	0.0837184	0.000829099
-126.661538	-10.969231	0.00867607	0.524838	-0.00038845	0.266723	0.0831678	0.000828295
-126.661538	-19.853846	0.00898127	0.524668	-0.000386791	0.266557	0.0830812	0.000827132

Table A13: Transducer 034 Data Reduction Table

Transducer Temperature [deg C]	SSE Temperature [deg C]	Coefficient a_0 [psi]	Coefficient a_1 [psi/mV]	Coefficient a_2 [psi/mV^2]	Coefficient a_0 Variance [psi^2/σ_c^2]	Coefficient a_1 Variance [psi^2/σ_c^2/mV^2]	Coefficient a_2 Variance [psi^2/σ_c^2/mV^4]
-82.969231	62.115385	0.266626	0.489744	0.00411212	0.184439	0.0741271	0.000938655
-83.984615	31.553846	0.266162	0.490853	0.00402612	0.184554	0.0742599	0.000940881
-85.994872	5.361539	0.297868	0.49203	0.00389744	0.176502	0.0720405	0.000935899
-86.176923	-13.030769	0.267905	0.490561	0.0040443	0.184068	0.0741122	0.000939995
-86.584615	-21.438462	0.267733	0.490824	0.00403319	0.184129	0.0741988	0.00094152
-56.753846	6.050000	0.296085	0.482992	0.00474296	0.177139	0.0724488	0.000938876
-105.669231	5.496154	0.336577	0.500088	0.00313395	0.166341	0.0691279	0.000928076
-130.261538	4.307692	0.362463	0.508502	0.00224616	0.160074	0.0666176	0.000910954
-56.753846	62.115385	0.265223	0.480734	0.00495503	0.18498	0.0745101	0.000941599
-56.753846	31.553846	0.265213	0.481846	0.00486826	0.18498	0.0746099	0.000943728
-56.753846	-13.030769	0.265	0.481468	0.00489531	0.184989	0.074598	0.000943125
-56.753846	-21.438462	0.265176	0.481756	0.00488219	0.184962	0.0746626	0.000944642
-105.669231	62.115385	0.30541	0.497807	0.00334811	0.174259	0.0712096	0.000930826
-105.669231	31.553846	0.305035	0.498916	0.00326196	0.174352	0.0713359	0.000933033
-105.669231	-13.030769	0.306395	0.498607	0.00328188	0.173963	0.0712147	0.000932202
-105.669231	-21.438462	0.306291	0.498876	0.00327037	0.174007	0.071297	0.000933726
-130.261538	62.115385	0.330642	0.506173	0.00246482	0.168159	0.068743	0.000913762
-130.261538	31.553846	0.329482	0.507277	0.00238002	0.16845	0.0689263	0.000916137
-130.261538	-13.030769	0.334217	0.507117	0.0023846	0.167207	0.0685706	0.000914815
-130.261538	-21.438462	0.333514	0.507344	0.00237657	0.167402	0.068691	0.000916354

Table A14: Transducer 036 Data Reduction Table

Transducer Temperature [deg C]	SSE Temperature [deg C]	Coefficient a_0 [psi]	Coefficient a_1 [psi/mV]	Coefficient a_2 [psi/mV^2]	Coefficient a_0 Variance [psi^2/σ_c^2]	Coefficient a_1 Variance [psi^2/σ_c^2/mV^2]	Coefficient a_2 Variance [psi^2/σ_c^2/mV^4]
-83.253846	62.115385	0.349353	0.501208	0.00415164	0.162132	0.0674153	0.000946735
-84.269231	31.553846	0.347025	0.500988	0.00431867	0.162622	0.0678102	0.000955057
-86.082051	5.361539	0.378274	0.501727	0.0042866	0.156582	0.0659053	0.000953888
-86.169231	-13.030769	0.347367	0.501041	0.00435717	0.16252	0.0677992	0.000956494
-86.469231	-21.438462	0.347242	0.500842	0.00436942	0.16259	0.0679172	0.000957979
-56.723077	6.050000	0.387325	0.499498	0.00408563	0.154544	0.0641723	0.000922299
-105.965384	5.496154	0.400728	0.504188	0.00431441	0.152011	0.0653968	0.000974489
-130.861538	4.307692	0.406632	0.506727	0.00438466	0.150737	0.0659058	0.00099843
-56.723077	62.115385	0.358755	0.498985	0.00395231	0.160027	0.0656639	0.000915233
-56.723077	31.553846	0.356898	0.498778	0.00411686	0.160425	0.0660271	0.000923438
-56.723077	-13.030769	0.355262	0.498786	0.00415884	0.160705	0.066137	0.000925003
-56.723077	-21.438462	0.355497	0.49859	0.00417058	0.160707	0.0662358	0.000926496
-105.965384	62.115385	0.371876	0.503669	0.00417977	0.157548	0.0669032	0.000967353
-105.965384	31.553846	0.36964	0.503453	0.00434632	0.158019	0.0672919	0.000975652
-105.965384	-13.030769	0.369596	0.503497	0.0043855	0.157992	0.0673045	0.000977114
-105.965384	-21.438462	0.369541	0.503298	0.00439765	0.158049	0.0674188	0.000978601
-130.861538	62.115385	0.377174	0.506197	0.0042472	0.15639	0.0674439	0.000991145
-130.861538	31.553846	0.374126	0.505958	0.00441803	0.15702	0.0678874	0.000999647
-130.861538	-13.030769	0.377497	0.506079	0.00445119	0.156335	0.0676912	0.00100089
-130.861538	-21.438462	0.376821	0.505876	0.00446423	0.156509	0.0678386	0.00100236

Appendix B

Error Analysis Sensitivities

Plots in this Appendix show the impact of the MEADS system errors in a single variable sense in order to show sensitivities to each individual error parameter. The net effects of all errors together are shown in Figures 4.31–4.33. Here, the MEADS hardware uncertainties are shown in Figures B1–B11 and the errors due to CFD uncertainties are shown in Figures B12–B14.

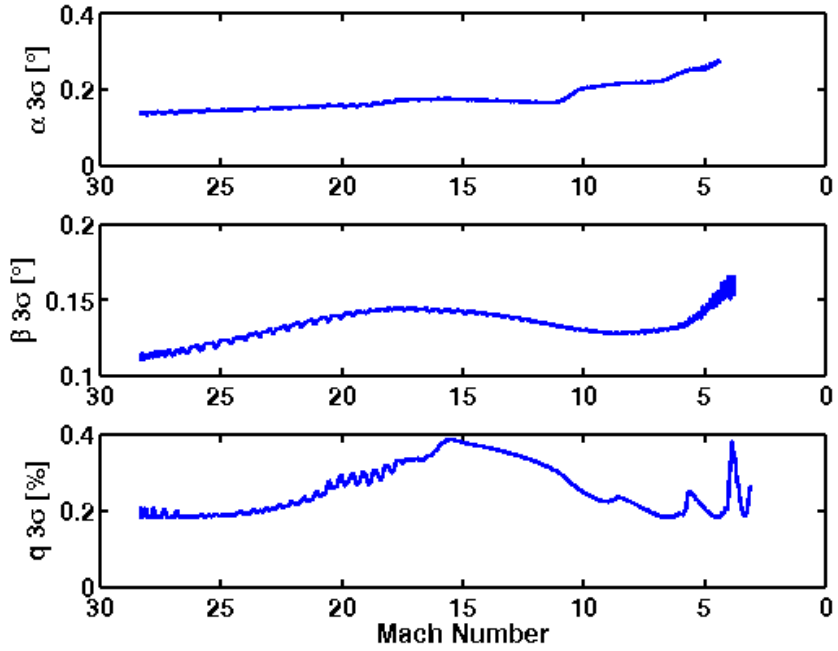

Figure B1: Estimation Errors due to Calibration Uncertainty

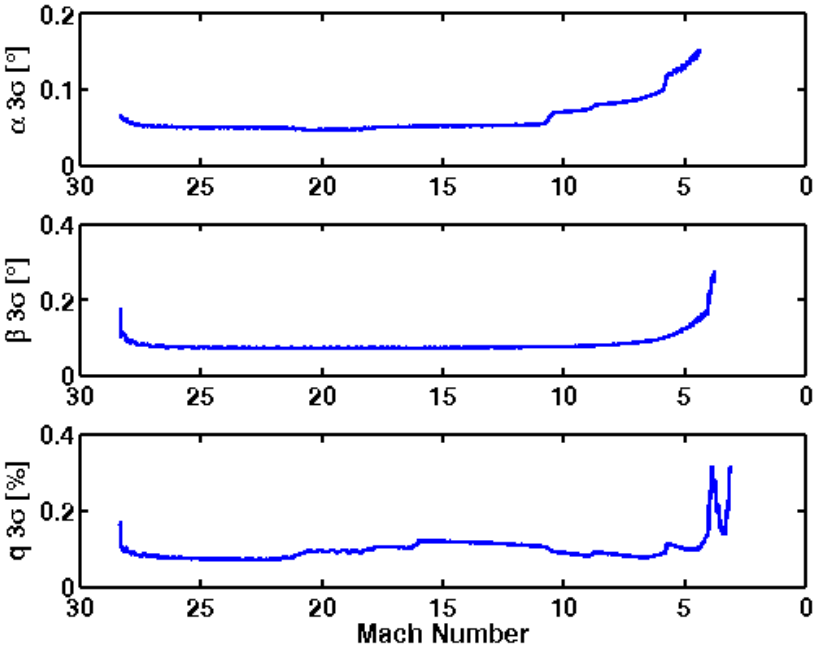

Figure B2: Estimation Errors due to Transducer Temperature Uncertainty

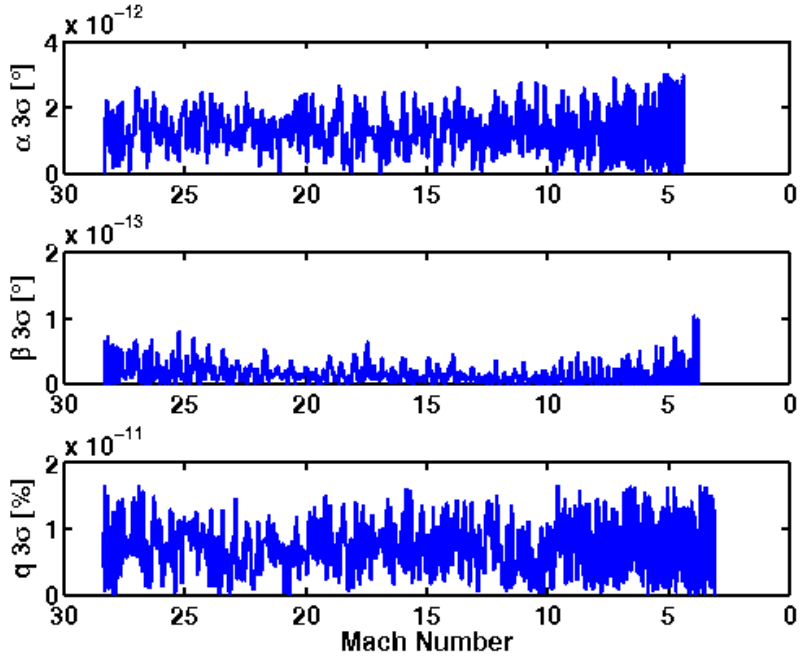

Figure B3: Estimation Errors due to Quantization

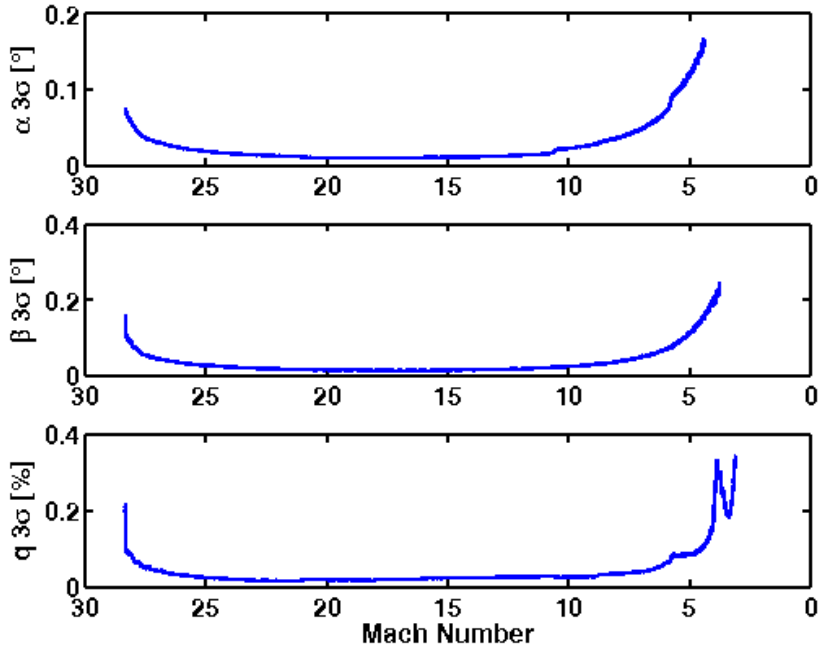

Figure B4: Estimation Errors due to SSE Noise

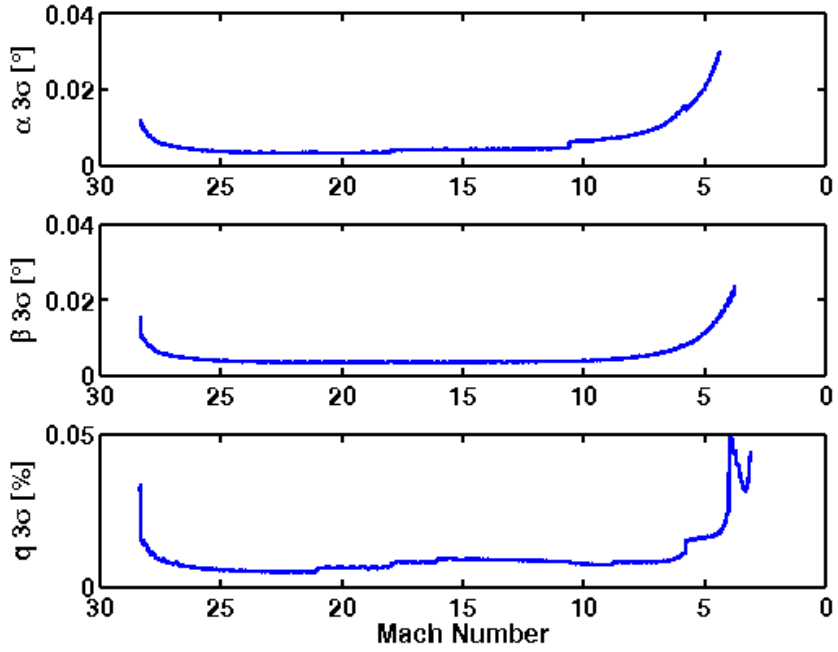

Figure B5: Estimation Errors due to SSE Temperature Uncertainty)

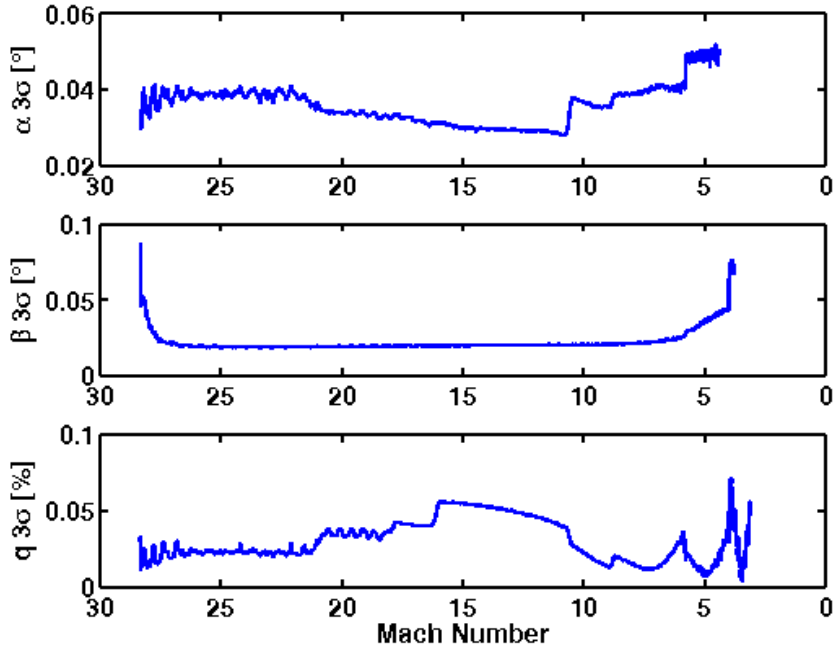

Figure B6: Estimation Errors due to Port Location Uncertainty

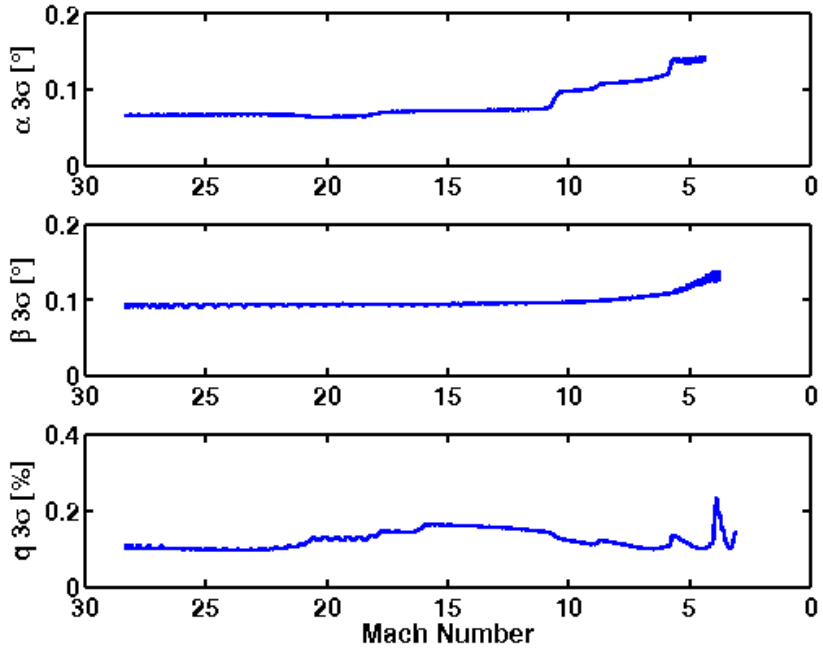

Figure B7: Estimation Errors due to Pressure Leak Uncertainty

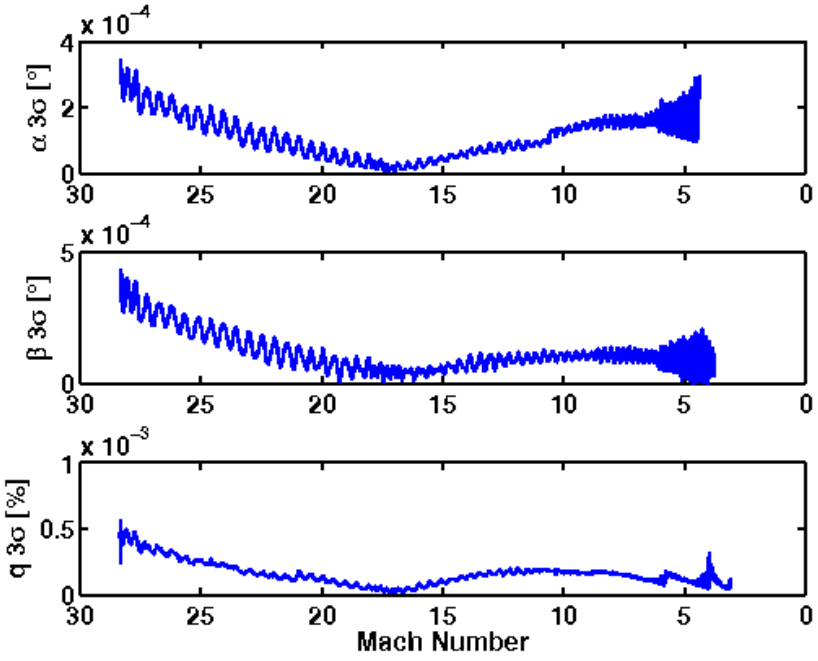

Figure B8: Estimation Errors due to Time Tag Uncertainty

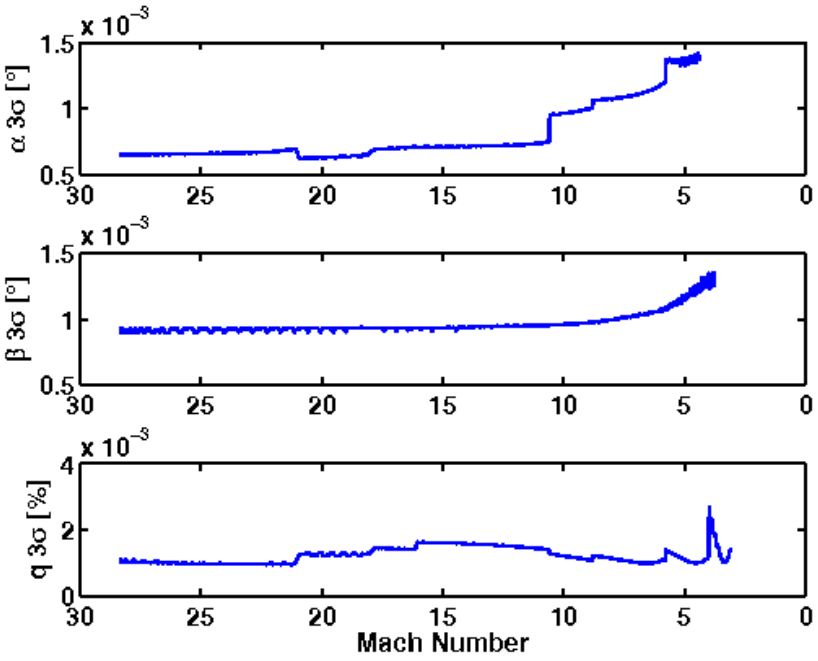

Figure B9: Estimation Errors due to Pneumatic Lag Uncertainty

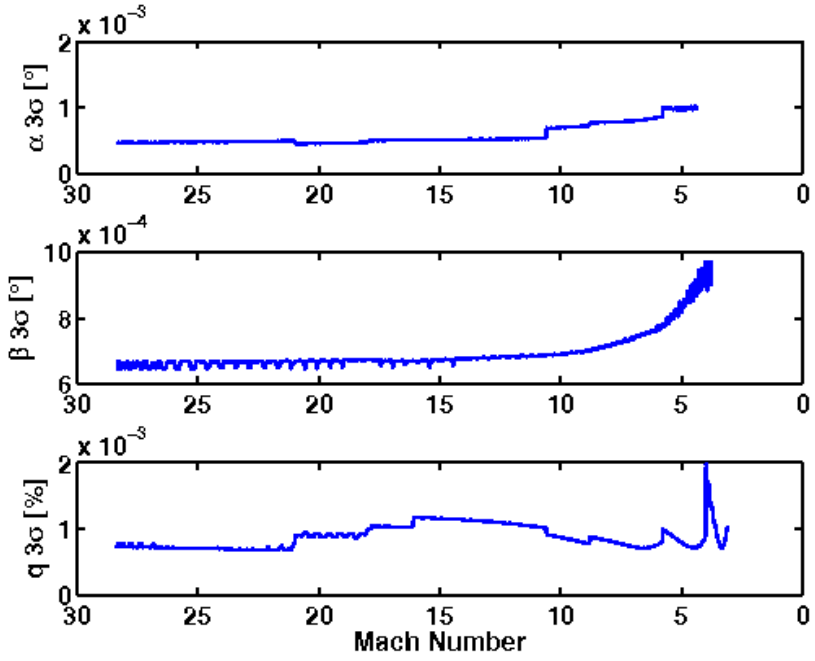

Figure B10: Estimation Errors due to Thermal Transpiration Uncertainty)

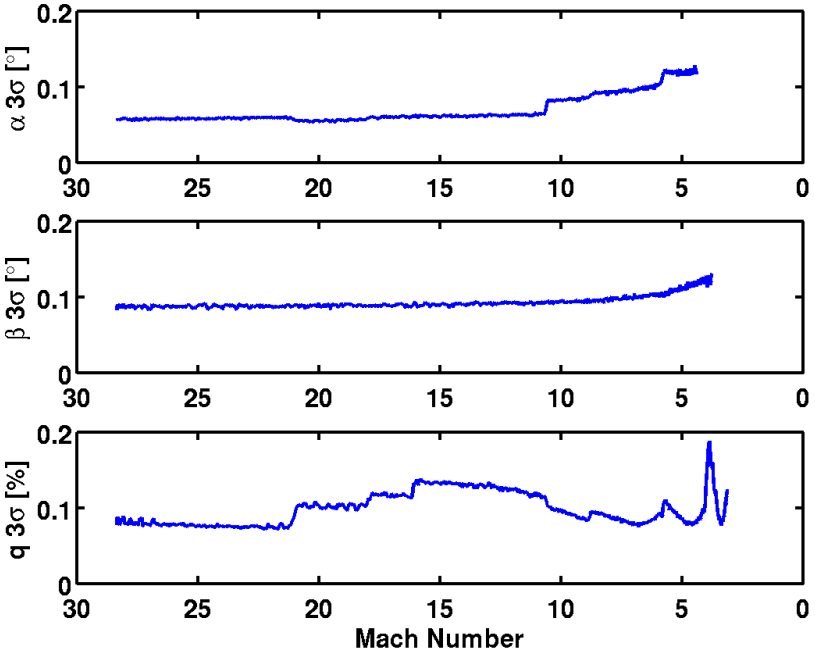

Figure B11: Estimation Errors due to Vibration

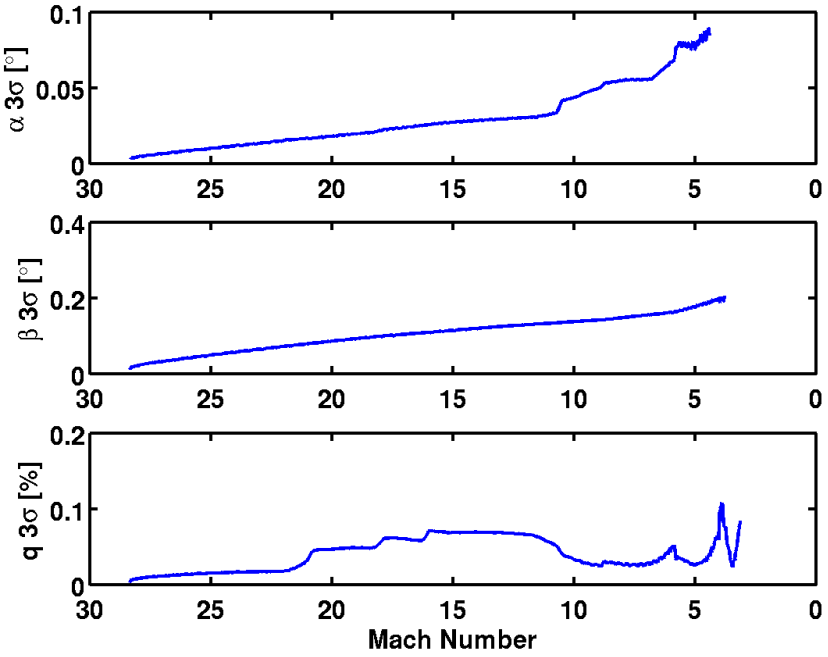

Figure B12: Estimation Errors due to Ablation

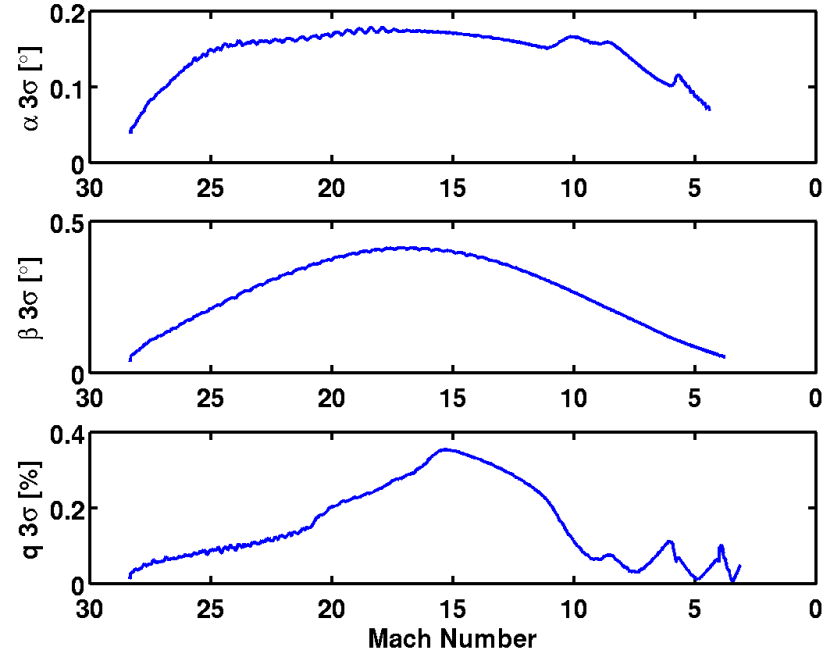

Figure B13: Estimation Errors due to Deformation

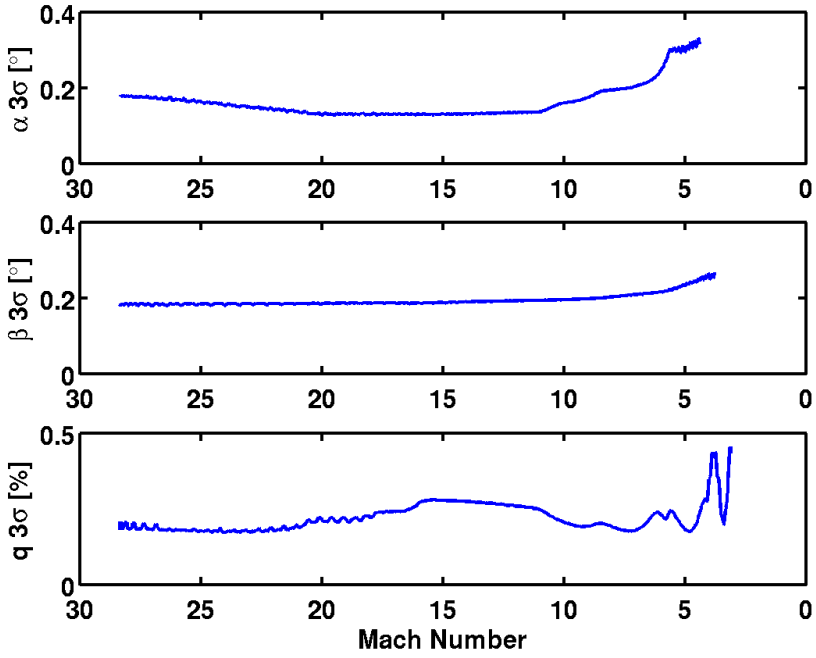

Figure B14: Estimation Errors due to OML Change

References

1. Gazarik, M. J., Wright, M. J., Little, A., Cheatwood, F. M., Herath, J. A., Munk, M. M., Novak, F. J., and Martinez, E. R., "Overview of the MEDLI Project," IEEE 2008 Aerospace Conference, March 2008.

2. Munk, M. M., Little, A., Kuhl, C., Bose, D., and Santos, J., "The Mars Science Laboratory (MSL) Entry, Descent, and Landing Instrumentation (MEDLI) Hardware," AAS Paper 13-310, February 2013.

3. Schoenenberger, M., Dyakonov, A., Buning, P., Scallion, W., and Van Norman, J., "Aerodynamic Challenges for the Mars Science Laboratory Entry, Descent and Landing," AIAA Paper 2009-3914, June 2009.

4. Pruett, C. D., Wolf, H., Heck, M. L., and Siemers, P. M., "Innovative Air Data System for the Space Shuttle Orbiter," *Journal of Spacecraft and Rockets*, Vol. 20, No. 1, 1983, pp. 61–69.

5. Siemers, P. M., Bradley, P. F., Wolf, H., Flanagan, P. F., Weilmuenster, K. J., and Kern, F. A., "Shuttle Flight Pressure Instrumentation: Experience and Lessons for the Future," NASA Langley Conference on Shuttle Performance: Lessons Learned, Hampton, VA, March 1983.

6. Wolf, H., Flanagan, P. F., and Henry, H. W., "Shuttle Entry Air Data System Program Manual," Analytical Mechanics Associates, Inc., AMA Report 85–4, March 1985.

7. Siemers, P. M., Henry, M. W., and Eades, J. B., "Shuttle Entry Air Data System (SEADS) - Advanced Air Data System Results: Air Data Across the Entry Speed Range," *Orbiter Experiments (OEX) Aerothermodynamics Symposium*, NASA CP-3248, Part I, April 1995, pp. 49–78.

8. Abilleira, F. and Shidner, J., "Entry, Descent, and Landing Communications for the 2011 Mars Science Laboratory," Paper IN1-4, 23rd International Symposium on Space Flight Dynamics, Pasadena, CA, October 2012.

9. Steltzner, A. D., Burkhart, P. D., Chen, A., Comeaux, K. A., Guernsey, C. S., Kipp, D. M., Lorenzoni, L. V., Mendeck, G. F., Powell, R. W., Rivellini, T. P., San Martin, A. M., Sell, S. W., Prakash, R., and Way, D. D., "Mars Science Laboratory Entry, Descent, and Landing System Overview," 7th International Planetary Probe Workshop, Barcelona, Spain, June 2010.

10. Wagner, W. E., "Re-Entry Filtering, Prediction, and Smoothing," *Journal of Spacecraft and Rockets*, Vol. 3, No. 9, 1966, pp. 1321–1327.

11. Wagner, W. E. and Serold, A. C., "Formulation on Statistical Trajectory Estimation Programs," NASA CR-1482, January 1970.

12. Karlgaard, C. D., Tartabini, P. V., Blanchard, R. C., Kirsch, M., and Toniolo, M. D., "Hyper–X Post–Flight Trajectory Reconstruction," *Journal of Spacecraft and Rockets*, Vol. 43, No. 1, 2006, pp. 105–115.

13. Karlgaard, C. D., Tartabini, P. V., Martin, J. G., Blanchard, R. C., Kirsch, M., Toniolo, M. D., and Thornblom, M. N., "Statistical Estimation Methods for Trajectory Reconstruction: Application to Hyper-X," NASA TM-2009-215792, August 2009.

14. Karlgaard, C. D., Beck, R. E., Derry, S. D., Brandon, J. M., Starr, B. R., Tartabini, P. V., and Olds, A. D., "Ares I-X Trajectory Reconstruction: Methodology and Results," *Journal of Spacecraft and Rockets*, Vol. 50, No. 3, 2013, pp. 641–661.

15. Karlgaard, C. D., Beck, R. E., O'Keefe, S. A., Siemers, P. M., White, B. A., Engelund, W. C., and Munk, M. M., "Mars Entry Atmospheric Data System Modeling and Algorithm Development," AIAA Paper 2009-3916, June 2009.

16. Hollis, B. R., Liechty, D. S., Wright, M. J., Holden, M. S., Wadhams, T. P., MacLean, M., and Dyakonov, A., "Transition Onset and Turbulent Heating Measurements for the Mars Science Laboratory Entry Vehicle," 43rd AIAA Aerospace Sciences Meeting and Exhibit, Reno, NV, January 2005.

17. Crassidis, J. C. and Junkins, J. L., *Optimal Estimation of Dynamic Systems*, Chapman & Hall/CRC, Boca Raton, FL, 2004.

18. Cheatwood, F. and Gnoffo, P., "Users Manual for the Langley Aerothermal Upwind Relaxation Algorithm (LAURA)," NASA TM-4674, April 1996.

19. Dyakonov, A., Schoenenberger, M., and Van Norman, J., "Hypersonic and Supersonic Static Aerodynamics of Mars Science Laboratory Entry Vehicle," AIAA Paper 2012-2999, June 2012.

20. Edquist, K. T., Dyakonov, A. A., Wright, M. J., and Tang, C. Y., "Aerothermodynamic Environments Definition for the Mars Science Laboratory Entry Capsule," AIAA Paper 2007-1206, January 2007.

21. Schoenenberger, M., Dyakonov, A., and Van Norman, J., "Mars Science Laboratory Aerodynamics V&V Review," December 2010.

22. Edquist, K. T., Dyakonov, A., Wright, M. J., and Tang, C. Y., "Mars Science Laboratory Entry Capsule Aerothermodynamics Environments: Revision B," November 2010.

23. Jackson, C. M., Corlett, W. A., and Monta, W. J., "Description and Calibration of the Langley Unitary Plan Wind Tunnel," NASA TP-1905, 1981.

24. Gibson, L. S. and Sealey, B. S., "Test and Evaluation of Pressure Transducers for a Reentry Vehicle Pressure Measurement System," 39th International Instrumentation Symposium, May 1993, pp. 1013–1030.

25. Parker, P. A., Hutchinson, M. A., Mitchell, M., and Munk, M. M., "Strategic Pressure Measurement System Characterization of the Mars Entry Atmospheric Data System," 6th International Planetary Probe Workshop, Atlanta, GA, June 2008.

26. McCollum, R. A., Commo, S. A., and Parker, P. A., "Calibration Modeling Methodology to Optimize Performance for Low Range Applications," 7th International Symposium on Strain-Gauge Balances, May 2010.

27. Kowalski, S. M., Parker, P. A., and Vining, G. G., "Tutorial: Industrial Split-Plot Experiments," *Quality Engineering*, Vol. 19, No. 1, 2007, pp. 1-15.

28. Bruce, W. E., "MEDLI/MEADS Pressure Path Leak Rate Heating Analysis," MEDLI-0234, October 27, 2010.

29. Shams, Q. A., "Leak Impact on Transducer Diaphragm Pressure," MEDLI-0237, February 10, 2011.

30. Bergh, H. and Tijdeman, H., "Theoretical and Experimental Results for the Dynamic Response of Pressure Measuring Systems," NLR–TR F.238, January 1965.

31. Whitmore, S. A., "Frequency Response Model for Branched Pneumatic Sensing Systems," *Journal of Aircraft*, Vol. 43, No. 6, 2006, pp. 1845–1853.

32. Whitmore, S. A. and Fox, B., "Improved Accuracy, Second–Order Response Model for Pressure Sensing Systems," *Journal of Aircraft*, Vol. 46, No. 2, 2009, pp. 491–500.

33. Chapin, W. G., "Dynamic-Pressure Measurements Using an Electrically Scanned Pressure Module," NASA TM–84650, July 1983.

34. Whitmore, S. A. and Moes, T. R., "Measurement Uncertainty and Feasibility Study of a Flush Airdata System for Hypersonic Flight Experiment," NASA TM 4627, 1994.

35. Knudsen, M., "Thermischer Molekulardruck in Röhren," *Annalen der Physik*, Vol. 83, 1927, pp. 797–821.

36. Kennard, E. H., *Kinetic Theory of Gases*, McGraw–Hill, New York, 1938, pp. 327–333.

37. Rasmussen, M., *Hypersonic Flow*, John Wiley & Sons, Inc., New York, 1994.

38. Potter, J. L., "Correction of Measured Pressures to Account for Thermomolecular Flow in Orifices and Tubes: User Guide and Program," Analytical Mechanics Associates, Inc., NASA Contract No. NAS1–18935, October 1991.

39. Potter, J. L., Kinslow, M., and Boylan, D. E., "An Influence of the Orifice on Measured Pressures in Rarefied Flow," 4th Symposium on Rarefied Gas Dynamics, de Leeuw, J. H. (Ed.), Vol. 2, 1966, pp. 175–194.

40. Kinslow, M. and Arney, G. D., Jr., "Thermomolecular Pressure Effects in Tubes and at Orifices," AGARDograph 119, August 1967.

41. Kinslow, M. and Potter, J. L., "Reevaluation of Parameters Relative to the Orifice Effect," 7th Symposium on Rarefied Gas Dynamics, Dini, D., (Ed.), Vol. 1, 1971, pp. 399–408.

42. Scholz, D., "MSL-ST-11-0056-HS2-Dimensional.pdf," Lockheed Martin Space Systems Company, July 2011.

43. Tang, C. Y., Wright, M. J., Edquist, K. T., Sepka, S. A., and Cassell, A. M., "Numerical Simulations of Protruding Gapfillers on the Mars Science Laboratory Heatshield," 41st AIAA Thermophysics Conference, San Antonio, TX, June 2009.

44. Mazaheri, A., "LAURA-B Tutorial," 2009.

45. Franklin, R. E. and Wallace, J. M., "Absolute Measurements of Static-Hole Error Using Flush Transducers," *Journal of Fluid Mechanics*, Vol. 42, 1970.

46. McKeon, B. J. and Smits, A. J., "Static Pressure Correction in High Reynolds Number Fully Developed Turbulent Pipe Flow," *Measurement Science and Technology*, Vol. 13, 2002.

47. Mensor/WIKA Data Sheet CPC 6000, April 2011

48. MEDLI SAR charts, February 16, 2011, Page 67.

49. Cheatwood, F. M., Bose, D., Karlgaard, C., Kuhl, C. A., Santos, J. A., and Wright, M. J., "Mars Science Laboratory (MSL) Entry, Descent, and Landing Instrumentation (MEDLI): Complete Flight Data Set," NASA TM, 2014, to be published.

50. Karlgaard, C. D., Kutty, P., Schoenenberger, M., Munk, M. M., Little, A., Kuhl, C. A., and Shidner, J., "Mars Science Laboratory Entry Atmospheric Data System Trajectory and Atmosphere Reconstruction," *Journal of Spacecraft and Rockets*, Vol. 51, No. 4, 2014, pp. 1029–1047. doi: 10.2514/1.A32770.

51. Chen, A., Cianciolo, A., Vasavada, A., Karlgaard, C., Barnes, J., Cantor, B., Hinson, D., Kass, D., Lewis, S., Mischna, M., Rafkin, S., and Tyler, D., "Reconstruction of Atmospheric Properties from the Mars Science Laboratory Entry, Descent, and Landing," *Journal of Spacecraft and Rockets*, Vol. 51, No. 4, 2014, pp. 1062–1075. doi: 10.2514/1.A32708.

52. Schoenenberger, M., Van Norman, J., Karlgaard, C. D., Kutty, P., and Way, D., "Assessment of the Reconstructed Aerodynamics of the Mars Science Laboratory Entry Vehicle," *Journal of Spacecraft and Rockets*, Vol. 51, No. 4, 2014, pp. 1076–1093. doi: 10.2514/1.A32794.

REPORT DOCUMENTATION PAGE

Form Approved
OMB No. 0704–0188

1. REPORT DATE *(DD-MM-YYYY)*	2. REPORT TYPE	3. DATES COVERED *(From - To)*
01-10-2014	Technical Memorandum	

4. TITLE AND SUBTITLE
Mars Entry Atmospheric Data System Modeling, Calibration, and Error Analysis

5a. CONTRACT NUMBER

5b. GRANT NUMBER

5c. PROGRAM ELEMENT NUMBER

6. AUTHOR(S)
Karlgaard, C. D., Van Norman, J., Siemers, P. M., Schoenenberger, M., and Munk, M. M.

5d. PROJECT NUMBER

5e. TASK NUMBER

5f. WORK UNIT NUMBER
757285.01.07.20

7. PERFORMING ORGANIZATION NAME(S) AND ADDRESS(ES)
NASA Langley Research Center
Hampton, Virginia 23681-2199

8. PERFORMING ORGANIZATION REPORT NUMBER
L–20464

9. SPONSORING/MONITORING AGENCY NAME(S) AND ADDRESS(ES)
National Aeronautics and Space Administration
Washington, DC 20546-0001

10. SPONSOR/MONITOR'S ACRONYM(S)
NASA

11. SPONSOR/MONITOR'S REPORT NUMBER(S)
NASA/TM–2014–218535

12. DISTRIBUTION/AVAILABILITY STATEMENT
Unclassified-Unlimited
Subject Category 19 Spacecraft Instrumentation and Astronics
Availability: NASA CASI (443) 757-5802

13. SUPPLEMENTARY NOTES
An electronic version can be found at http://ntrs.nasa.gov.

14. ABSTRACT

The Mars Science Laboratory (MSL) Entry, Descent, and Landing Instrumentation (MEDLI)/Mars Entry Atmospheric Data System (MEADS) project installed seven pressure ports through the MSL Phenolic Impregnated Carbon Ablator (PICA) heatshield to measure heatshield surface pressures during entry. These measured surface pressures are used to generate estimates of atmospheric quantities based on modeled surface pressure distributions. In particular, the quantities to be estimated from the MEADS pressure measurements include the dynamic pressure, angle of attack, and angle of sideslip. This report describes the calibration of the pressure transducers utilized to reconstruct the atmospheric data and associated uncertainty models, pressure modeling and uncertainty analysis, and system performance results. The results indicate that the MEADS pressure measurement system hardware meets the project requirements.

15. SUBJECT TERMS

16. SECURITY CLASSIFICATION OF:			17. LIMITATION OF ABSTRACT	18. NUMBER OF PAGES	19a. NAME OF RESPONSIBLE PERSON
a. REPORT	b. ABSTRACT	c. THIS PAGE			STI Help Desk (email: help@sti.nasa.gov)
U	U	U	UU	97	19b. TELEPHONE NUMBER *(Include area code)* (443) 757-5802